秋田県立大学大学院博士学位論文

Investigation on Growth and Performance of Anodic Aluminum Oxide Film Fabricated in Etidronic Acid under High Current Density

（高電流密度下でエチドロン酸により作製された陽極酸化 Al_2O_3 膜の成長と性能の評価）

黄　紅鍵

Hongjian Huang

2021 年 3 月

Abstract

Anodizing aluminum and its alloys in acidic electrolyte solutions results in the formation of anodic aluminum oxide (AAO), or porous anodic alumina (PAA), with numerous nanometer-scale pores. It is generally believed that the structure and performance of AAO films strongly depend on the type of electrolytes (chromic, sulfuric, oxalic and phosphoric acids, etc.), in which the films are fabricated. Most recently, many novel properties obtained via anodizing in newly discovered etidronic acid (HEDP) are attracted more and more attention, such as submicrometer-scale array, structural coloration, high hardness and corrosion resistance. In this work, the anodizing behavior in etidronic acid was systematically investigated by changing current density, electrolyte temperature and anodizing duration. Moreover, in order to broaden the application fields of HEDP anodized film, the hard anodizing was developed on the commercial aluminum alloy.

In chapter 1, the research backgrounds, research significance, summary of the research and the construction of this thesis are described. The objectives of the research are to study the anodizing behavior in etidronic acid and the properties of the resultant film.

In chapter 2, the properties of experimental materials, as well as the experimental methods and the characterizations are presented.

In chapter 3, anodic aluminum oxide films and micro-arc oxide (MAO) coatings are generally prepared from different electrochemical regimes. In this work, we prepared a new hard coating with a MAO/AAO double layer structure in HEDP solution by one-step way for the first time. The influence of current densities on the coating structures, elements distribution, phases composition and hardness was systematically investigated. Results showed that the AAO film would not be burnt down until the current density increased up to 8 A/dm^2. A steady sparking was observed when the current density was higher than 4 A/dm^2, and the visible sparks would automatically quench after a while. The obtained oxide coatings had both the outer volcanic resolidified pool structure and

inner honeycomb structure, i.e., a MAO/AAO composite coating. EDS results suggested that the concentration of anion contaminants of MAO layer was lower than that of AAO layer. The estimated growth rate of oxide coating increased from 1 to 36 μm/h with the increase of current densities from 1 to 7 A/dm^2. The hardness of inner AAO layer was about 6−8 GPa, which was in contrast with the highest hardness (26.57 GPa) of the outer MAO layer.

In chapter 4, the growth mechanisms of MAO/AAO coating found in chapter 3 were systematically investigated. In this work, anodizing of aluminum was carried out in HEDP solution at high current density with different duration to track the formation behavior of the coating. SEM images indicated that the burning of initial film is actually caused by local oxide cracking due to the increase of compressive stress. The soft spark would appear when voltage reached 300 V, then change to the micro arcs at 400 V, and finally manufacture the outer MAO layer. Hereafter, the automatic extinguishing of micro arcs gives rise to the formation of inner AAO layer. Moreover, it is evidenced that plasma discharge has few contributions to coating thickening. The barrier layer provides the raw materials for the growth of outer MAO layer. Based on these results, the growth mechanism of MAO/AAO coating processed in HEDP is proposed and discussed.

In chapter 5, we selected a commercial aluminum alloy (6063T5) as the object and developed a high-performance anodized film via HEDP hard anodizing. In this work, the mild HEDP anodizing was first investigated at a temperature range of 15–45ºC, just under the burning current densities. The voltage curves and microstructures of the anodized film prepared in HEDP (Eti-film) indicate that 35ºC is the most appropriate temperature for the fast fabrication of Eti-film, in contrast to the MAO coating and the seriously surface-corroded Eti-film prepared at 15 and 45ºC, respectively. Then, the HEDP hard anodizing without burning was successfully conducted via a gradient-increase-current approach, resulting in a high growth rate (~ 2.1 μm/min), low porosity (< 10%), thick barrier layer (~ 510 nm) and branched nanoholes structure of the hard anodized Eti-film. The Eti-films were systematically investigated by scanning electron microscopy, energy-dispersive X-

ray spectroscopy, X-ray photoelectron spectroscopy, X-ray diffraction, transmission electron microscopy, and a nanoindentation tester. In addition, the wear and corrosion resistance of the Eti-film and the hard sulfuric acid anodized film (Sul-film) were compared. The results indicate that the hardness of the Eti-film can reach ~ 11 GPa (~ 1000 $HV_{0.01}$). The better wear resistance of the Eti-film as compared to the currently widely used Sul-film is attributed to the low porosity and less hydrated alumina content of the Eti-film. Moreover, the corrosion resistance of the Eti-film has been found to be 10 times higher than that of the Sul-film. In general, our results suggest a possibility of replacing the pollution-carrying anodizing methods currently used in the industry with the etidronic acid anodizing.

In chapter 6, general conclusions of this dissertation are made.

Content

Abstract i
Chapter 1 Introduction 1
1.1 Background 1
1.2 Structure of anodic aluminum oxide film 1
1.3 Growth mechanism of porous-type anodic alumina film 5
1.3.1 Interface reactions 5
1.3.2 Volume expansion 6
1.3.3 Kinetics for generation of honeycomb structure 7
1.3.4 Film evolution and electrochemical response during anodizing 9
1.4 Anodizing technology 10
1.4.1 Anodizing equipment 10
1.4.2 Mild, hard, and self-ordering anodizing processes 11
1.4.3 Electrolyte and anodizing voltage 15
1.4.4 Post-sealing treatment 17
1.5 Micro-arc oxidation 18
1.6 Research topic and contribution of this dissertation 21
References 24
Chapter 2 Materials, Experiment and Characterizations 33
2.1 Materials 33
2.2 Sample preparation 33
2.2.1 Pre-treatment of sample 33
2.2.2 Anodizing 34
2.3 Characterization 36
2.3.1 Thickness of film 36
2.3.2 Scanning electron microscopy (SEM) 36
2.3.3 Energy dispersive spectrometry (EDS) and X-ray photoelectron spectroscopy (XPS) 36
2.3.4 X-ray diffractometer (XRD) and selected-area electron diffraction (SAED) 37
2.3.5 Microhardness test 37
2.3.6 Wear resistance 37
2.3.7 Corrosion resistance 37
Chapter 3 A hard coating with MAO/AAO double layers prepared on aluminum in HEDP 39
3.1 Introduction 39
3.2 Experimental procedure 41
3.2.1 Sample preparation 41
3.2.2 Characterization 41
3.3 Results and discussion 42
3.3.1 Evolution of electrical characteristics and colour 42
3.3.2 Surface structural characteristics 45

3.3.3 Cross-sectional structural characteristics 49
3.3.4 The distribution of elements....52
3.3.5 Coatings phase analysis 54
3.3.6 Hardness and elastic modulus of coatings 55
3.4 Conclusions....57
References....58
Chapter 4 Morphological evolution and burning behavior of MAO/AAO coating 63
4.1 Introduction....63
4.2 Experimental procedure 65
4.2.1 Sample preparation 65
4.2.2 Characterization 65
4.3 Results and discussion 66
4.3.1 Maximum current density and burning behavior of anodic film....66
4.3.2 Morphologies and element distributions of the burnt area....67
4.3.3 Stable plasma discharge behavior 69
4.3.4 Surface roughness and compositions of coatings....70
4.3.5 Morphology evolution of coating formed at 6 A/dm^2 71
4.3.6 Coating growth kinetics 77
4.3.7 Proposed growth mechanism 80
4.4 Conclusions....82
References....82
Chapter 5 Ultra-fast fabrication of porous alumina film with excellent wear and corrosion resistance via HEDP hard anodizing....89
5.1 Introduction....89
5.2 Experimental procedure 91
5.2.1 Sample preparation 91
5.2.2 Characterization 92
5.3 Results and discussion 93
5.3.1 Effect of electrolyte temperature on the Eti-film 93
5.3.2 Electrochemical behaviors of anodizing just under the burning current....95
5.3.3 HEDP hard anodizing 99
5.3.4 Elemental composition and crystalline state of the hard anodized Eti-film....102
5.3.5 Mechanical performance of the hard anodized Eti-film....104
5.3.6 Corrosion resistances of the hard anodized Eti-film 108
5.4 Conclusions....113
References....114
Chapter 6 Conclusions....120
6.1 General conclusions and remarks 120
6.2 Future work....121
List of Research Achievement....122
Acknowledgements 124

Chapter 1 Introduction

1.1 Background

In ambient atmospheres, aluminum would become rapidly coated with a compact 2−3 nm thick oxide layer. This native oxide layer prevents the metal surface from further oxidation, nevertheless, it struggles to meet the protection requirements. In 1857, Buff first found that aluminum can be electrochemically oxidized in an aqueous solution to form an oxide layer that is thicker than the native one [1]. This phenomenon has been called “anodizing” because the aluminum part to be processed constitutes the anode in an electrolytic cell. With the development of industry, the structural components made from aluminium and its alloys get attentions since about 1930 due to the high strength/weight ratio, meanwhile, anodizing began to be widely used to improve the surface performance of aluminium [2, 3].

Anodizing (also called anodization) is a simple, low cost, and straightforward approach that can be used to synthesize an oxide layer over the large surface area of the metallic substrate, such as aluminum, titanium and magnesium, etc.. The anodic alumina film has good mechanical properties, high corrosion resistance, abrasion resistance, and strong adsorption. Attractive appearance can be obtained on aluminum by treating the anodized aluminum with various coloring methods. In addition, the anodic alumina film also has good functional characteristics, e.g. dielectric properties, selective absorption of light and nano-honeycomb hole array structure. With the development of anodizing, more and more new characteristics of anodic alumina film have been discovered. Notably, aluminum anodizing and anodizing theory, a subject that has been studied for decades, have again attracted the attention in various fields since the nanohole arrays were prepared by Masuda, et al. through the two-step anodizing in 1995 [4].

1.2 Structure of anodic aluminum oxide film

It is commonly known that the nature of an electrolyte used for anodizing is a key factor,

which determines the morphology of oxide grown on the aluminum surface. Generally, two different morphologies of AAO films can be formed, i.e. the nonporous barrier-type AAO films and the porous-type AAO films (Fig. 1.1), which are mainly determined by the types and characteristics of the electrolyte. The barrier-type films are formed in neutral electrolytes (pH 5−7), such as borate, oxalate, citrate, phosphate, adipate, tungstate solution, etc. [1]. A porous-type film is formed in the electrolyte that promotes the dissolution of the oxide film, such as selenic [5], sulfuric [6], oxalic [7], phosphoric [4], chromic [8], malonic [9], tartaric [10], citric [11], malic acid [10], etc..

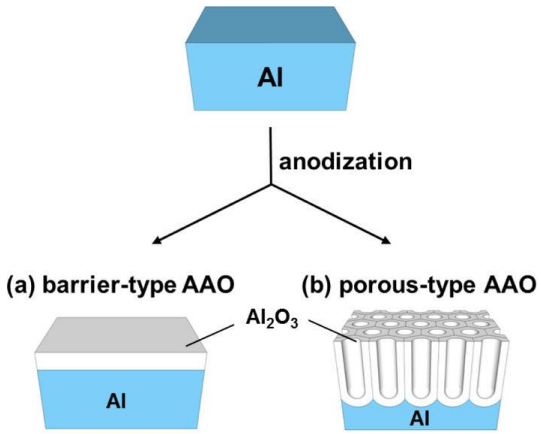

Fig. 1.1 Two different types of anodic aluminum oxide (AAO). (a) barrier-type and (b) porous-type. [1]

The porous-type AAO film is also called porous anodic alumina film (PAA), which has received more attention than barrier-type AAO film due to the unique honeycomb structure, as shown in Fig. 1.2. Porous anodic films consist of a thin barrier layer located at the aluminum/film interface and an outer porous region containing cylindrical pores extending from the surface of the film to the barrier layer. The film has a close packed array of columnar hexagonal cells each with a central, cylindrical, uniformly sized pore. The pores in the film are parallel to each other and are known for having a honeycomb-like structure with a short distance ordering and a long distance disordering of the pore arrangement. The barrier layer at the bottom of each cell is approximately hemispherical, so that the aluminum/oxide interface appears scalloped. However, the morphology of the

anodic alumina films commonly obtained is far from the honeycomb-like idealized structure; usually the cells are irregular polygons, and the configuration of the cells and pores is not hexagonal, causing distortions of the cross section of the pores and broadening of the pore diameter distribution.

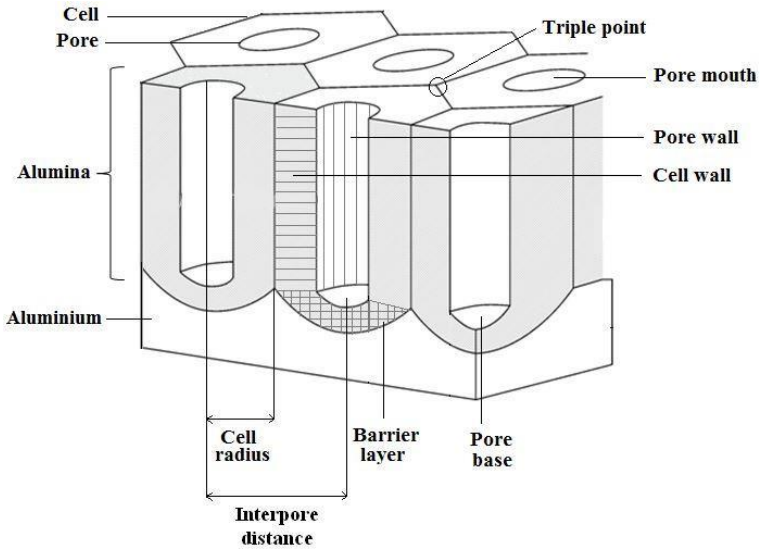

Fig. 1.2 Schematic representation of the morphology of PAA.[12]

As early as the last century, the multi-layer structure of the PAA has attracted the attention of researchers. In 1978, G.E. Thompson et al. found that PAA consists of bilayer structures, i.e., an outer layer containing a large amount of electrolyte anions and an inner layer of pure and dense alumina [13, 14], which is widely accepted and consistent with electron microscope observation and component analysis. Fig. 1.3 shows the bilayer structure and elemental distribution of PAA recently investigated by Kikuchi et al. [15].

It is believed that the thickness ratio of outer layers of PAAs depends on electrolytes and the distribution of the potential drop across barrier layers of PAAs formed in different electrolytes behaves differently (Fig. 1.4). The difference in the composition of the inner and outer layers of PAA also leads to the difference in the etching rate (the etching speed of the inner layer is slower than that of outer layer) [16].

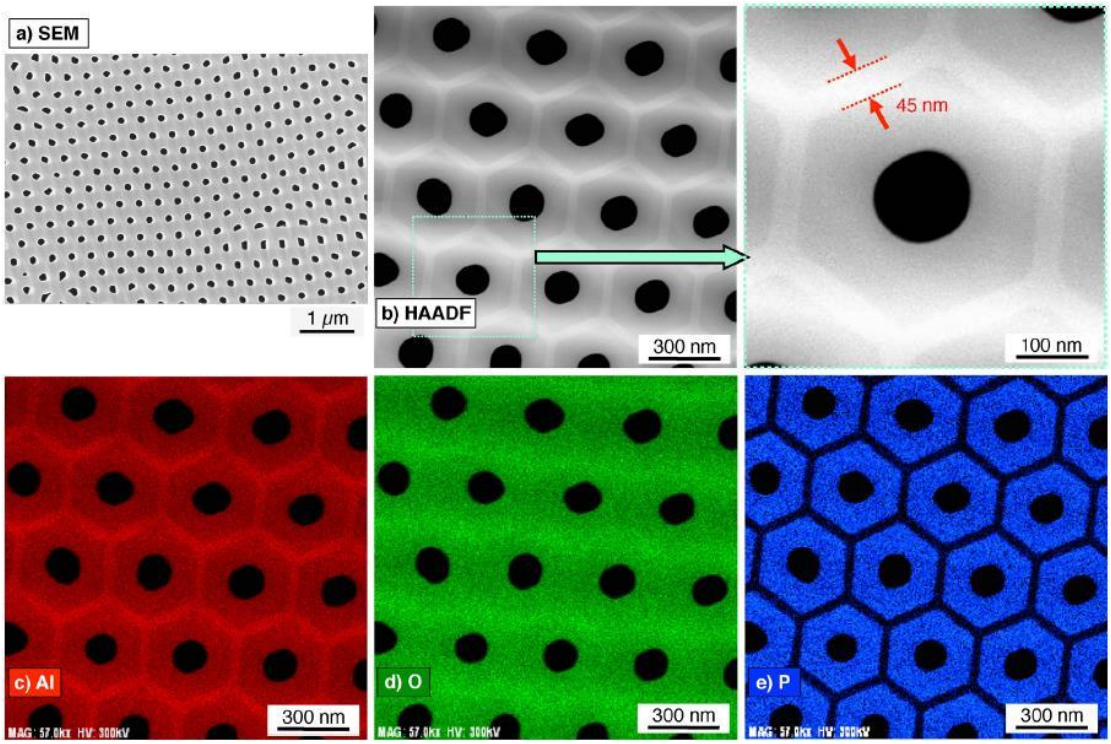

Fig. 1.3 The bilayer structure and elemental distribution of PAA fabricated in phosphonic acid observed under transmission electron microscope (TEM).[15]

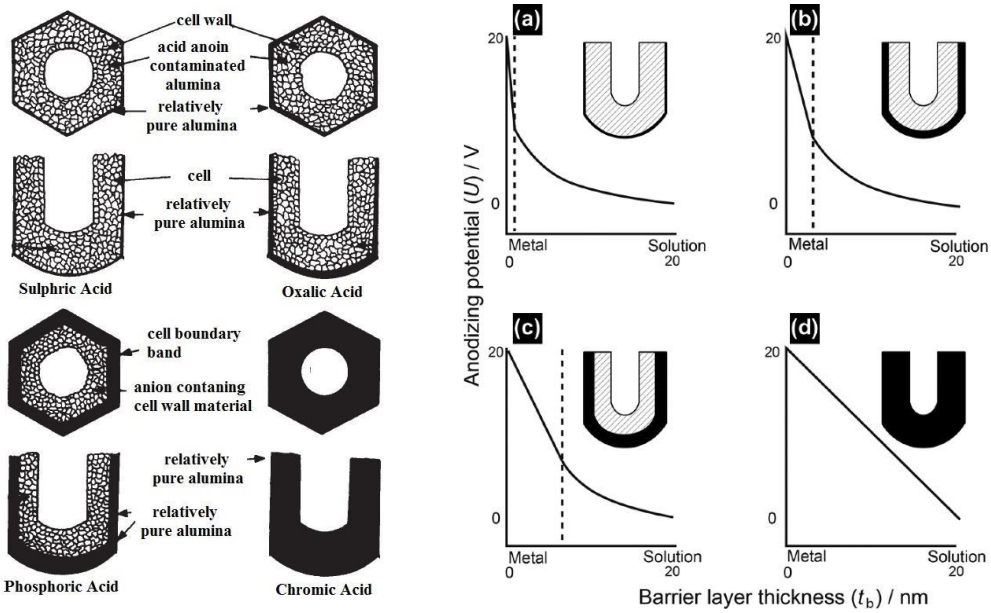

Fig. 1.4 The variation of thickness of inner and outer layers for the PAAs formed in (a) sulfuric, (b) oxalic, (c) phosphoric, and (d) chromic acid. [1, 14]

Moreover, the thickness of the barrier layer (t_b) is one of the most important structural parameters of PAA. The potential dependence of the barrier layer thickness has

also been known as "anodizing ratio ($AR = t_b/U$)", the inverse of which corresponds to the electric field across the barrier layer, and it determines the ionic current density. Extensive researches show that AR for various electrolytes was determined to be $AR \approx 1$ nm/V [10].

The main component of PAA film is amorphous, which is basically a recognized fact. However, it is still controversial that there might be some crystalline or microcrystalline islands in PAA, and they have not been detected easily might be attributed to its low content in PAA. Li et al. [17] recently reported that the crystallized PAA film can be fabricated under ultra-high anodizing voltage (700–1000 V). Crystalline phases (α-Al_2O_3, θ-Al_2O_3, and γ-Al_2O_3) in PAA were detected by X-ray diffraction (XRD). It was suggested caused by the crystalline transition of amorphous Al_2O_3 due to the combined action of heat and stress generated during ultra-high voltage.

1.3 Growth mechanism of porous-type anodic alumina film

1.3.1 Interface reactions

It is now widely accepted that the amorphous PAA films form by migration of Al^{3+} (from the substrate) and O^{2-} ions (from the electrolyte) through the anodic alumina under a high electric field.

The overall anodic reaction that leads to film growth is [1, 12, 18]:

$$2Al + 3H_2O \rightarrow Al_2O_3 + 6H^+ + e^- \quad [1.1]$$

The following elementary reactions are considered to be possibly occurring at the interfaces:

(i) At the aluminum/oxide interface:

$$Al \rightarrow Al^{3+}_{(ox)} + 3e^- \quad [1.2]$$

$$2Al^{3+}_{(ox)} + 3O^{2-}_{(ox)} \rightarrow Al_2O_3 \quad [1.3]$$

(ii) At the oxide/electrolyte interface:

$$2Al^{3+}_{(ox)} + 3O^{2-}_{(ox)} \rightarrow Al_2O_3 \quad [1.4]$$

$$Al_2O_3+6H^+_{(aq)} \rightarrow 2Al^{3+}_{(aq)} + 3H_2O_{(l)} \quad [1.5]$$

$$Al^{3+}_{(ox)} \rightarrow Al^{3+}_{(aq)} \quad [1.6]$$

$$2O^{2-}_{(ox)} \rightarrow O_{2(g)} + 4e^- \quad [1.7]$$

$$2H_2O_{(l)} \rightarrow O^{2-}_{(ox)} + OH^-_{(ox)} + 3H^+_{(aq)} \quad [1.8]$$

Eqs. 1.3 and 1.4 correspond to the formation of anodic oxide at the metal/oxide and oxide/electrolyte interfaces, respectively. Eq. 1.5 describes the dissolution of anodic alumina by Joule's heat-induced oxide dissolution and field-induced oxide dissolution. On the other hand, Eq. 1.6 occurs through field-assisted direct ejection of Al^{3+} ions from the metal/oxide interface through oxide into the electrolyte. Eqs. 1.5-1.7 decrease the net current efficiency (η_j) associated with the anodic oxide formation. Eq. 1.8 describes the heterolytic dissociation of water molecules at the oxide/electrolyte interface, which supplies oxygen anions to the metal/oxide interface to form anodic oxide [1].

1.3.2 Volume expansion

Oxidation of aluminum is a volume expansion process. The volume expansion during anodizing can be quantitatively expressed by the Pilling–Bedworth ratio (*PBR*) [1, 19]. The *PBR* is rigorously defined by the molar volume ratio of grown oxide (V_{ox}) to the consumed metal (V_m) as follows:

$$PBR = \frac{V_{ox}}{V_m} = \frac{M_{ox}\rho_m}{nM_m\rho_{ox}} \quad [1.9]$$

where M_{ox} is the molecular weight of oxide, M_m is the atomic weight of metal, n is the number of atoms of metal per one formula of the oxide, and ρ_m and ρ_{ox} are the densities of metal and oxide, respectively. In science on the corrosion of metals, *PBR* has been the basis for judging the protectiveness of a passivating oxide: if $PBR < 1$, the passivating oxide is under tensile stress and easily cracked; if $1 < PBR < 2$, the oxide covers the metal uniformly and is protective; if $PBR > 2$, the passivating oxide is under too much compressive stress and easily crumbles (e.g., iron oxide on iron). For anodic alumina

growth, PBR can be experimentally determined from the current efficiency (η_j) of oxide formation and the density (ρ_{AAO}) of the resulting AAO, provided that the composition of anodic oxide is well-defined. The densities of barrier- and porous-type AAOs have been reported to be in the range of $\rho_{AAO} = 2.7-3.5$ g/cm^3. Assuming composition stoichiometry of Al_2O_3 and $\rho_{AAO} = 3.0$ g/cm^3, *PBR* for AAO growth is 1.70 at 100% current efficiency (η_j). For porous-type AAO growth, *PBR* can vary between 1.02 and 1.58 due to the lower current efficiency (η_j = 60−93%) [1, 20]. On the other hand, it is also needs to be considered that the larger is the amount of incorporated acid anions during anodizing, the larger is the *PBR* [21].

1.3.3 Kinetics for generation of honeycomb structure

For the honeycomb structure of PAA, several models have been put forward in order to explain its formation. Among them, a field-assisted oxide dissolution [22-24] and stress-induced plastic flow models [25] are most frequently used. In addition, an oxygen bubble mold model [26-28] has been recently proposed for explanation of some unusual morphologies of anodic oxide films and phenomena occurring during their formation.

(I) Field-assisted oxide dissolution model

At the beginning of anodizing, a barrier type film forms at a reduced efficiency. Subsequently, formation of incipient pores at the film surface occurs by field-assisted dissolution of the oxide followed by a preferential growth of certain incipient pores that increases the local current density at the base of the pore. Then, due to the non-uniform distribution of the current and the low efficiency of film growth, major pores then develop following the field-assisted dissolution model [22-24].

Although the filed-assisted model well describes the oxide formation and growth process, it does not explain adequately some phenomena observed during anodizing including (1) higher concentration of Al^{3+} in the electrolyte after anodizing of Al than that originating from the formation of oxide, (2) much thicker oxide layers observed than the oxide thickness expected from the passed current and multiplied by the PBR, and (3)

incorporation of electrolyte species in the growing oxide layer [18].

(II) Plastic flow model

More recent work additionally revealed that the growth of PAA is most likely driven by the internal stresses and volume expansion [25] that develop in the oxide film during anodizing. In the porous film formation both factors, the oxide dissolution and stress generation at the metal/oxide interface, play a crucial role. However, it was found that only the dissolution of the oxide and ionic electromigration in the oxide layer are responsible for the formation of pores at the initial stage of anodization. For the steady-state conditions of oxide growth, a large compressive interfacial stress causes the lateral flow of oxide material from the center of pore base toward the cell boundaries and then upward in the pore walls.

(III) Oxygen bubble mold model

This model proposes that the porous structure of PAA is thanks to the decrease in current efficiency at the initial stage of anodizing, i.e., ion current (j_{ion}) decreases and electron current (j_e) increases. Where, j_{ion} is responsible for forming alumina (Eqs. 1.3 and 1.4) and j_e leads to the formation of oxygen bubbles (Eq. 1.7). The initial small bubbles adsorbe on the film/electrolyte interface before they becoming big enough to escape from the interface. Hence, the barrier layer continuously grows around the bubbles and the initial embryo-pores form. After the bubbles growing larger and overflowing out, the electrolyte fills the embryo-pores, causing an uneven current distribution. Subsequently, the stable growth of PAA can be explained by the field-assisted oxide dissolution model [26-28].

An important characteristic of these models is that they provide merely a mechanistic interpretation of steady-state growth of PAA, and therefore remain semiquantitative or qualitative models due to a large number of experimental factors that influence the growth of nanostructures [18].

1.3.4 Film evolution and electrochemical response during anodizing

PAA can be easily fabricated by anodizing of aluminum in acid electrolytes either under a constant potential or a constant current condition. In general, constant potential anodizing is widely employed for the fabrication of self-ordered PAA, because of the linear relation between the applied potential and the structural parameters of the resulting PAA (Fig. 1.2). However, constant current mode is actually more suitable for industrial production than is the constant potential mode.

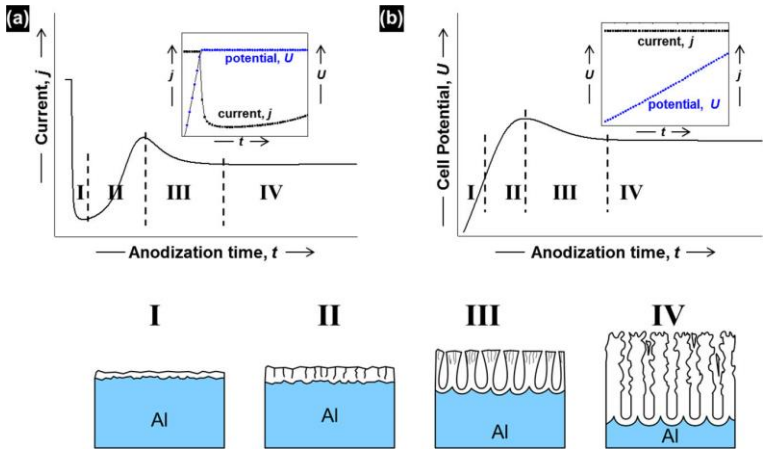

Fig. 1.5 Typical current-time curves during anodizing of aluminum and corresponding stages of the oxide layer formation. (A) Constant potential mode; (B) constant current mode. [1]

Fig. 1.5 shows the typical current-time curves during anodizing of aluminum and corresponding stages of the oxide layer formation. When the constant potential is applied (stage I), a compact barrier layer is developed on the aluminum surface and its thickening with time results in a rapid current (j) decrease to a minimum value. At stage II, current increases slightly to a local maximum due to the formation of penetration paths and pore embryos in the compact barrier layer. There are several theories on initial development of local imperfections from the compact barrier layer. According to O'Sullivan and Wood a local variation in the electric field strength on the oxide surface with some defects, impurities, pits, and sub-grain boundaries leads to a formation of a nonuniform thickness

of the barrier layer. Thompson and co-workers have proposed that local cracking of the initial barrier layer due to accumulated tensile stress ($PBR < 1$) may develop the paths for electrolyte penetration. It should also be mentioned that the electron current (j_e) used to form bubbles starts to generate in stage II, and X. Zhu correspondingly proposed the oxygen bubble mold model to explain the formation of the initial pore embryos. At stage III, the appearance of current overshoot has been related to the decrease of the initial pore density with the steady-state growth of major pores: pores increase in size by persistent merging with adjacent pores. These processes occur continuously until the curvatures of the aluminum/oxide interface are large enough to intersect each other. The growing major pores readjust their sizes and spatial arrangement to establish equilibrium morphology and the uniform electric field across the barrier layer. Finally, the steady-state conditions of oxide growth are attained (stage IV). For the case of constant current anodizing, the potential (U) changes as a function of time also attributed to the morphological instability of anodic film (stages I−IV) [1, 12, 18].

1.4 Anodizing technology

1.4.1 Anodizing equipment

In general, the entire process and setups used for the preparation of anodic alumina films are conducted using a two-electrode electrochemical cell with aluminum as the anode and platinum (also lead, stainless steel, graphite and other electrodes) as the cathode. Fig. 1.6a shows a conventional electrochemical cell in which both electros are aligned vertically and electrolyte can be agitated with a stirrer [29]. The horizontal arrangement of electrodes (Fig. 1.6b) in the electrochemical cell can also be used [30]. This type of the electrochemical cell is generally used for fabrication of anodic film with fixed area. The reaction heat during anodizing can be removed in time by stirring the electrolyte or heat conduction from the back of aluminum. Sometimes, more sophisticated electrolytic systems are used for anodizing of metallic substrates. In the overflow cell,

continuous circulation of the electrolyte to the anodized metal surface is ensured by a pump (Fig. 1.6c) [31, 32]. An anodized workpiece with large surface area can be easily fabricated with a limited-power anodizing equipment by scanning anodizing (change the position of the electrolyte sprayed on the aluminum) [32].

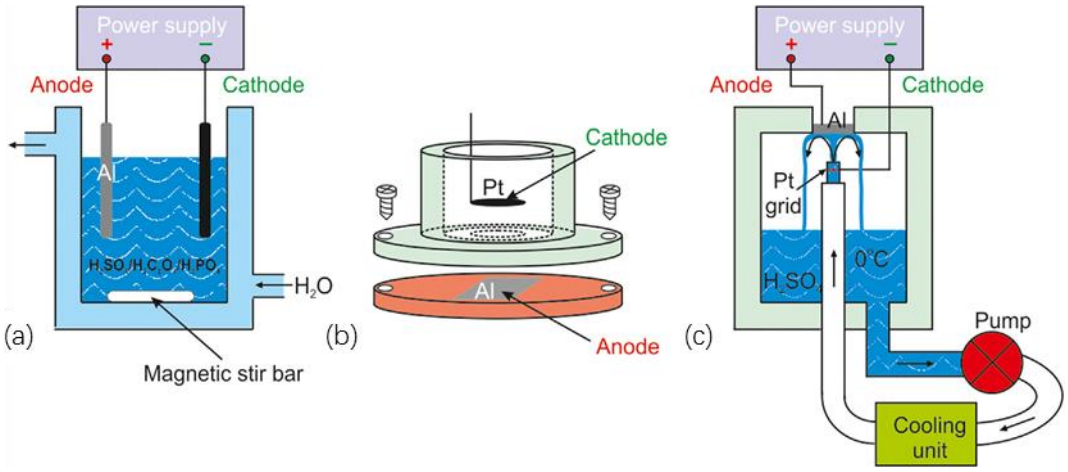

Fig. 1.6 Schematic representation of the conventional electrochemical cell with (a) vertical and (b) horizontal alignment of electrodes, and (c) overflow electrochemical cells used for anodizing. [18]

1.4.2 Mild, hard, and self-ordering anodizing processes

The structural features of PAA, especially pore diameter and interpore distance, are strongly influenced by the anodizing parameters, especially the type of electrolyte and applied voltage. Anodizing process can be mainly divided into mild, hard, and self-ordering anodizing processes according to different purposes.

(I) Mild anodizing (MA) or conventional anodizing

This type of anodizing process is relatively mild and slow (film growth rate = 2−10 μm/h). The resultant PAA film is nonuniform with disordered pore size and interpore distance. This thin disordered PAA film is generally used as a primer for surface coloring.

(II) Hard anodizing (HA)

HA is different from MA in that the former involves low electrolyte temperatures and high current densities or voltages. However, the underlying mechanisms of anodic film

growth are the same and are closely connected with the metallurgical history of the metal specimen [12]. The original meaning of hard anodizing is the formation of a hard PAA film with high Vickers hardness [33], while it has been recently used to describe the anodizing for fast fabrication of a PAA film [30] (Fig. 1.7). Although, a growth rate of PAA prepared by HA (50–100 μm/h [30]) can achieve1 to 2 orders of magnitude higher than that by MA, the HA film is prone to curling, cracking and distorted hole shape due to the burning and high voltage breakdown [34, 35]. The balance between heat generated by the anodizing process and heat removed during anodic film growth as the key factor for the initiation of burning. The generated heat mainly comes from Joule heating due to ionic current passing through the highly resistive oxide layer. This heat source is enhanced by increasing the applied current density or voltage, explaining why burning is an important issue for high speed anodizing processes [34]. The generated heat can be removed in time to reduce the risk of burning during HA process by using the powerful refrigeration equipment or pulse anodizing approach [36].

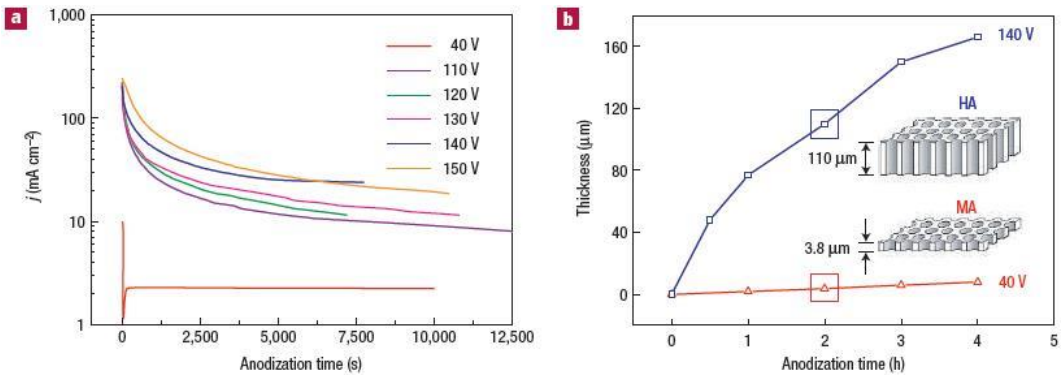

Fig. 1.7 (a) The MA and HA current-time curves in 0.3 M $H_2C_2O_4$. (b) PAA thickness dependence of time under MA (40 V) and HA (140 V). [30]

When the principal application of the anodic film, requires a hard and wear resistant surface, the hard anodizing process is adopted. Various aluminum alloys covered by hard porous alumina with Vickers hardness values of approximately HV = 400–500 are commercially available [37, 38]. Dilute electrolytes and low temperatures favour the growth of harder films, while more concentrated electrolytes and high temperatures and

longer process times (factors that will favour the dissolution of the film in the electrolyte) may produce soft, powdery, spongy or easily rubbed off films. For this reason, the cooling of the electrolyte is required to reduce the solvency power of the electrolyte, which helps in shifting the chemical equilibrium of forming and dissolution of the film to obtain a higher thickness. Decreasing the concentration of the acid electrolyte increases the abrasion resistance of the coating. The variation in the current density at low temperature (from 0 to -5°C) does not influence the abrasion resistance significantly [39]. However, between 10 and 20 °C the decrease of the current density leads to pronounced deterioration of the abrasion resistance and it is caused by increasing the porosity of the film [39]. The best abrasion resistance is obtained on pure aluminium, since the higher content of alloying elements, the more significant is the decrease in abrasion resistance [12].

(III) Self-ordered anodizing

The regularity of nanostructure of PAA is greatly affected by the anodizing voltage. Anodizing outside the self-ordering voltage window would eventually lead to a disordered growth of PAA. In addition, the anodizing duration, purity and surface state of aluminum, electric field distribution and other factors would also affect the regularity of PAA [40-43]. Therefore, the self-ordered PAA film has not been found since anodizing was proposed for decades.

Masuda et al. first fabricated the self-ordered PAA by a two-step anodizing in 1995 [4], which provides a new powerful method for preparing nanomaterials. Fig. 1.8 [1] presents the schematic of two-step anodizing. Firstly, a long-duration anodizing is conducted under the self-ordering voltage of the electrolyte to achieve a fully self-assembly barrier layer of PAA and a disordered pores in its top part (Fig. 1.8a). Then, the obtained PAA is removed by chemical dissolution, leaving ordered concaves on the aluminum substrate (Fig. 1.8b). Finally, anodizing once again by using the same conditions as the first step, thus, a highly ordered PAA film can be successfully fabricated (Fig. 1.8c). Fig. 1.8d exhibit a polydomain structure of the ordered PAA formed by two-step anodizing. The

lateral size of the defect-free domain increases with the anodizing time [1].

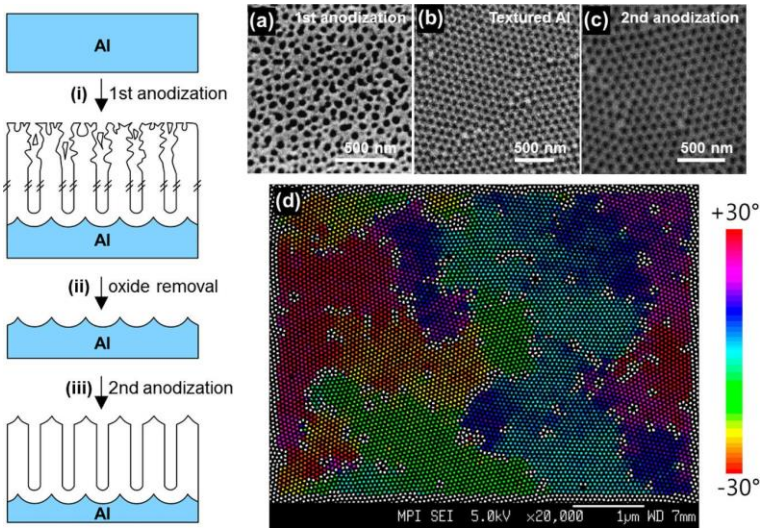

Fig. 1.8 The schematic of two-step anodizing and the corresponding scanning electron microscope (SEM) morphologies.[1]

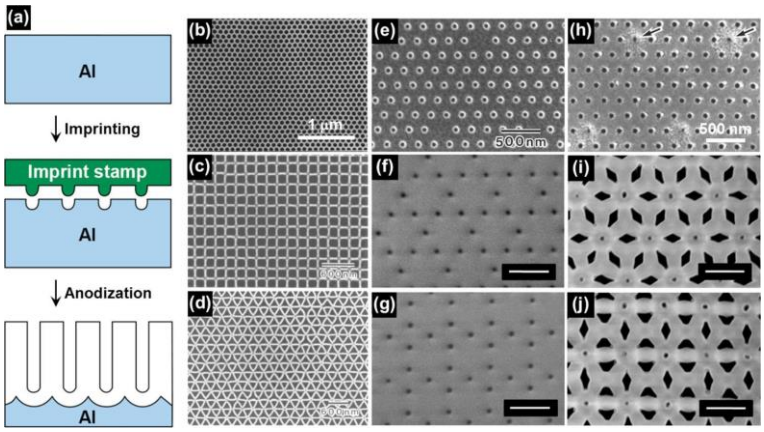

Fig. 1.9 Fabrication of ordered PAA with pre-pattern method (a) and the novel SEM morphologies of PAAs (b-j). [1]

In order to further reduce the experimental steps, Masuda et al. [41] afterward reported the fabrication of ideally ordered PAAs with a single-domain configuration over a few mm^2 area based on the idea of the two-step method. The process involved pre-patterning of the aluminum surface by transferring the pattern of a hard SiC stamp (mold) onto the aluminum by mechanical pressure (i.e., nanoimprinting), followed by anodizing (Fig. 1.9a). In order to obtain a highly ordered PAA film, the applied voltage of anodizing should match the pattern (the relationship between anodizing voltage and nanostructure

of PAA would be introduced in Chapter 1.4.3). Many pore array architectures can be fabricated by further extending this method (Fig. 1.9) [44, 45]. However, since the anodizing cannot proceed under the absolute self-ordering voltage, the non-hexagonal PAAs would become disordered after a long duration [1]. Therefore, it is still a challenge to prepare a large-area PAA films with ordered structures easily and quickly so far.

1.4.3 Electrolyte and anodizing voltage

The structural features of PAAs, especially pore diameter (D_p) and interpore distance (D_{int}), are strongly influenced by the type of electrolyte and applied voltage. Each electrolyte is characterized by a self-ordering voltage at which a highly ordered porous structure is obtained (Fig. 1.10). Beyond this voltage, the formed PAA is less ordered or even nonporous. For the ordered PAAs, D_{int} and the anodic voltage (U_a) have a linear relationship [1, 10, 46]:

$$D_{int} = \xi \times U_a \qquad [1.10]$$

During the mild anodizing, $\xi_{MA} = 2.5\ \mathrm{nm/V}$, and for hard anodizing, $\xi_{HA} = 2.0\ \mathrm{nm/V}$, as shown in Fig. 1.10. Notably, this simple linear relationship between D_{int} and U_a is not continuous, the formula is only applicable in a narrow voltage range for the specified electrolyte. For the mild anodizing, sulfuric acid with a self-ordering voltage of 19–25 V (corresponding D_{int}: 50–65 nm), oxalic acid of 40 V (100 nm), selenic acid of 42–48 V (95–112 nm), and phosphoric acid of 160–195 V (405–490 nm) have been reported [47]. Recently, more and more electrolytes with different self-ordering voltage range have been discovered to realize the continuous controllability of D_{int} of the ordered PAA, such as squaric acid[48], malonic acid [9], phosphonic acid [15], chromic acid[49], sodium hydrogen sulfate [50], citric acid [11], etc. These achievements greatly promote the application of self-ordered PAAs in the preparation of nanomaterials. For industrial applications, the mechanical properties and corrosion resistance of PAA film also depend on the electrolyte and the anodizing voltage. PAA films prepared in different electrolytes are generally different in D_{int}, D_p, and barrier layer thickness (t_b). The porosity (depends

on both D_{int} and D_p) greatly determines the hardness [37], while t_b affects the corrosion resistance [51].

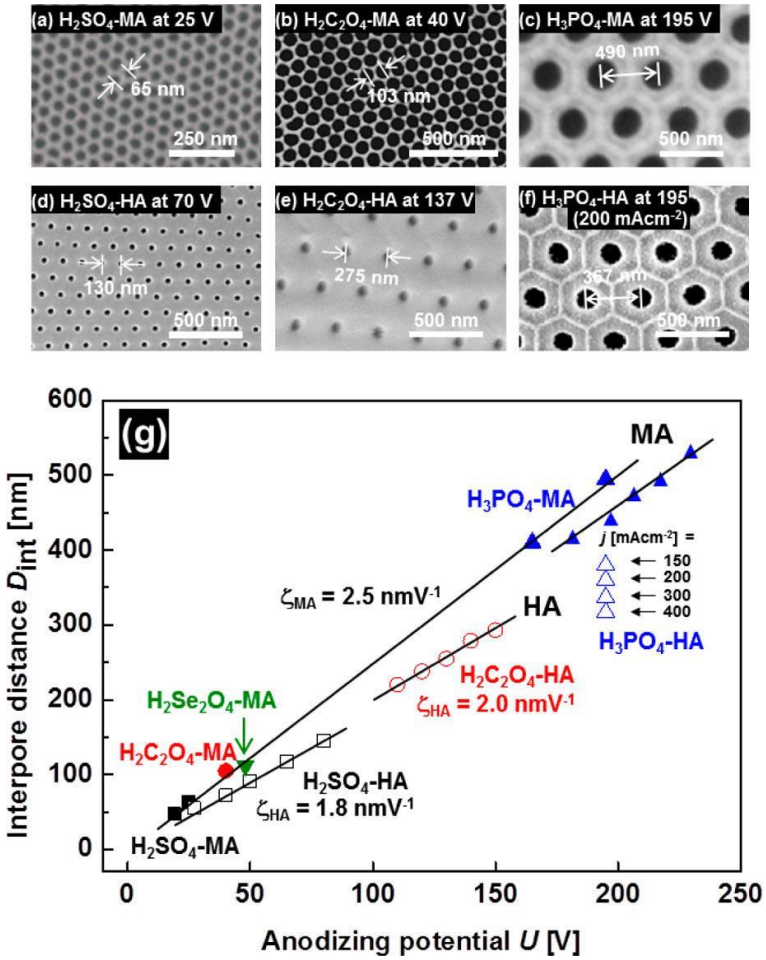

Fig. 1.10 The SEM morphologies of PAA fabricated in sulfuric, oxalic and phosphoric acid (a~f) and the linear relation between D_{int} and U_a (g). [1]

In general, chromic, sulfuric, and oxalic acids are the most widely used anodizing electrolytes in industry [6-8, 36, 52]. Chromic acid was used extensively in the early development of anodizing. The thickness of chromic acid PAA film is generally only 2–5 μm, the anodized aluminum workpiece in chromic acid can therefore maintain its original accuracy and surface roughness. Moreover, the chromic acid PAA film has good binding force with organic matter and is often used as the bottom layer for polymer coating. However, chromic acid has been gradually abandoned in recent years due to the high toxicity and serious environmental pollution. Sulfuric acid electrolytes are the most

commonly used in industry due to their low cost and ease of handling. In order to reduce the dissolution of the PAA film by sulfuric acid and reduce the risk of film burning caused by the accumulated reaction heat, a strong refrigeration equipment is usually required to maintain the electrolyte at a lower temperature. However, using a very dilute sulfuric acid electrolyte may present some problems during hard anodizing, as the electrolyte may freeze at low temperature; to prevent this, adequate circulation or vigorously stirring must be considered [12]. The resultant anodic alumina films tend to be rougher than films produced in more concentrated electrolytes; nevertheless they have good polishing properties and work well for components whose application requires grinding or polishing as a final operation [12]. Oxalic acid anodizing was widely used in Japan and Germany before 1939. Due to the low chemical dissolution of oxalic acid to PAA film, the porosity of oxalic acid PAA film is relatively low, and its corrosion resistance, wear resistance and electrical insulation are generally better than that of sulfuric acid PAA film [7]. However, the cost of oxalic acid anodizing is generally 3–5 times higher than that of sulfuric acid anodizing, besides, oxalic acid is easily decomposed during anodizing. Therefore, it is also subject to certain restrictions.

1.4.4 Post-sealing treatment

The porous structure of PAA film makes the area exposed to air much larger than the surface area of the aluminum workpiece, thereby increasing its corrosion rate. Therefore, the subsequent sealing processes on PAA via boiling water or metal salt solutions are frequently carried out to further improve its corrosion resistance [53-55]. The following reactions are considered to take place during sealing in water [12]:

$$Al_2O_3 + H_2O \rightarrow 2AlO(OH) \rightarrow Al_2O_3 \cdot H_2O \quad [1.11]$$

$$2AlO(OH) + 2H_2O \rightarrow Al_2O_3 \cdot 3H_2O \quad [1.12]$$

The formation of aluminium oxide monohydrate is indicated in Eq. 1.11 and the formation of aluminium oxide trihydrate is indicated in Eq. 1.12. Based on the SEM observations of the cross-sections (Fig. 1.11), the nanopores of PAA film were radually

sealed by hydration from the bottom to the top during immersion in boiling water [51]. Sealing of anodic alumina films can also be accomplished by immersion of the specimen in a hot aqueous 5 vol.% sodium dichromate solution or in a hot aqueous solution containing nickel acetate or cobalt acetate [12]. Another type of pore sealing is cold sealing, where chemicals like nickel fluoride are used to replace the hydrothermal precipitation to seal pores [33].

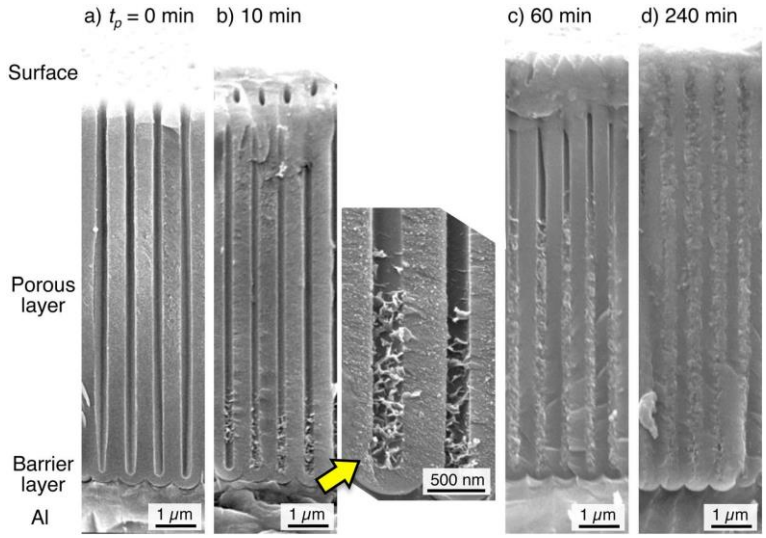

Fig. 1.11 SEM images of the fracture cross-section of PAA film immersed in boiling water for up to 240 min.[51]

1.5 Micro-arc oxidation

Micro-arc oxidation (MAO) [56-59], also known as plasma electrolytic oxidation (PEO) [60] or anodic spark oxidation (ASO) [61], is a kind of anodizing process that can be used on Al, Mg, Ti, Zr and other valve metals under high voltage (400–600 V) to fabricate MAO coating with excellent hardness (HV=1200–3500), wear resistance, corrosion resistance, high temperature resistance, catalytic ability, or biological compatibility, etc. [56, 58]. Up to now, the technology is mainly used in aerospace and artificial bone fields. Although MAO is also an electrochemical oxidation technology similar to anodizing with metals as anodes, MAO was not proposed and developed by the Soviet Union until the end of the 1960s due to the more complicated growth mechanism and higher requirements in equipment and energy consumption of MAO coating than that of traditional anodic

film [59, 62].

Generally, the whole MAO process can be divided into the formation and continuous growth of the coating. The working voltage of MAO breaks through the general voltage range of anodizing and enters the spark discharge section [62]. The particular micro discharges result in localized plasma reactions, with conditions of high temperature and pressure which promote the growth of oxide coating. Processes including melting, melt-flow, re-solidification, diffusion, sintering and densification of the growing oxide are parts of the MAO coating process [59, 60, 63-65].

Many growth mechanisms of MAO coating have been put forward and set up. Vijh [66] and Wood [67] et al. proposed that the microdischarge is a local avalanche breakdown of a solid insulating coating. T.B. Van et al. [68] suggested that the discharge always appears first in the weak part of the oxide film. A. Hickling et al. [69] considered that the initial discharge ignited in the gas bubbles between the coating and the electrolyte first and then induced the breakdown of the dielectric barrier layers. A. Epelfeld et al. [70] considered each microdischarge as a gas discharge occurring in a micropore of the oxide film, which was believed to be induced by an initial dielectric breakdown of a barrier layer in the bottom of the micropore. These mechanisms can help to explain qualitatively the stable growth of MAO coatings [59].

Compared with anodizing, which is based on acid electrolyte system, MAO electrolyte mainly are alkaline system such as, sodium silicate [56, 64], sodium phosphate [71, 72] and sodium aluminate [73, 74]. The performance of the MAO coating can be artificially changed by adding inorganic salts and functional particles [75]. Moreover, the performance and structure of the MAO coating can also be modified by using alternating current (AC) or high-frequency pulsed direct current (PDC, frequency of 50–1000 Hz, duty cycle of 10–90%) power supply [76, 77].

Fig. 1.11 presented the characteristics of the typical MAO coating. The formation process of MAO coating is similar to a volcanic eruption, and two distinct regions can be observed from its surface (Fig. 1.11a), a resolidified pool with a central hole and

accumulated particles with a nodular structure [56]. For the cross-sectional morphologies, a MAO coating has a three-layer structure (Fig. 1.11b-f), i.e. an outer porous layer, an inner dense layer and an amorphous alumina layer (AAL, several hundred nanometers thick, Fig. 1.11c-e) between the inner layer and the substrate. Due to the limitation of the characterization methods, the existence of AAL has not been confirmed until the past ten years. Zhu et al. [78] proposed that the main MAO voltage drop of applying the sample loaded on AAL layer (~1 V/nm), which provides new ideas for studying the growth kinetics of MAO coating. Actually, the similar "anodizing ratio" was used to explain the growth kinetics of PAA film [10]. It strongly implies the relationship between the growth mechanisms of MAO coating and PAA film.

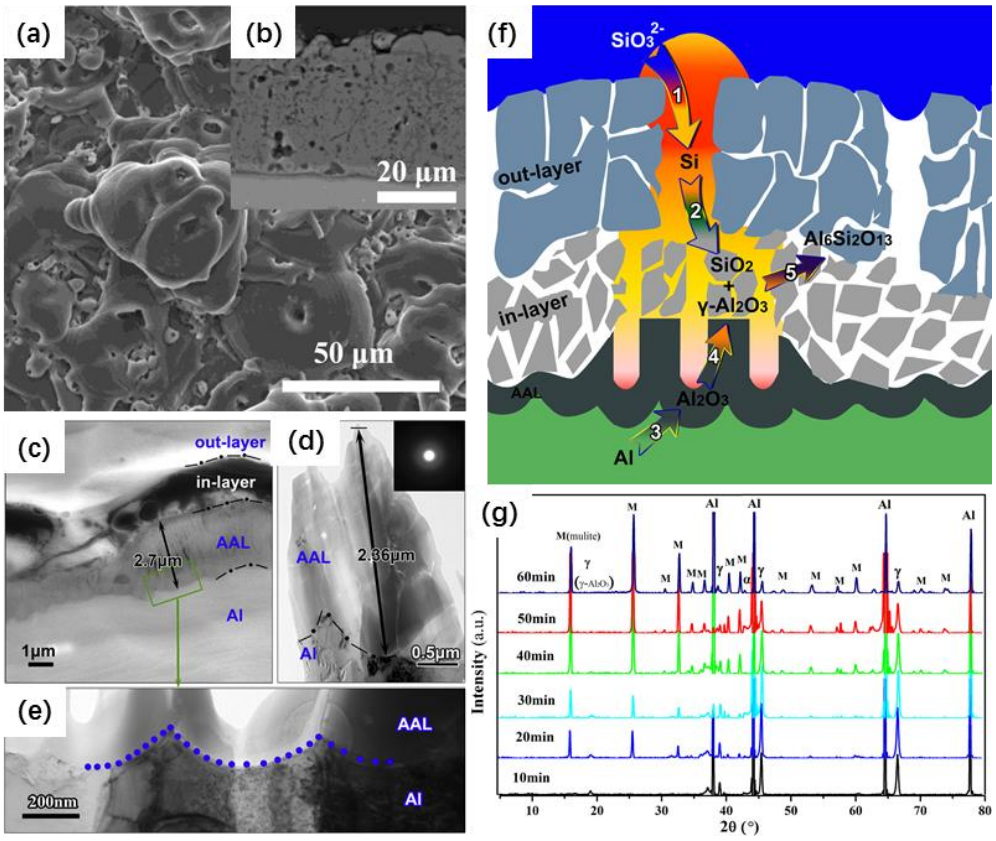

Fig. 1.11 Surface (a) and cross-sectional (b) SEM images of typical MAO coating; High resolution transmission electron microscope (HRTEM) images of MAO coating at the coating/substrate interface (c-e); Schematic illustration of the structural characteristics of MAO coating (f); X-ray diffraction (XRD) spectrum of the MAO coating fabricated in sodium silicate electrolyte system. [73, 78]

According to the research so far, anodizing cannot be converted into MAO by artificially increasing the voltage, and it also cannot be simply converted into anodizing by reducing the voltage during MAO too. The composition of the electrolyte directly determines which regime occurs during the electrochemical oxidation in it. The response voltage of anodizing in acid electrolyte is generally low, and the electric field strength applied to bubbles or defects is difficult to reach its breakdown value to form sparks. Artificially excessively increasing the voltage during anodizing will cause irreversible field-induced dissolution of the PAA film due to the breakdown of the oxidation balance [34]. When anodizing in some organic acids with low conductivity, sparks may occur due to the high working voltage. However, these sparks are destructive to the oxide film. During MAO in alkaline electrolyte, the negatively charged aluminosilicate colloid (take the sodium silicate electrolyte as an example) from the electrolyte moves continuously and adheres to the anode. When the high-energy micro-arc is generated, the sintered oxide is deposited in situ at the location where electrical breakdown occurs then cool down and crystallize [59]. The significant difference make the two technologies have been developed independently.

1.6 Research topic and contribution of this dissertation

Etidronic acid (1-hydroxyethane 1,1-diphosphonic acid, HEDP) is currently one of the most popular chelating agents and is widely used in various applications, such as in medicines, commercial washing agents, and inhibitors for corrosion protection [47]. More recently, the HEDP anodizing has been first proposed by Kikuchi et al. [47, 79] to fabricate ordered PAA (Fig. 1.12a and b) in the submicron level with special structural coloration (Fig. 1.12c) in 2015. For the engineering application, they found that the PAA film prepared in HEDP can retain a higher hardness (~ 600 HV) than can the PAA film fabricated via sulfuric acid hard anodizing (300–550 HV) due to the low porosity (as low as 4%) (Fig. 1.12e) [37]. Moreover, the barrier layer of PAA film prepared in HEDP is 10 times thicker than that prepared in sulfuric acid due to a high anodizing voltage (200–300

V, Fig. 1.12d) [47, 79].

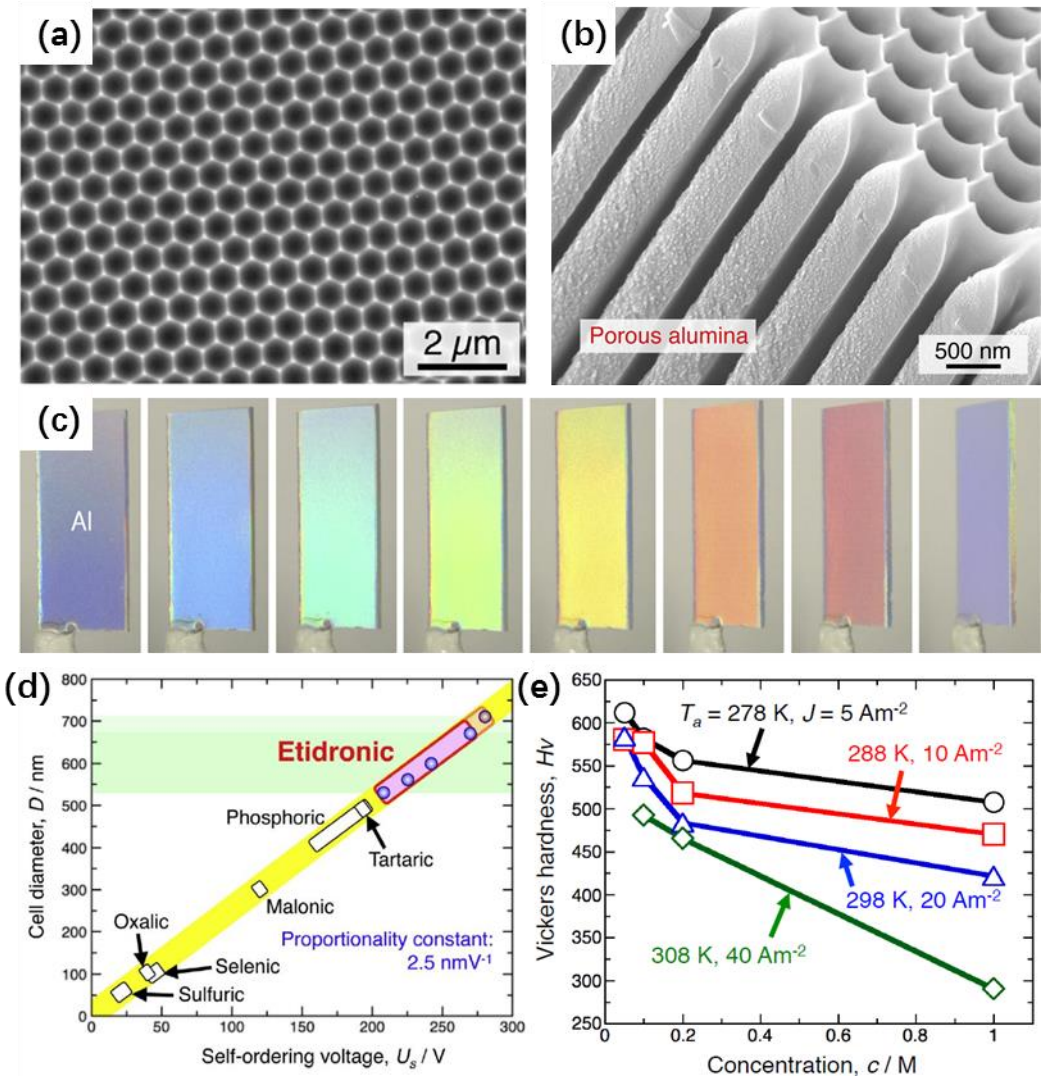

Fig. 1.12 SEM images of the dimple array (a) formed on the aluminum substrate after HEDP anodizing and the PAA film (b); (c) Bright structural colors at different viewing angles of the ordered PAA film fabricated via HEDP anodizing; (d) The relation between the cell diameter and the self-ordering voltage for PAA formed in various acidic electrolytes, as well as that for the PAA formed in HEDP; (e) Vickers hardness of the PAA film fabricated in HEDP. [37, 47]

Although the nanopores of PAA film can be subsequently sealed in boiling water or a metal salt solution for corrosion protection, the last corrosion-resistant structure in a corrosive environment is the bottom barrier layer, even after pore sealing [51]. Chu et al.

[10] reported the fabrication of PAA by anodizing at high voltages in several organic carboxylic acids, such as citric, malic, and tartaric acid solutions. However, these electrolytes easily lead to a burning phenomenon with local thickening of the PAA during anodizing, and it is difficult to form a uniform PAA film by anodizing at high voltages. Therefore, HEDP anodizing is a promising technology that can be used to prepare PAA film that is superior to currently known PAA films in terms of wear and corrosion resistance. However, rapidly fabricating the PAA film in HEDP with a certain thickness is still a challenge.

In order to explore the HEDP hard anodizing conditions for fast fabricating PAA film with super wear and corrosion resistance, we conducted a systematic study on HEDP anodizing on aluminum. According to the experience that the accumulated reaction heat on the anode must be removed to inhibit the burning of the PAA film fabricated in sulfuric acid under high current density (reducing the electrolyte temperature or using single-sided anodizing), we first investigated the single-sided anodizing of pure aluminum foil in low-temperature (0–10°C) HEDP solution at high current density (1–8 A/dm^2) in Chapter 3. The results showed that the response voltage quickly exceeded 300 V and rose to the usual MAO voltage range (>400 V), moreover, a stable spark appeared on the anode surface resulting in the typical structure of MAO coating. Namely, the stable MAO behavior in acid electrolyte was observed for the first time. More interestingly, the micro-arc would automatically extinguish and the oxidation voltage then remained at a stable value after a certain drop during the later stage of MAO in HEDP solution. After the characterization of the resultant coating, it was found that the coating has the composite structures of MAO coating and AAO film, i.e. MAO/AAO coating. Afterward, we followed the formation process of the MAO/AAO coating by SEM in Chapter 4. The burning of oxide film formed at the initial stage of oxidation and the effect of soft spark on this film were discussed, and a growth model of the MAO/AAO coating was proposed. Finally, we had successfully prepared HEDP hard anodized film on commercial aluminum alloy (6063T5) in Chapter 5 by changing the anodizing conditions to suppress

the burning of the initial film and avoid the MAO regime based on our previous work. The HEDP hard anodized film was confirmed to have super-high hardness, wear resistance and corrosion resistance that exceed the current anodized film.

References

[1] W. Lee, S.-J. Park, Porous anodic aluminum oxide: Anodization and templated synthesis of functional nanostructures, Chemical Reviews, 114 (2014) 7487-7556.

[2] G.D. Bengough, J.M. Stuart, Improved process of protecting surfaces of aluminium or aluminium alloys, GB Patent 223994, 1923.

[3] G.D. Bengough, J.M. Stuart, A process of producing a coloured surface on aluminium or aluminium alloys, GB Patent 223995, 1923.

[4] H. Masuda, K. Fukuda, Ordered metal nanohole arrays made by a two-step replication of honeycomb structures of anodic alumina, Science, 268 (1995) 1466-1468.

[5] Y. Nazarkina, K. Kamnev, A. Dronov, A. Dudin, A. Pavlov, S. Gavrilov, Features of porous anodic alumina growth in galvanostatic regime in selenic acid based electrolyte, Electrochimica Acta, 231 (2017) 327-335.

[6] Z. Ding, Mechanistic study of thin film sulfuric acid anodizing rate difference between Al2024 T3 and Al6061 T6, Surface and Coatings Technology, 357 (2019) 280-288.

[7] R.K. Choudhary, P. Mishra, V. Kain, K. Singh, S. Kumar, J.K. Chakravartty, Scratch behavior of aluminum anodized in oxalic acid: Effect of anodizing potential, Surface and Coatings Technology, 283 (2015) 135-147.

[8] D. Elabar, G.R. La Monica, M. Santamaria, F. Di Quarto, P. Skeldon, G.E. Thompson, Anodizing of aluminium and AA 2024-T3 alloy in chromic acid: Effects of sulphate on film growth, Surface and Coatings Technology, 309 (2017) 480-489.

[9] B. Sun, J. Li, X. Jin, C. Zhou, Q. Hao, X. Gao, Self-ordered hard anodization in malonic acid and its application in tailoring alumina taper-nanopores with continuously tunable periods in the range of 290–490nm, Electrochimica Acta, 112 (2013) 327-332.

[10] S.Z. Chu, K. Wada, S. Inoue, M. Isogai, Y. Katsuta, A. Yasumori, Large-scale fabrication of ordered nanoporous alumina films with arbitrary pore intervals by critical-potential anodization, Journal of The Electrochemical Society, 153 (2006).

[11] Y. Ma, Y. Wen, J. Li, J. Lu, Y. Li, Y. Yang, C. Feng, C. Hao, Z. Zhang, J. Hu, R. Sun, Pore nucleation mechanism of self-ordered alumina with large period in stable anodization in citric acid, Journal of The Electrochemical Society, 165 (2018) E311-E317.

[12] J.T. Alvarez, Hard anodic films for aluminum alloys, Department of Materials, The University of Manchester, 2018.

[13] G. Thompson, R. Furneaux, G. Wood, J. Richardson, J. Goode, Nucleation and growth of porous anodic films on aluminium, Nature, 272 (1978) 433-435.

[14] G. Thompson, G. Wood, Porous anodic film formation on aluminium, Nature, 290 (1981) 230-232.

[15] S. Akiya, T. Kikuchi, S. Natsui, N. Sakaguchi, R.O. Suzuki, Self-ordered porous alumina fabricated via phosphonic acid anodizing, Electrochimica Acta, 190 (2016) 471-479.

[16] H. Han, S.-J. Park, J.S. Jang, H. Ryu, K.J. Kim, S. Baik, W. Lee, In situ determination of the pore opening point during wet-chemical etching of the barrier layer of porous anodic aluminum oxide: nonuniform impurity distribution in anodic oxide, ACS Applied Materials & Interfaces, 5 (2013) 3441-3448.

[17] S. Li, Y. Li, S. Jin, J. Wu, Z. Li, X. Hu, Z. Ling, Fabrication of crystallized porous anodic aluminum oxide under ultra-high anodization voltage, Journal of The Electrochemical Society, 165 (2018) E623-E627.

[18] G.D. Sulka, Nanostructured anodic metal oxides, Elsevier, 2020.

[19] S. Berger, J. Kunze, P. Schmuki, D. LeClere, A.T. Valota, P. Skeldon, G.E. Thompson, A lithographic approach to determine volume expansion factors during anodization: Using the example of initiation and growth of TiO_2-nanotubes, Electrochimica Acta, 54 (2009) 5942-5948.

[20] K. Shimizu, K. Kobayashi, G. Thompson, G. Wood, Development of porous anodic films on aluminium, Philosophical Magazine A, 66 (1992) 643-652.

[21] I. Vrublevsky, V. Parkoun, V. Sokol, J. Schreckenbach, G. Marx, The study of the volume expansion of aluminum during porous oxide formation at galvanostatic regime, Applied Surface Science, 222 (2004) 215-225.

[22] A. Baron-Wiecheć, M.G. Burke, T. Hashimoto, H. Liu, P. Skeldon, G.E. Thompson, H. Habazaki, J.J. Ganem, I.C. Vickridge, Tracer study of pore initiation in anodic alumina formed in phosphoric acid, Electrochimica Acta, 113 (2013) 302-312.

[23] J. O'sullivan, G. Wood, The morphology and mechanism of formation of porous anodic films on aluminium, Proceedings of the Royal Society of London. A. Mathematical and Physical Sciences, 317 (1970) 511-543.

[24] T. Hoar, N. Mott, A mechanism for the formation of porous anodic oxide films on aluminium, Journal of Physics and Chemistry of Solids, 9 (1959) 97-99.

[25] S. Garcia-Vergara, P. Skeldon, G. Thompson, H. Habazaki, A flow model of porous anodic film growth on aluminium, Electrochimica Acta, 52 (2006) 681-687.

[26] M. Yu, Y. Chen, C. Li, S. Yan, H. Cui, X. Zhu, J. Kong, Studies of oxide growth location on anodization of Al and Ti provide evidence against the field-assisted dissolution and field-assisted ejection theories, Electrochemistry Communications, 87 (2018) 76-80.

[27] M. Yu, H. Cui, F. Ai, L. Jiang, J. Kong, X. Zhu, Terminated nanotubes: Evidence against the dissolution equilibrium theory, Electrochemistry Communications, 86 (2018) 80-84.

[28] S. Zhao, C. Li, T. Wei, C. Li, M. Yu, H. Cui, X. Zhu, A mathematical model for initiation and growth of anodic titania nanotube embryos under compact oxide layer, Electrochemistry Communications, 91 (2018) 60-65.

[29] H. Huang, J. Qiu, M. Sun, W. Liu, X. Wei, E. Sakai, K. Ito, A hard coating with MAO/AAO double layers prepared on aluminum in etidronic acid by DC oxidation, Surface and Coatings Technology, 360 (2019) 307-317.

[30] W. Lee, R. Ji, U. Gosele, K. Nielsch, Fast fabrication of long-range ordered porous alumina membranes by hard anodization, Nature Materials, 5 (2006) 741-747.

[31] M. Noormohammadi, Z.S. Arani, A. Ramazani, M.A. Kashi, S. Abbasimofrad, Super-fast fabrication of self-ordered nanoporous anodic alumina membranes by ultra-hard anodization, Electrochimica Acta, 354 (2020) 136766.

[32] L. Wen, Y. Wang, Y. Jin, B. Liu, Y. Zhou, D. Sun, Microarc oxidation of 2024 Al alloy using spraying polar and its influence on microstructure and corrosion behavior, Surface and Coatings Technology, 228 (2013) 92-99.

[33] A.l.o.o.p. R.Gabe, Hard anodizing—What do we mean by hard?, Metal Finishing, 100 (2002) 52-58.

[34] T. Aerts, I. De Graeve, H. Terryn, Study of initiation and development of local burning phenomena during anodizing of aluminium under controlled convection, Electrochimica Acta, 54 (2008) 270-279.

[35] T. Aerts, I. De Graeve, H. Terryn, Anodizing of aluminium under applied electrode temperature: Process evaluation and elimination of burning at high current densities, Surface and Coatings Technology, 204 (2010) 2754-2760.

[36] M. Bononi, R. Giovanardi, A. Bozza, Pulsed current hard anodizing of heat treated aluminum alloys: Frequency and current amplitude influence, Surface and Coatings Technology, 307 (2016) 861-870.

[37] T. Kikuchi, A. Takenaga, S. Natsui, R.O. Suzuki, Advanced hard anodic alumina coatings via etidronic acid anodizing, Surface and Coatings Technology, 326 (2017) 72-78.

[38] G. Alcalá, P. Skeldon, G.E. Thompson, A.B. Mann, H. Habazaki, K. Shimizu, Mechanical properties of amorphous anodic alumina and tantala films using nanoindentation, Nanotechnology, 13 (2002) 451-455.

[39] P. Kwolek, Hard anodic coatings on aluminum alloys, Advances in Manufacturing Science and Technology, 41 (2017) 35-46.

[40] H. Masuda, M. Satoh, Fabrication of gold nanodot array using anodic porous alumina

as an evaporation mask, Japanese Journal of Applied Physics, 35 (1996) L126.

[41] H. Masuda, H. Asoh, M. Watanabe, K. Nishio, M. Nakao, T. Tamamura, Square and triangular nanohole array architectures in anodic alumina, Advanced Materials, 13 (2001) 189-192.

[42] S.-K. Hwang, S.-H. Jeong, H.-Y. Hwang, O.-J. Lee, K.-H. Lee, Fabrication of highly ordered pore array in anodic aluminum oxide, Korean Journal of Chemical Engineering, 19 (2002) 467-473.

[43] I.S. Molchan, T.V. Molchan, N.V. Gaponenko, P. Skeldon, G.E. Thompson, Impurity-driven defect generation in porous anodic alumina, Electrochemistry Communications, 12 (2010) 693-696.

[44] L. Wen, R. Xu, Y. Mi, Y. Lei, Multiple nanostructures based on anodized aluminium oxide templates, Nature Nanotechnology, 12 (2017) 244-250.

[45] S. Zhao, K. Chan, A. Yelon, T. Veres, Novel structure of AAO film fabricated by constant current anodization, Advanced Materials, 19 (2007) 3004-3007.

[46] G.D. Sulka, K.G. Parkoła, Anodising potential influence on well-ordered nanostructures formed by anodisation of aluminium in sulphuric acid, Thin Solid Films, 515 (2006) 338-345.

[47] T. Kikuchi, O. Nishinaga, S. Natsui, R.O. Suzuki, Fabrication of self-ordered porous alumina via etidronic acid anodizing and structural color generation from submicrometer-scale dimple array, Electrochimica Acta, 156 (2015) 235-243.

[48] T. Kikuchi, T. Yamamoto, S. Natsui, R.O. Suzuki, Fabrication of anodic porous alumina by squaric acid anodizing, Electrochimica Acta, 123 (2014) 14-22.

[49] D. Elabar, T. Hashimoto, J. Qi, P. Skeldon, G.E. Thompson, Effect of low levels of sulphate on the current density and film morphology during anodizing of aluminium in chromic acid, Electrochimica Acta, 196 (2016) 206-222.

[50] R. Kondo, T. Kikuchi, S. Natsui, R.O. Suzuki, Fabrication of self-ordered porous alumina via anodizing in sulfate solutions, Materials Letters, 183 (2016) 285-289.

[51] Y. Suzuki, K. Kawahara, T. Kikuchi, R.O. Suzuki, S. Natsui, Corrosion-resistant

porous alumina formed via anodizing aluminum in etidronic acid and its pore-sealing behavior in boiling water, Journal of The Electrochemical Society, 166 (2019) C261-C269.

[52] A. Bozza, R. Giovanardi, T. Manfredini, P. Mattioli, Pulsed current effect on hard anodizing process of 7075-T6 aluminium alloy, Surface and Coatings Technology, 270 (2015) 139-144.

[53] C. Lee, K. Oh, D. Lee, Y. Kim, H. Yoon, D.-W. Park, M. Gab Kim, K. Lee, J. Choi, Self-sealing anodization approach to enhance micro-Vickers hardness and corrosion protection of a die cast Al alloy, Journal of Physics and Chemistry of Solids, 103 (2017) 87-94.

[54] Y. Wu, W. Zhao, W. Wang, L. Wang, Q. Xue, Novel anodic oxide film with self-sealing layer showing excellent corrosion resistance, Scientific Reports, 7 (2017) 1344.

[55] Y. Yang, J. Cheng, S. Liu, H. Wang, P. Dong, Effect of $NaAlO_2$ sealing on corrosion resistance of 2024 aluminum alloy anodized film, Materials and Corrosion, 70 (2019) 120-127.

[56] H. Huang, X. Wei, J. Yang, J. Wang, Influence of surface micro grooving pretreatment on MAO process of aluminum alloy, Applied Surface Science, 389 (2016) 1175-1181.

[57] J. Wang, S. Huang, M. He, P. Wangyang, Y. Lu, H. Huang, L. Xu, Microstructural characteristic, outward-inward growth behavior and formation mechanism of MAO ceramic coating on the surface of ADC12 Al alloy with micro-groove, Ceramics International, 44 (2018) 7656-7662.

[58] X. Wei, H. Huang, M. Sun, W. Liu, J. Qiu, Effects of honeycomb pretreatment on MAO coating fabricated on aluminum, Surface and Coatings Technology, 363 (2019) 265-272.

[59] M. Kaseem, S. Fatimah, N. Nashrah, Y.G. Ko, Recent progress in surface modification of metals coated by plasma electrolytic oxidation: Principle, structure,

and performance, Progress in Materials Science, (2020) 100735.

[60] Y. Cheng, T. Wang, S. Li, Y. Cheng, J. Cao, H. Xie, The effects of anion deposition and negative pulse on the behaviours of plasma electrolytic oxidation (PEO)—A systematic study of the PEO of a Zirlo alloy in aluminate electrolytes, Electrochimica Acta, 225 (2017) 47-68.

[61] M. Fazel, H. Salimijazi, M. Shamanian, Improvement of corrosion and tribocorrosion behavior of pure titanium by subzero anodic spark oxidation, ACS Applied Materials & Interfaces, 10 (2018) 15281-15287.

[62] A.L. Yerokhin, X. Nie, A. Leyland, A. Matthews, S.J. Dowey, Plasma electrolysis for surface engineering, Surface and Coatings Technology, 122 (1999) 73-93.

[63] Y.-l. Cheng, Z.-g. Xue, Q. Wang, X.-Q. Wu, E. Matykina, P. Skeldon, G.E. Thompson, New findings on properties of plasma electrolytic oxidation coatings from study of an Al–Cu–Li alloy, Electrochimica Acta, 107 (2013) 358-378.

[64] Y. Cheng, F. Wu, J. Dong, X. Wu, Z. Xue, E. Matykina, P. Skeldon, G.E. Thompson, Comparison of plasma electrolytic oxidation of zirconium alloy in silicate- and aluminate-based electrolytes and wear properties of the resulting coatings, Electrochimica Acta, 85 (2012) 25-32.

[65] Y. Cheng, J. Cao, M. Mao, H. Xie, P. Skeldon, Key factors determining the development of two morphologies of plasma electrolytic coatings on an Al–Cu–Li alloy in aluminate electrolytes, Surface and Coatings Technology, 291 (2016) 239-249.

[66] A.K. Vijh, Sparking voltages and side reactions during anodization of valve metals in terms of electron tunnelling, Corrosion Science, 11 (1971) 411-417.

[67] J. O'dwyer, The theory of avalanche breakdown in solid dielectrics, Journal of Physics and Chemistry of Solids, 28 (1967) 1137-1144.

[68] T.B. Van, S.D. Brown, G.P. Wirtz, Mechanism of anodic spark deposition, American Ceramic Society Bulletin, Cincinnati, OH, USA, 1977.

[69] A. Hickling, M. Ingram, Contact glow-discharge electrolysis, Transactions of the

Faraday Society, 60 (1964) 783-793.

[70] A. Epelfeld, V. Lyudin, O. Dunkin, O. Nevskaya, Discharge in the metal-oxide-electrolyte system during microarc oxidation with alternating current, Bulletin of the Russian Academy of Sciences-Physics, 64 (2000) 610-613.

[71] Q. Cai, L. Wang, B. Wei, Q. Liu, Electrochemical performance of microarc oxidation films formed on AZ91D magnesium alloy in silicate and phosphate electrolytes, Surface and Coatings Technology, 200 (2006) 3727-3733.

[72] Q. Wen, F.H. Cao, Y.Y. Shi, Z. Zhang, J.Q. Zhang, The effect of phosphate on MAO of AZ91D magnesium using AC power source, Materials and Corrosion, 59 (2008) 819-824.

[73] Y.-l. Cheng, M.-k. Mao, J.-h. Cao, Z.-m. Peng, Plasma electrolytic oxidation of an Al-Cu-Li alloy in alkaline aluminate electrolytes: A competition between growth and dissolution for the initial ultra-thin films, Electrochimica Acta, 138 (2014) 417-429.

[74] Y. Cheng, J. Cao, Z. Peng, Q. Wang, E. Matykina, P. Skeldon, G.E. Thompson, Wear-resistant coatings formed on Zircaloy-2 by plasma electrolytic oxidation in sodium aluminate electrolytes, Electrochimica Acta, 116 (2014) 453-466.

[75] X. Lu, M. Mohedano, C. Blawert, E. Matykina, R. Arrabal, K.U. Kainer, M.L. Zheludkevich, Plasma electrolytic oxidation coatings with particle additions–A review, Surface and Coatings Technology, 307 (2016) 1165-1182.

[76] J.-H. Wang, M.-H. Du, F.-Z. Han, J. Yang, Effects of the ratio of anodic and cathodic currents on the characteristics of micro-arc oxidation ceramic coatings on Al alloys, Applied Surface Science, 292 (2014) 658-664.

[77] V. Dehnavi, B.L. Luan, D.W. Shoesmith, X.Y. Liu, S. Rohani, Effect of duty cycle and applied current frequency on plasma electrolytic oxidation (PEO) coating growth behavior, Surface and Coatings Technology, 226 (2013) 100-107.

[78] L. Zhu, Z. Guo, Y. Zhang, Z. Li, M. Sui, A mechanism for the growth of a plasma electrolytic oxide coating on Al, Electrochimica Acta, 208 (2016) 296-303.

[79] A. Takenaga, T. Kikuchi, S. Natsui, R.O. Suzuki, Exploration for the Self-ordering

of Porous Alumina Fabricated via Anodizing in Etidronic Acid, Electrochimica Acta, 211 (2016) 515-523.

Chapter 2 Materials, Experiment and Characterizations

2.1 Materials

1N30 aluminum foil (with a chemical composition of ≥ 99.3 wt% Al and ≤ 0.7 wt% Si+Fe) with a thickness of 0.1 mm was purchased from Taiho Kogyo Corporation (Toyota, Japan). 6063T5 aluminum alloy (with a chemical composition of 0.40 wt% Si, 0.15 wt% Fe, 0.00 wt% Cu, 0.02 wt% Mn, 0.48 wt% Mg, 0.00 wt% Cr, 0.00 wt% Zn, 0.01 wt% Ti, <0.05 wt% others and balance Al, provided by the manufacturer) with a thickness of 2 mm was obtained from UACJ Corporation (Tokyo, Japan). Etidronic acid ($CH_3C(OH)[PO(OH)_2]_2$, HEDP, 4.2 M) was purchased from Tokyo Chemical Industry (Tokyo, Japan). Perchloric acid ($HClO_4$, 60 wt%), copper chloride ($CuCl_2$, 95.0%), hydrochloric acid (HCl, 35%), sodium chloride (NaCl, 99.5%), acetone ($(CH_3)_2CO$, 99.0%) and ethanol (C_2H_5OH, 99.5%) were obtained from Nacalai Tesque Incorporation (Nacalai, Japan).

2.2 Sample preparation

2.2.1 Pre-treatment of sample

The 1N30 aluminum foil with a cutted dimensions of 25 mm× 25 mm×0.1 mm was used for one side anodizing, it has a mirror bright finish and no need to be further polished. The 6063T5 aluminum alloy was cut into rectangular pieces (40 mm × 10 mm × 2 mm) and ground with abrasive papers (320–800#). Then, the pieces were electrochemically polished in a $HClO_4/C_2H_5OH$ mixture (v:v = 1:4) at 25 V for 2.5 min under −5–5°C. Finally, all samples were were cleaned with acetone for 10min and dried in a stream of cold air for use. Fig. 2.1 shows the polished 6063T5 aluminum alloy.

Fig. 2.1 The appearance of the polished 6063T5 aluminum alloy

2.2.2 Anodizing

The 1N30 aluminum foil and 6063T5 aluminum alloy were anodized in the one-side and conventional mode, respectively. One-side anodizing refers to the method in which samples are packaged by special fixtures, leaving only a partial area for anodizing. Fig. 2.2 shows the schematic diagram of electrolytic cell with the fixture for one-side anodizing. The 1N30 aluminum foils were clamped in the fixture with one side exposed, and the exposed area was limited by a silicone O-ring to 1.8 cm^2. The foils were connected the anode through a copper wire and a 304 stainless steel as cathode. The electrolytic cell was a 300mL double-walled glass beaker, and the temperature of electrolyte can be adjusted by injecting circulating cooled water/ethanol mixture (CCA-1111, Eyela, Japan) into the interlayer of the beaker. As to the anodizing of 6063T5 aluminum alloy, the exposed part of the sealed 6063T5 samples (exposed area of 3.8 cm^2) were directly immersed in the anodizing electrolyte as the anode instead of using the one-side fixture.

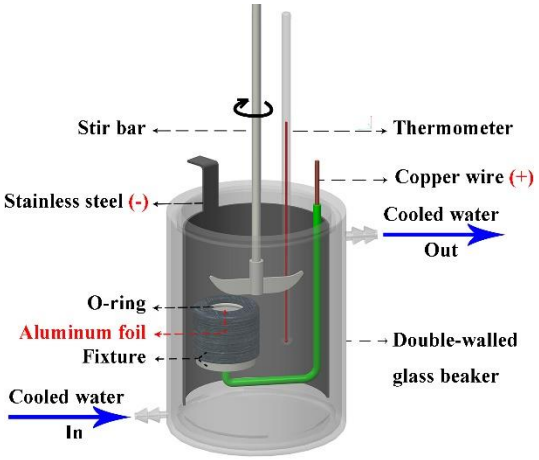

Fig. 2.2 The schematic diagram of electrolytic cell

The anodizing was conducted in 0.2 M HEDP solution with different temperatures. A power supply (PWR1201H, Kikusui Electronics, Japan) was used for anodizing and the electric signals were measured during the anodizing process. During the anodizing, the solution was strongly stirred with a mechanical stirring bar. After the anodizing, the samples were ultrasonically washed with deionized water at room temperature, and then dried in a cooled air stream for characterization.

In order to investigate the performance of HEDP anodized film prepared on 6063T5 aluminum alloy, the hard-anodized film fabricated in sulfuric acid solution was used to compare with that fabricated in HEDP solution. The details of sulfuric acid hard anodizing as follows: 30 wt% sulfuric acid, temperature of −5 ± 0.5 °C, 3 A/dm^2 current density, and 75% duty cycle (to avoid burning). The thicknesses of anodized films used for performance comparison were adjusted to ~40 μm. Fig. 2.3 shows the SEM images of the hard-anodized film prepared in sulfuric acid.

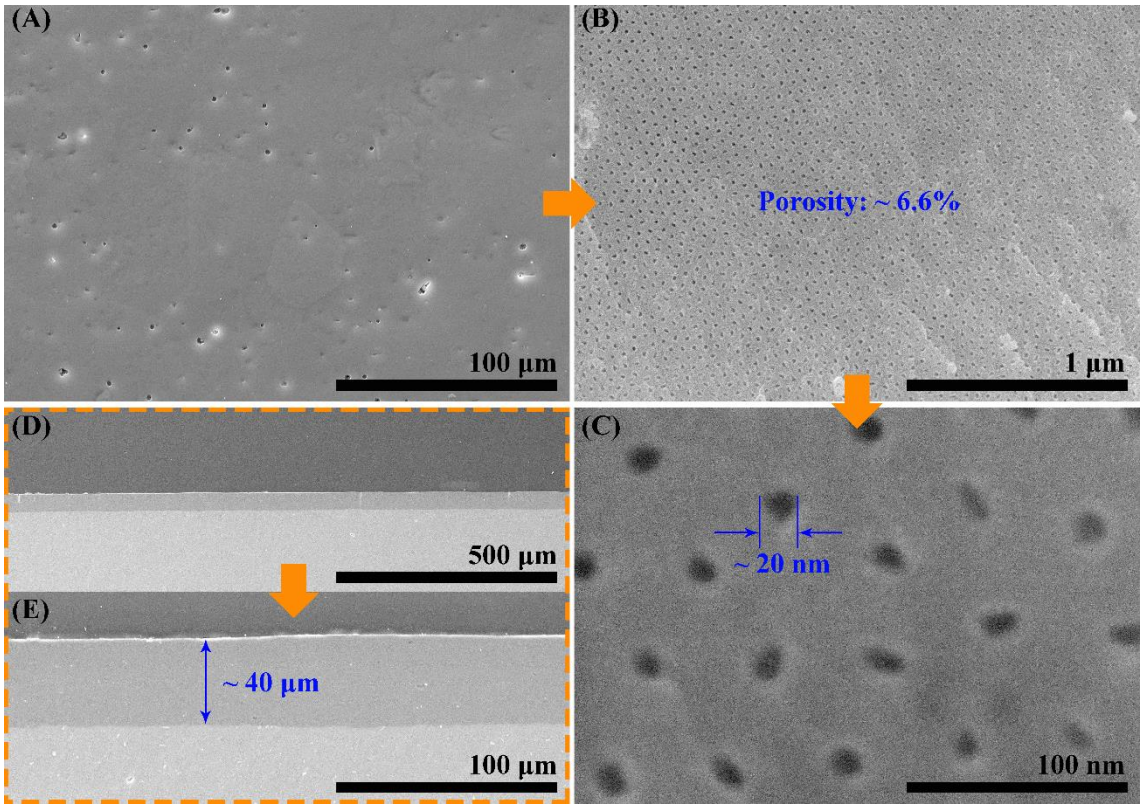

Fig. 2.3 Surface (A-C) and cross-sectional (D and E) morphologies of the hard-anodized film fabricated in sulfuric acid on 6063T5 aluminum alloy.

2.3 Characterization

2.3.1 Thickness of film

The thickness of the samples before and after anodizing was measured by a spherical face digimatic micrometer (395-271-30, Mitutoyo, USA). The thicknesses of the films were pre-determined after anodizing with an eddy current thickness gauge (MiniTest 735, Elektrophysik, Germany).

2.3.2 Scanning electron microscopy (SEM)

The broken sections of anodized films were fabricated to observe the real cross-sections, especially the barrier layer; the polished cross-sections of the anodized films after mounting in epoxy resin were prepared for thickness and hardness measurements. For the observation on the back of barrier layer, sample preparation was carried out with the following four steps: 1) the anodized 6063T5 specimen was cut into two pieces along the thickness direction with a saw to expose the aluminum substrate; 2) the specimens were immersed in a 0.5 M $CuCl_2$ solution at room temperature to completely dissolve the aluminum substrate and a free-standing porous alumina film without the aluminum substrate was obtained via the chemical dissolution processes, and the back of barrier layer could be observed.

The morphologies of the anodized films were examined in detail by SEM (ERA-8900, Elionix, Japan) and (S-4300 and SU-70, Hitachi, Japan). Before the SEM observation, a thin platinum layer was coated on the samples to increase the conductivity. The pore diameter, porosity, and thickness of the anodized films were measured from the SEM images using software (Image J 1.42q).

2.3.3 Energy dispersive spectrometry (EDS) and X-ray photoelectron spectroscopy (XPS)

The elemental compositions and distributions of the anodized films were evaluated via EDS coupled to the SEM (SU-70 and ERA-8900) and XPS (ESCA5400, ULVAC-PHI,

Japan). The samples used for the XPS measurements were etched with argon ions for 5 min in advance, and the XPS spectra were corrected by reference to the Ar2p3/2 (242 eV) and Ar2p1/2 (244 eV) peaks.

2.3.4 X-ray diffractometer (XRD) and selected-area electron diffraction (SAED)

The crystal state of the films was determined by using XRD ((X'pert Pro MPD, Malvern Panalytical, Netherlands) and (SmartLab9K-INP, Rigaku, Japan)) and SAED analysis via a transmission electron microscope (TEM, HT7830, Hitachi, Japan) at 120 kV. For preparation of TEM sample, the porous alumina film obtained via the chemical dissolution processes was cut on the barrier layer side using a focused ion beam (FIB, FB2000A, Hitachi, Japan).

2.3.5 Microhardness test

The hardness H_{IT} and elastic modulus E_{IT} of the films were measured on their cross-sections at a load of 0.025 N for 10 s by a nanoindentation tester (DUH-211, Shimadzu, Japan) equipped with a Berkovitch diamond indenter. The hardness was also evaluated via the Vickers method at a load of 0.1 N (HM-200, Mitutoyo, Japan).

2.3.6 Wear resistance

The wear resistance of the film was evaluated by the reciprocating motion approach of an UMT TriboLab (BRUKER, USA) for 30 min. A GCr15 steel ball (Φ 9.5 mm, HRC 62) and the anodized aluminum block were set as the friction pairs. The load was 10 N and the frequency was 5 Hz. The wear scars were examined with a profilometer (Form Talysurf Intra, Taylor Hobson, UK) and SEM-EDS.

2.3.7 Corrosion resistance

An electrochemical workstation (CS2350H, Corrtest, China) was used to analyze the corrosion resistance of the films with electrochemical impedance spectroscopy (EIS) and

potentiodynamic polarization tests in a 3.5 wt% NaCl solution at room temperature (20–25 °C). A saturated calomel electrode (SCE), a platinum plate, and the anodized aluminum were set as the reference, counter, and working electrodes, respectively. Before the test, the samples were sealed with the evaluated areas of 1 cm^2 , then immersed in NaCl solution for 1 h to reach a steady open-circuit potential (OCP). Afterwards, an EIS measurement was performed by applying the signal amplitude of 10 mV on an OCP over a frequency from 10^{-2} to 10^5 Hz, 1 point per decade. Potentiodynamic polarization was carried out by applying a ± 250 mV polarization based on the OCP at a scanning rate of 1 mV/s. Zview and Cview software were used to simulate the EIS and polarization data, respectively.

Chapter 3 A hard coating with MAO/AAO double layers prepared on aluminum in HEDP

3.1 Introduction

Anodizing is a process that electric current flows through an electrolyte such as chromic acid, sulfuric acid, oxalic acid, and phosphoric acid, where aluminium sheet is used as anode [1, 2]. As a porous amorphous film with a honeycomb structure, the obtained anodic aluminum oxide (AAO) has been widely applied in the fields of corrosion protection [3, 4], mechanical protection [5-7], coloring [8], production of capacitors [9], and nano-template [10, 11].

Hard anodizing is a process that uses a combination of low temperature (263–268 K [12]) and high voltage or current densities to produce AAO with excellent wear and corrosion-resistant properties. The hard AAO processed in a sulphuric acid solution has been widely used in industrial fields because it keeps the best mechanical performance (4–6 GPa [5, 13]) in the anodizing field. However, the requirements on the performance of workpieces have become increasing higher with the development of technology. For instance, the AAO film keeping a hardness higher than 7 GPa has great prospects in partially replacing the chromium/nickel plating coatings [14] that have serious industrial pollution. Many researchers have studied the factors affecting hardness, e.g. type of electrolyte, electrical parameters and reaction temperature [12], but the improvement of the performance of AAO was still limited due to the relatively fixed porosity of AAO prepared in the corresponding electrolyte.

Recently, Kikuchi et al. [6, 8, 15, 16] first proposed using etidronic acid, 1-hydroxyethane -1,1%-diphosphonic acid (HEDP), as an electrolyte for anodizing. It was found that the AAO films prepared in HEDP possessed a high hardness of Hv=610, which increased to Hv=769 after thermal treatment [6]. In the conventional anodizing using

sulfuric, oxalic, and phosphoric electrolyte solutions, the porosity of the obtained AAO was approximately 0.1–0.35 [17, 18]. Hence, the extremely low porosity (~0.04) of AAO films prepared in HEDP was suggested to interpret the superior performance. However, the extremely low growth rate (~7 μm/h) cannot meet industrial production requirements.

After that, Sepúlveda et. al. [19] compared the growth rate of self-ordering AAO films prepared by potentiostatic anodizing at 270 V in HEDP solution at 298 and 313 K, respectively. They concluded that increasing the electrolyte temperature led to increasing the growth rate of the AAO films from 3.9 μm/h at 298 K to 20 μm/h at 313 K, and accelerating the self-organization of the AAO. It is proposed that increasing the electrolyte temperature would reduce the electrolyte viscosity and increase the electric conductivity of the anodizing bath, which results in higher forming rate of the AAO films. However, it is also generally believed that the AAO film would be burnt down under the high current densities, then the oxidation balance is broken and the aluminum substrate is continuously dissolved [10]. Therefore, the HEDP has a low dissolution rate on AAO film compared to traditional electrolytes [15], such that a wider region of processing conditions were achieved for the rapid preparation of hard AAO films in HEDP.

Herein, we conducted the DC anodizing on aluminum in HEDP at relatively high current densities. The effect of current densities on the oxide coating prepared in HEDP was systematically investigated. The electrical signal-time response, morphology, structure, composition, and performance of the coatings were discussed in detail. The results showed that the growth rate of oxide coating had been successfully increased. Moreover, when the current density was set higher than 4 A/dm^2, the cell potential voltage increased rapidly and exceeded 400 V, resulting in a steady spark on the anode as the micro-arc oxidation (MAO) or plasma electrolytic oxidation (PEO) [20-24]. As the growth of coating, the sparks would gradually quench. Finally, a coating with outer volcanic resolidified pool structure and inner honeycomb structure was obtained, i.e. MAO/AAO composite coating. To the authors' knowledge, most of MAO coatings were prepared in alkaline electrolyte including silicate [24-27], phosphate [27-29] and

aluminate [30-32], contrasting with the acidic electrolyte used in anodizing. The present work firstly reported a micro spark phenomenon on the surface of aluminum immersed in HEDP. It is envisaged that the newly found MAO/AAO composite coating is meaningful to further explain the relationship between anodizing and MAO.

3.2 Experimental procedure

3.2.1 Sample preparation

1N30 aluminum foil (≥ 99.3 wt.% Al; ≤ 0.7 wt.% Si+Fe, Taiho Trading Co.,Ltd.) with mirror bright finish was cut into pieces with the dimensions of 25 mm × 25 mm × 0.1 mm. The samples were ultrasonically washed with acetone and deionized water at room temperature, and then dried in a cool air stream.

Fig. 2.2 gave the schematic diagram of electrolytic cell. The samples were clamped in the fixture with one side exposed, and the exposed area was limited by a silicone O-ring to 1.8 cm^2. The samples were connected the anode through a copper wire and a 304 stainless steel as cathode. The electrolytic cell was a 300mL double-walled glass beaker, and the temperature of electrolyte was maintained at 273–283 K by injecting circulating cooled water/ethanol mixture (CCA-1111, Eyela, Japan) into the interlayer of the beaker. The samples were immersed in 0.2M HEDP (pH=1.14 at room temperature) and then anodized at 1-8 A/dm^2 for 1 hour using a DC power supply (PWR1201H, Kikusui Electronics, Japan) connected to a PC. The electric signals were measured by a software (SD027-PWR-01, Kikusui Electronics, Japan). During the oxidation process, the solution was strongly stirred with a mechanical stirring bar. After the oxidation treatment, the samples were ultrasonically washed with deionized water at room temperature, and then dried in a cooled air stream for characterization. The sparks were recorded using a high speed camera (Fastcam SA1.1, Photron, Japan) with a shutter speed of 4 ms.

3.2.2 Characterization

The thicknesses of the coatings were measured with an eddy current thickness gauge

(MiniTest 735, Elektrophysik, Germany), each coating was measured at least five times. The morphologies of oxide coatings were examined in detail by field emission scanning electron microscopy (SEM) (S-4300, Hitachi, Japan). Before the SEM observation, a thin platinum layer was coated on the samples to increase the conductivity. The ImageJ 1.42q software was employed to reveal the coating structures and pore size distribution from the SEM images. At least 500 pores were measured for each sample.

The distribution of elements of oxide coating were examined by a 3D-SEM (ERA-8900, Elionix, Japan), equipped with a dispersion X-ray spectrometry (EDAX Inc., USA).

The phase compositions of oxide coatings were examined by X-ray diffractometer (X'pert Pro MPD, Malvern Panalytical, Netherlands) with Cu-Kα radiation at a scan step (2θ) of 0.01° from 25° to 80°.

Prior to hardness evaluation, the samples were cut, mounted in resin, polished through successive grades of SiC abrasive papers (320-1000#), and finely polished with diamond paste of W0.3 particle size. Then, the polished cross-sections of coatings were examined using a nanoindentation tester (DUH-211, Shimadzu, Japan) with a Berkovitch diamond indenter. The loading was gradually increased to a target load (25 mN) at a rate of 1.9 mN/s and then keep it for 10 s. The hardness H_{IT} and elastic modulus E_{IT} were determined from the load/displacement curves. At least three replicates were conducted for each sample.

3.3 Results and discussion

3.3.1 Evolution of electrical characteristics and colour

The electrical signal-time response curves during the oxidation process in HEDP at different current densities are presented in Fig. 3.1 and Fig. 3.2. As shown, when the current densities are lower than 3 A/dm^2 (Fig. 3.1), the cell potential curves present the case of galvanostatic anodizing. The potentials increase significantly first with the thickness of the growing barrier oxide and then continue to increase gradually. Such a potential evolution can be attributed to a morphological instability, i.e., transition from

the stage of barrier oxide growth to stage of porous oxide growth [33]. After that, the cell potential at 1 A/dm^2 reaches a steady value of 310 V and the corresponding current density is stable. However, the potential curves at 2 and 3 A/dm^2 reach the steady value of 324 and 342 V, respectively, after passing through an overshoot. In addition, slight electrical signal fluctuations are observed on both the potential and current density curves at 2 and 3 A/dm^2. Similar cases of electrical signal fluctuations were also observed in the literatures [8, 15, 19].

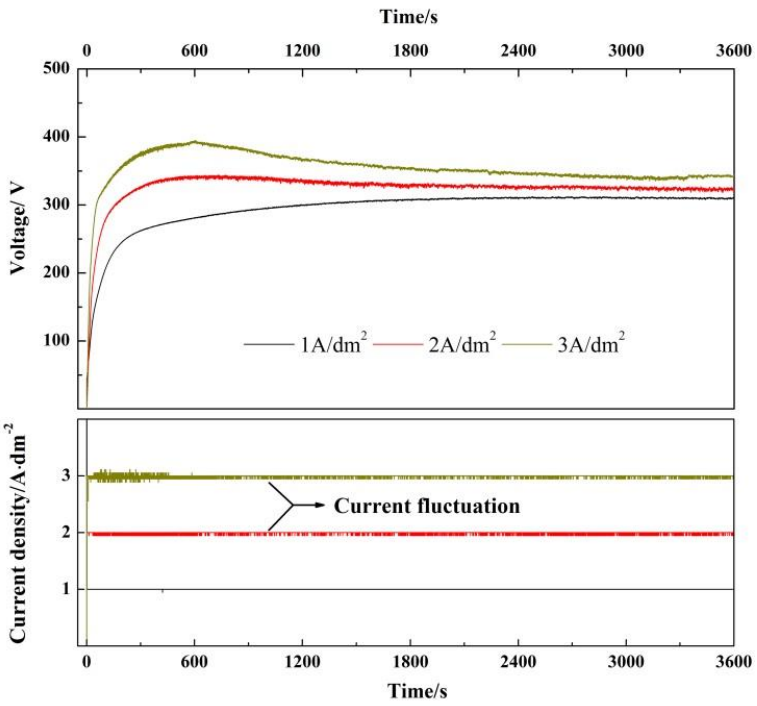

Fig. 3.1 Electrical signal-time response curves during the oxidation process in HEDP at 1–3 A/dm^2.

In fact, when the anodizing potential reaches a value (300 V in Fig. 3.1), invisible sparking on the anode starts appearing, and local thicking, cracking, blistering, or even burning of oxide film commences [10]. However, the oxidation balance has not been broken at the relatively high current densities (compared with the traditional anodizing) due to the low dissolution rate of the anodic oxide in HEDP [15].

In the case of electrical signal-time response curves at 4-7A/dm^2 (Fig. 3.2), the potentials show a similar significant rise first and then the rising trend becomes gradual

in the initial stage. However, a clear difference of the electrical signal is exhibited between the Fig. 3.1 and 3.2 in the following stage. After the transition in cell potential at 200 s, a steady sparking is observed as shown in the insert boxes of Fig. 3.2. Meanwhile, the cell potentials reach 400 V and accompany with a strong current fluctuation. Under the influence of sparks, the cell potentials continue to increase slightly. The size and intensity of sparks increase and the population density of sparks decrease with the increasing oxidation time. Note that the sparks would automatically extinguish after the oxidation treatment for about 0.5 h and the cell potentials decrease dramatically by 80 V. Meanwhile, the fluctuation amplitudes decrease and are similar to the case of 2 A/dm^2 and 3 A/dm^2 (Fig. 3.1). After that, the cell potentials do not increase and remain fluctuating within a certain range.

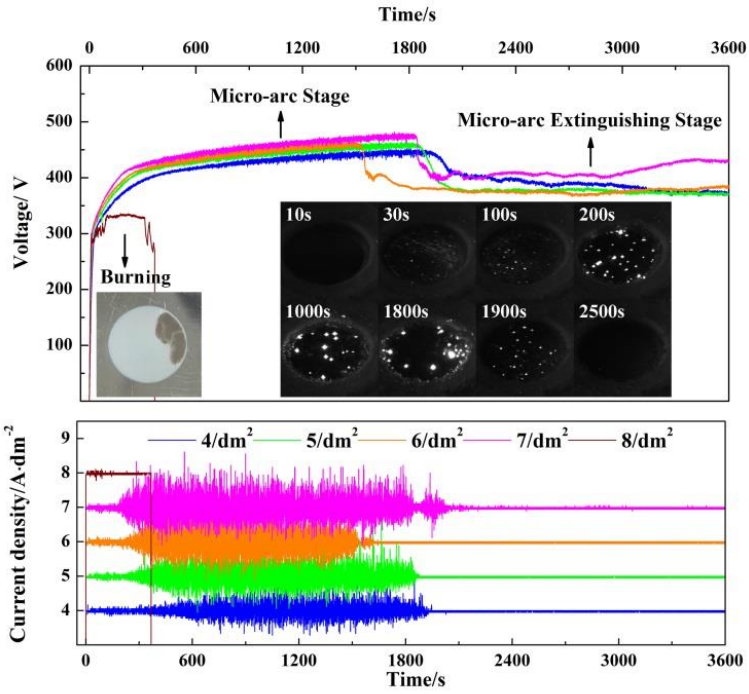

Fig. 3.2 Electrical signal-time response curves during the oxidation process in HEDP at 4–8A/dm^2. The insert boxes are the burned film (8 A/dm^2) and spark appearances during oxide process (5 A/dm^2).

In the case of 8 A/dm^2, the cell potential drops sharply after a violent fluctuating. The non-uniform oxide spots with dark brown hue were partially observed on the obtained

film, i.e. the burning phenomenon occurred, as shown in the insert box of Fig. 3.2. This burning can be interpreted as that the reaction heat cannot be adequately dissipated from the anode, and that electrolyte heating cause local increase in conductivity and a current "run away" process; thus, the dielectric properties of the oxide are permanently degraded [10].

As known, the steady visible sparking is the iconic feature of micro-arc oxidation (MAO). Thus, the whole oxidation process can be simply divided into two stages, i.e., micro-arc stage and micro-arc extinguishing stage. During the micro-arc stage, the sparks have always been blue-white which are different from the orange ones of traditional MAO process in alkaline electrolyte [32, 34]. This might indicate that the relatively lower breakdown energy or only gas breakdown occur there.

Fig. 3.3 shows the color change of coatings processed at 1–7 A/dm^2. Obviously, color ranging are from dark to light gray for current densities from 1 to 7 A/dm^2. The coatings (1–3 A/dm^2) have the same color as the AAO films prepared in HEDP by Kikuchi et al. [6] and the light grayness (4–7 A/dm^2) are generally the feature of MAO ceramic coatings [35, 36].

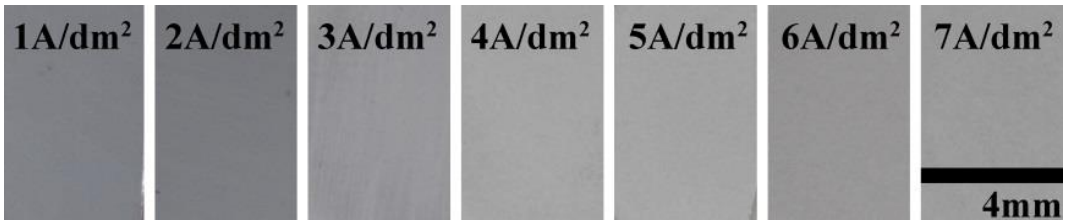

Fig. 3.3 Colors obtained from the oxide coatings formed on aluminum in 0.2M HEDP for 1 h at different current densities.

3.3.2 Surface structural characteristics

Fig. 3.4 presents the surface morphologies of AAO film prepared at 1 A/dm^2. As expected, the whole surface is smooth without defects (Fig. 3.4b), and the distorted pores with diameter of 50–250 nm (Fig. 3.4c) are clearly observed. The parallel lines on the surface are caused by the directional growth of pores induced by the original surface

finish of aluminum.

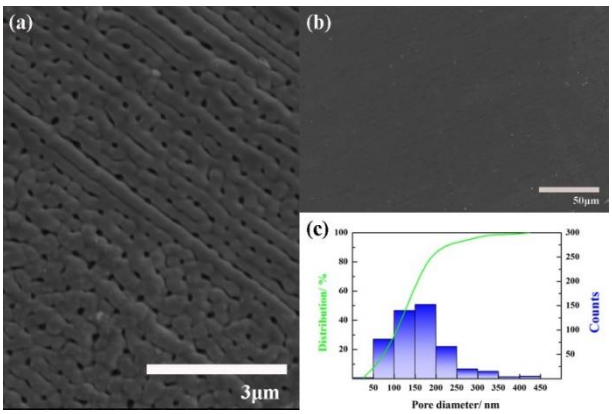

Fig. 3.4 Surface morphologies of AAO film formed on aluminum in 0.2 M HEDP for 1h at 1 A/dm^2. (a) is the higher magnification image of (b); (c) is the diameter distribution of the nano-pores.

Fig. 3.5 gives the surface morphologies of AAO film prepared at 2 A/dm^2. Compared with Fig. 3.5, there are many independent micro-pores (diameter of 1.0-3.5μm, as shown in Fig. 3.5e), or called micro-pits, with a flower-like feature. The flower-like features are possibly associated with the weak sparks on the AAO film. Those sparks are very weak and are not easy to be noticed [32], although the current fluctuation (Fig. 3.1) implies those sparks. Meanwhile, the barrier layer of AAO film was unaffected by the weak sparks, and thus the cell potential–time responses present the characteristics of anodizing. Furthermore, the number of micro-pores increases and interference occurs as the current density increases to 3 A/dm^2 (Fig. 3.6). In addition, the diameter of nano-pores becomes a little bigger due to the higher potential (Fig. 3.1).

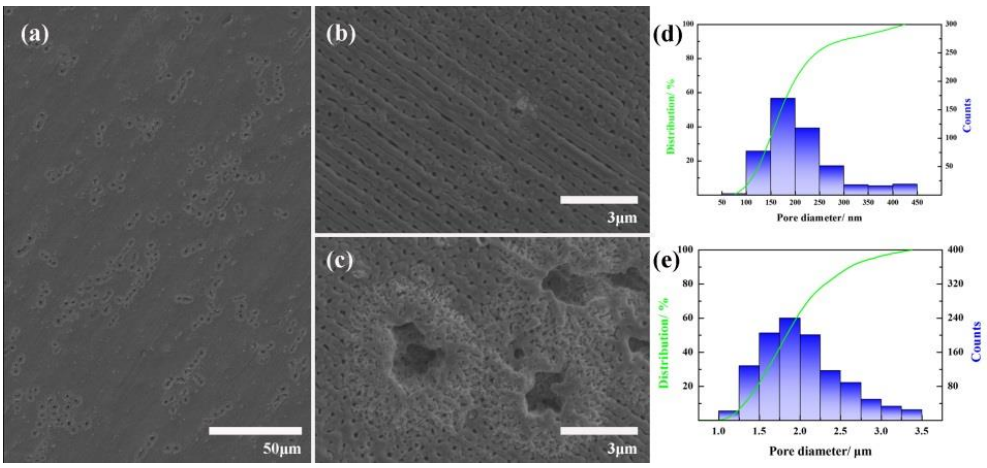

Fig. 3.5 Surface morphologies of AAO film formed on aluminum in 0.2 M HEDP for 1 h at 2 A/dm^2. (b) and (c) are the higher magnification images of different locations of (a); (d) and (e) are diameter distributions of the nano- and micro-pores, respectively.

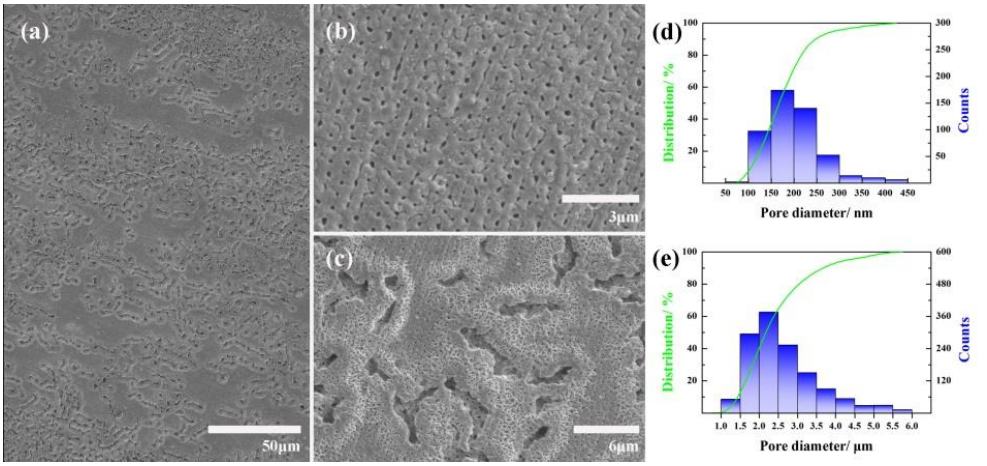

Fig. 3.6 Surface morphologies of AAO film formed on aluminum in 0.2 M HEDP for 1 h at 3 A/dm^2. (b) and (c) are the higher magnification images of different locations of (a); (d) and (e) are diameter distributions of the nano- and micro-pores, respectively.

The surface morphologies of oxide coating prepared at 4 A/dm^2 present a rough surface with two features of volcanic resolidified pools (Fig. 3.7b) and nodules (Fig. 3.7c). These features are the evidences of the "breakdown-melt-ejection-deposition" activity of oxide coating, i.e., the micro-arc oxide process [23]. The unclosed central holes of the resolidified pools is likely due to the insufficient energy of the "soft" sparks. Moreover, the nano-pores (Fig. 3.7d) that are not affected by sparks can still be observed, which is

because the density of the spark was not enough. The nano-pore area (Fig. 3.7d) would become less and discrete as the current density and process time increase.

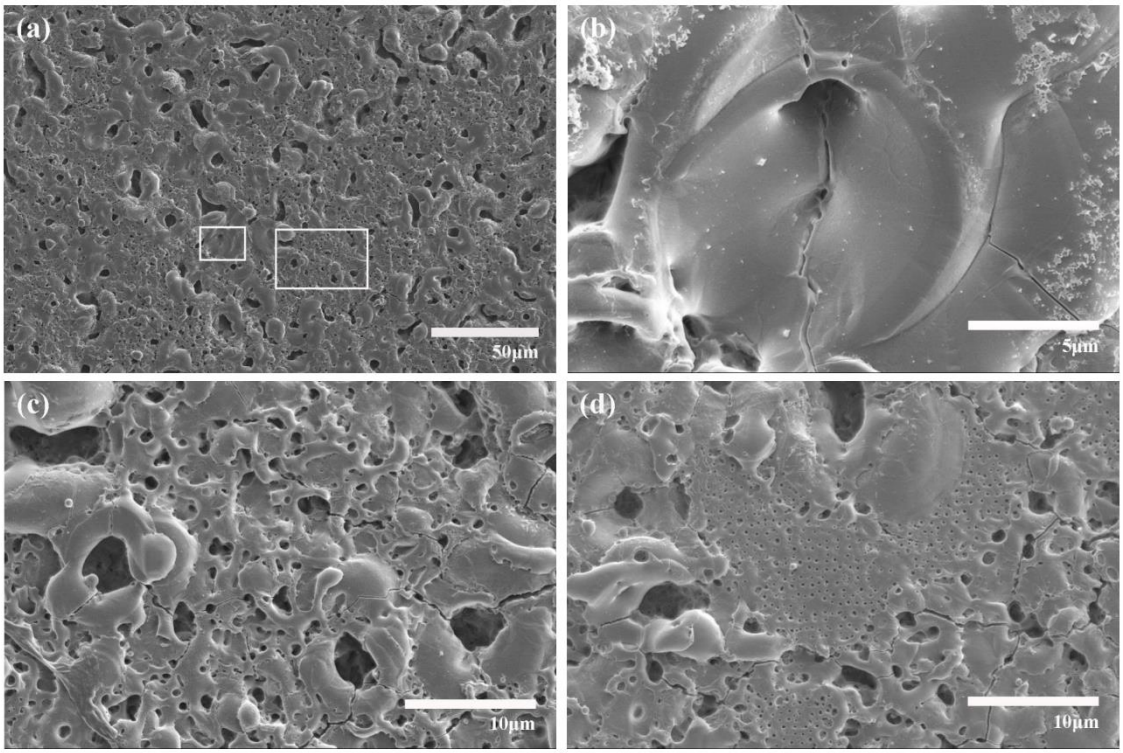

Fig. 3.7 Surface morphologies of oxide coating formed on aluminum in 0.2 M HEDP for 1 h at 4 A/dm^2. (b) and (c) are the higher magnification images of the box areas of (a); (d) is the residual nano-pore structure.

The surface morphologies of oxide coating prepared at 5–7 A/dm^2 are given in Fig. 3.8. As expected, there are few unclosed central holes of resolidified pools on the surface of oxide coating prepared at 7 A/dm^2 (Fig. 3.8c) because of the higher energy of sparks. The well developed oxide coating reveals clearly that the coating surface is only made of the resolidified pools. Unexpectedly, the size of unclosed central holes on coating prepared at 6 A/dm^2 is a little bigger than that prepared at 5 A/dm^2 (Fig. 3.8a and b). This phenomenon might be explained by the longer periods (about 300 s) of micro-arc stage of electrochemical process at 5 A/dm^2 than 6 A/dm^2 (Fig. 3.2).

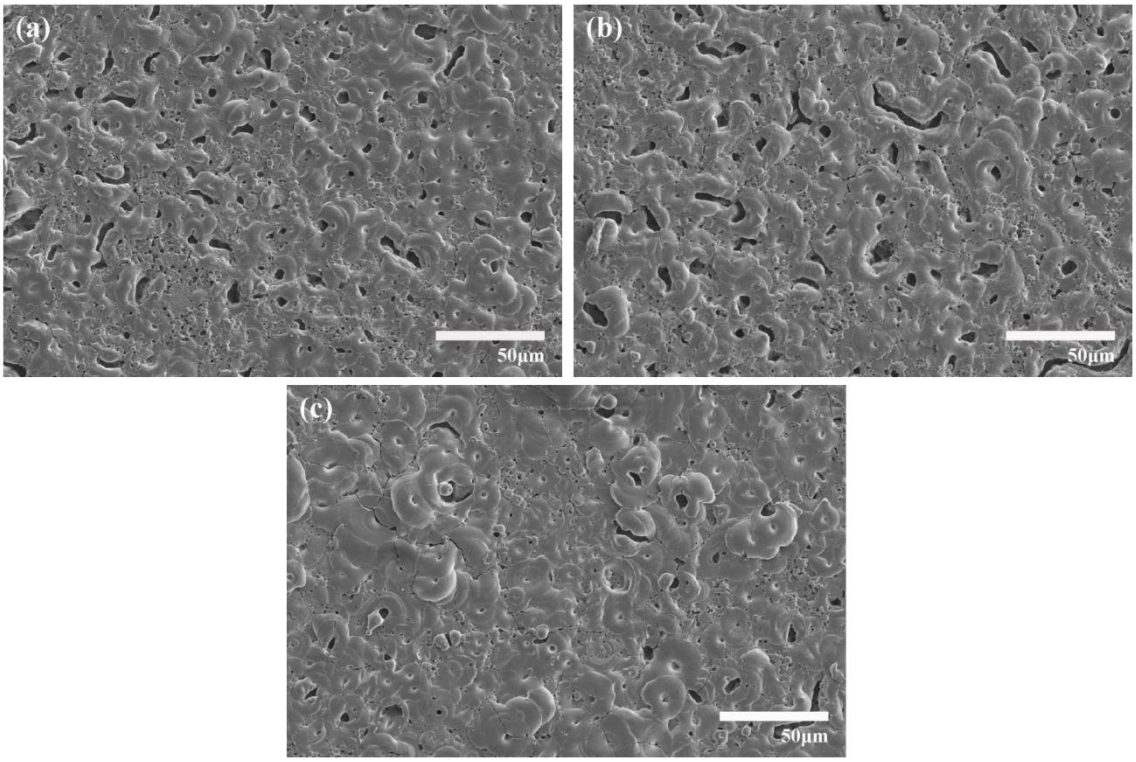

Fig. 3.8 Surface morphologies of oxide coatings formed on aluminum in 0.2 M HEDP for 1 h at different current densities. (a-c) 5–7 A/dm^2, respectively.

3.3.3 Cross-sectional structural characteristics

Fractured cross-sectional morphologies of the AAO films prepared at 1–3 A/dm^2 are shown in Fig. 3.9. Typically, the AAO films consist of outer porous layer and inner barrier layer. The thin thickness or even more thinner at the beginning (about 1 μm in Fig. 3.9a) and the relatively bigger pore diameter (about 200 nm in Fig. 3.4) of AAO film prepared in HEDP at 1 A/dm^2 guarantee the good electrical conductivity of the porous layer. Therefore, the entire potential is applied to the barrier layer (~0.97 V/nm) during the whole oxidation process. In this case, the responding cell-potential (ΔU) should be proportional to the applied current density (j) and thickness of barrier layer (t_b) according to the exponential law of Güntherschulze and Betz as follows: [10]

$$j = j_0 \exp(\beta \Delta U / t_b) \quad [3.1]$$

Which can be converted to:

$$\Delta U = t_b \log_{j_0}^{j} / \beta \quad [3.2]$$

where j_0 and β are material-dependent constants at a given temperature.

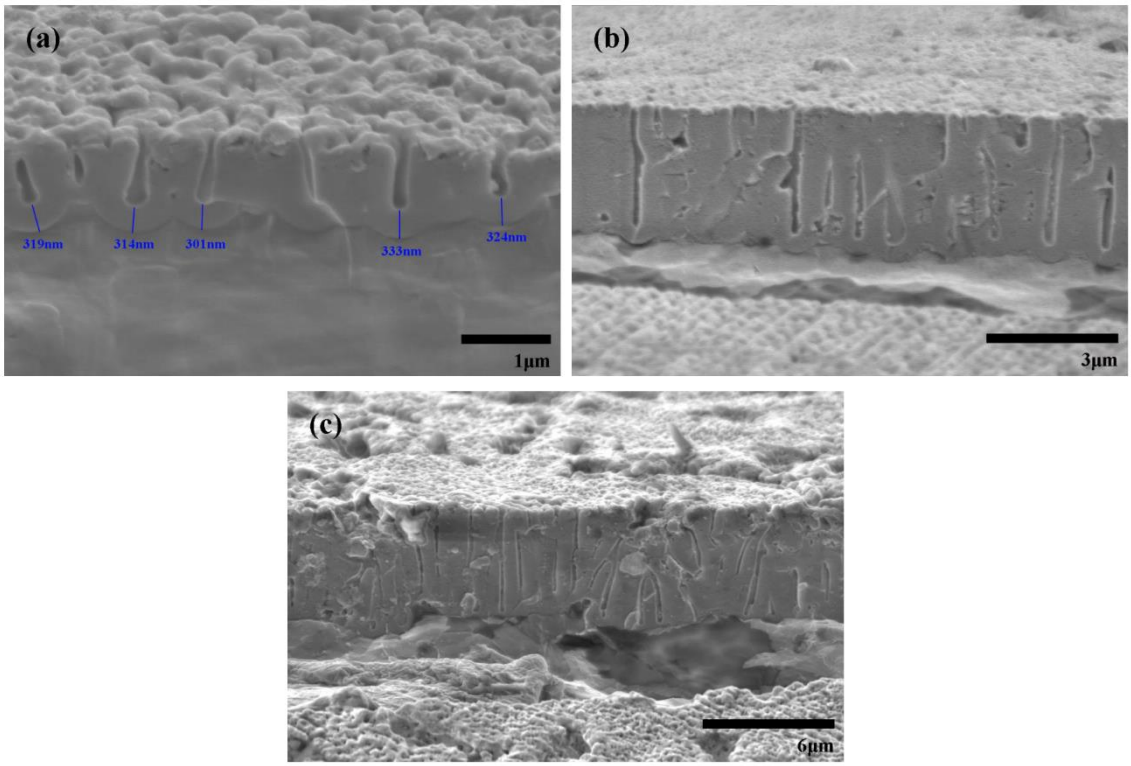

Fig. 3.9 Cross-sectional morphologies of AAO films formed on aluminum in 0.2 M HEDP for 1 h at different current densities. (a-c) 1-3 A/dm^2, respectively.

As the current density increases, the thickness of porous layer increases and the potential drop loaded on the porous layer increases. Therefore, with the evolution of AAO films, the appearance of potential overshoot (Fig. 3.1) has been related to the decrease of the initial pore density with the steady-state growth of major pores [37]: pores increase in size by persistent merging with adjacent pores. Meanwhile, the high viscous HEDP electrolyte (0.3 M HEDP for 298K, 7.584 mPa·s [19]) cannot permeate the nano-pores completely to reach the barrier layer, i.e., the channels of nano-pores would be filled with an atmospheric pressure of O_2. Ultimately, the potential drop would concentrate on the bubbles and the invisible sparks would occur once the breakdown potential of the bubbles is reached. Thus, it is understandable that the larger electrical signal fluctuation (Fig. 3.1, curve of 3 A/dm^2) at the beginning of oxidation process implies the action of invisible sparks. The top mico pores in Fig. 3.9c also proved this assumption. These mico pores

were retained on the surface of the film as the oxide film becomes thicker.

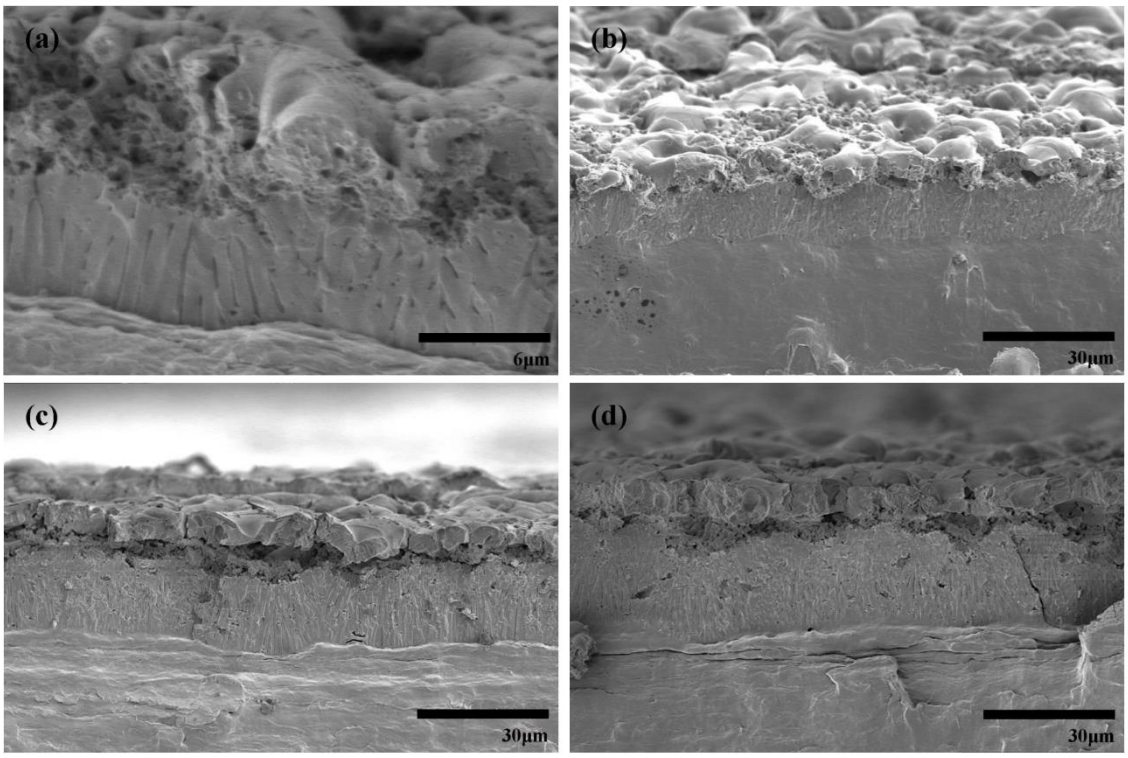

Fig. 3.10 Cross-sectional morphologies of oxide coatings formed on aluminum in 0.2 M HEDP for 1 h at different current densities. (a) 4 A/dm^2, (b) 5 A/dm^2 , (c) 6 A/dm^2, and (d) 7 A/dm^2.

Fig. 3.10 presents the cross-sectional morphologies of the coatings prepared at 4–7 A/dm^2. Interestingly, instead of generating the typical MAO coating, a composite coating with significant double layers was obtained. The top layer is considered to be the MAO layer according to its surface volcanic morphologies (Fig. 3.8), while the bottom layer is the AAO layer with honeycomb structure. The formation of MAO/AAO double layer structure should be due to the spark extinguish. Namely, the MAO layer generated in the early stage. The extinguish of micro-arc gives rise to the growth of the AAO layer. However, it is difficult to explain this stage under the galvanostatic condition. This phenomenon may suggest the conversion of coating structure and impedance drop of the whole loop, which should be further investigated to better understand the spark behavior for coating growth.

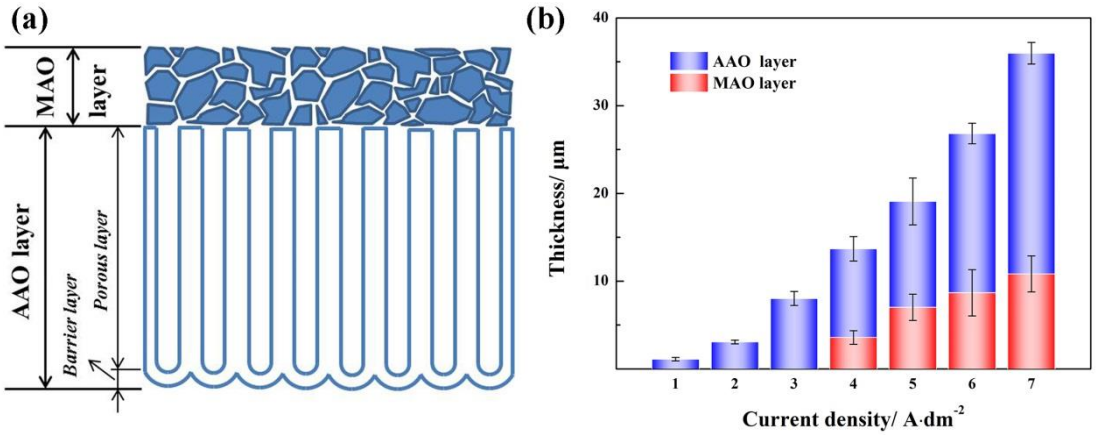

Fig. 3.11 Schematic diagram and thickness of the MAO/AAO composite coatings.

The schematic diagram of the MAO/AAO composite coating is given in Fig. 3.11a. Fig. 3.11b reveals the thicknesses of coatings prepared at different current densities. The coating thickness increases with the increasing current density. Finally, the coating consisting of 10.8 μm thick MAO layer and 25.2 μm thick AAO layer was prepared at 7 A/dm^2 for 1 h.

3.3.4 The distribution of elements

Fig. 3.12 is the EDS element mappings of the coatings prepared at 2 and 7 A/dm^2. As shown, the main elements of the coatings are Al, O, C and P. The P and C are resulted from the HEDP ($CH_3C(OH)[PO(OH)_2]_2$) used as the electrolyte, which has two P atoms and two C atoms in the molecular structure. Meanwhile, the HEDP is a tetra acid (H_4Y) with the following acid dissociation constants (pKa) [8, 15]:

$$H_4Y \leftrightharpoons 4H^+ + Y^{4-} \quad [3.3]$$

(pKa_1=1.43, pKa_2=2.70, pKa_3=7.02, pKa_4=11.20)

Which is easy to form relatively stable complexes with the with Al^{3+} ions [38]:

$$AlH_2Y^+ \leftrightharpoons AlHY^0 + H^+ \quad (\mathrm{Log}K1 = 1.8 \pm 0.3) \quad [3.4]$$

$$AlHY^0 \leftrightharpoons AlY^- + H^+ \quad (\mathrm{Log}K2 = 4.4 \pm 0.2) \quad [3.5]$$

$$AlY^- + 4H^+ \leftrightharpoons H_4Y + Al^{3+} \quad (\mathrm{Log}K3 = 22.7 \pm 0.1) \quad [3.6]$$

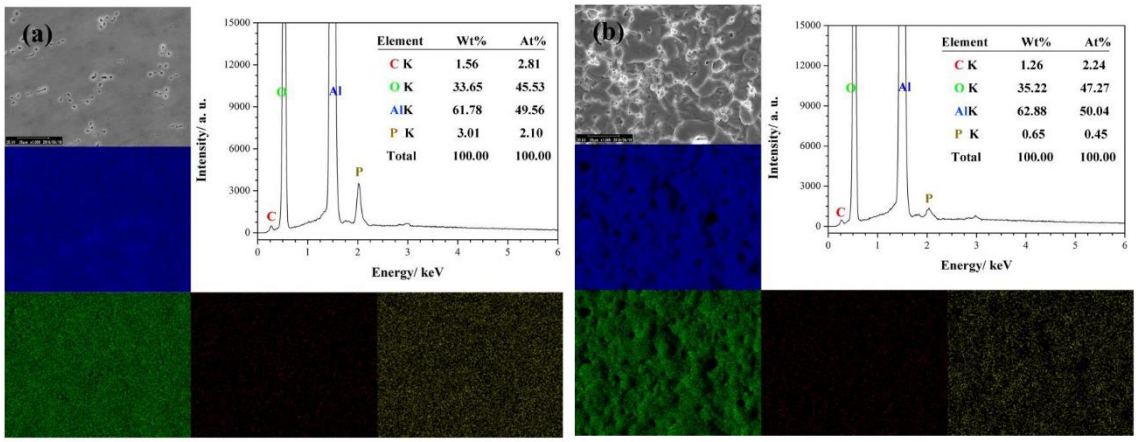

Fig. 3.12 SEM images and the corresponding EDS images of aluminum, oxygen, carbon, and phosphorus elements. (a) AAO film prepared at 2 A/dm^2; (b) MAO/AAO coating prepared at 7 A/dm^2.

The AlY^- ions is much stable due to the highest stepwise stability constants value (LogK_3=22.7). The negatively charged AlY^- ions would move to the anode in the aqueous solution under the applied electrical field. Eventually, C and P were introduced into the coatings. The relatively higher element content (at%) of C than P in Fig. 3.12a may be attributed to the contaminated sample. Nevertheless, it is considered that chemical bonds of incorporated anions with a large molecular structure are cleaved in the anodic oxide during incorporation, and this cleavage would cause the different distributions of C and P [15].

In the case of MAO/AAO composite coating (Fig. 3.12b), the contents of Al, O and C remain basically the same as Fig. 3.12a. However, only 0.45 at% P was detected. This suggests that the concentration of anion contaminants was reduced during melting of the anodic alumina under the microdischarges [36]. The EDS elements distributions in Fig. 3.13 confirm that the content of P increases rapidly at the MAO/AAO interface from surface to internal. In addition, the increases in Al and O (about 10 microns near the surface in Fig. 3.13) are thanks to the uneven edge of the fractured cross-section.

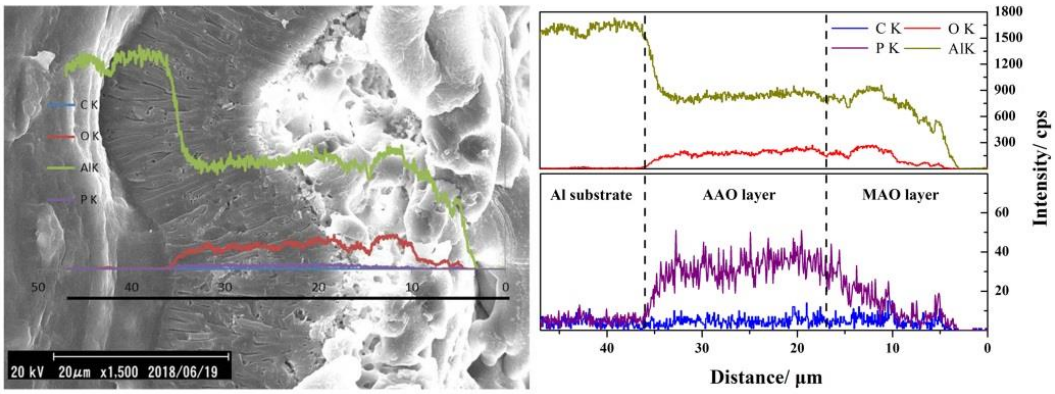

Fig. 3.13 SEM image of coating prepared on aluminum at 7 A/dm^2 and the elements distributions along the test line.

3.3.5 Coatings phase analysis

The XRD patterns of oxide coatings prepared at different current densities are presented in Fig. 3.14. It is generally recognized that the typical anodic films are amorphous, and only peaks of Al are observed for the coatings prepared at 1–2 A/dm^2. In contrast, the peaks of γ-Al_2O_3 and α-Al_2O_3 begin to appear after the current density was higher than 3 A/dm^2. Thus, the MAO/AAO composite coating keeps both outer crystallizing layer and inner amorphous layer, indicating some properties grads.

The relative contents of α-Al_2O_3 and γ-Al_2O_3 phases were estimated on the basis of the integrated intensities of the $(113)_\alpha$ and $(400)_\gamma$ peaks [24]. As shown in Fig. 3.14, the integrated intensity ratio of the two peaks (I_α/I_γ) increases as the current density increases. The similar I_α/I_γ of coatings prepared at 5 A/dm^2 and 6 A/dm^2 may be due to the difference in time of micro-arc stage (Fig. 3.2). Moreover, the absence of peaks of phases containing P and C indicates that these two elements may exist in the coatings as amorphous substance or impurity atom.

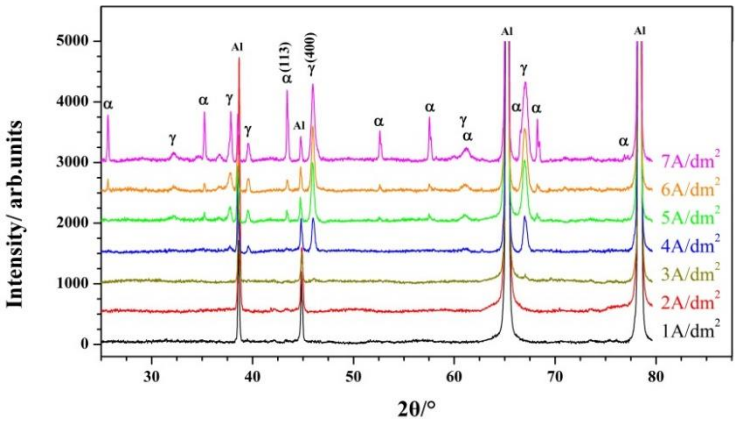

Fig. 3.14 XRD patterns for the coatings prepared in 0.2 M HEDP for 1 h on aluminum at 1–7 A/dm^2.

3.3.6 Hardness and elastic modulus of coatings

Fig. 3.15 shows the MAO/AAO composite coating prepared at 7 A/dm^2 and the locations of indents. The results of nanoindentation on MAO layer are listed in Table 3.1. The hardness of the dense area was 22.78–26.57 GPa, which is close to the value of 19–23 GPa reported for the MAO coatings prepared in concentrated aluminate electrolyte [30]. These values are thought to be a result of the high purity alumina with high content of α-Al_2O_3 (26 GPa [39]). The stiffness of the coating is related to the elastic modulus which are also given in Table 3.1. The values of elastic modulus for the coatings are approximately proportional to the hardness values.

The hardness and elastic modulus profiles from the Al/Al_2O_3 interface of AAO layer prepared at 7 A/dm^2 are given in Fig. 3.16. As shown, the hardness distribution of the interior AAO layer is relatively homogeneous. However, the hardness begins to decrease near the MAO/AAO interfaces, which indicates the loose structure as shown in Fig. 3.10d. Moreover, contrasting with the MAO layer, the lower hardness of the AAO layer was 6–8 GPa (Fig. 3.16). However, it is still much better than conventional hard anodic alumina (4–6 GPa) [5, 13] and a little higher than the hardness of hard anodic coatings (Hv= 610, i.e., 6.2 GPa) prepared in HEDP by Kikuchi et al. [6].

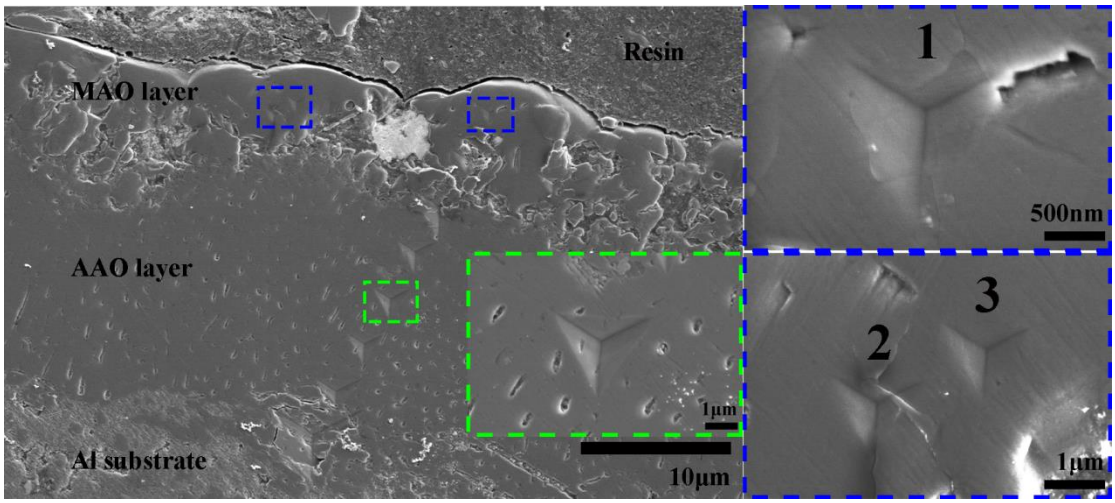

Fig. 3.15 Imprints of nanoindentation tests on the coating formed on aluminum in 0.2 M HEDP for 1 h at 7 A/dm^2 and details of the box area.

Table 3.1. Results of nanoindentation test locations in Fig. 3.15

Location	Hardness (GPa)	Elastic modulus (GPa)
1	23.64	185.0
2	22.78	187.9
3	26.57	208.2

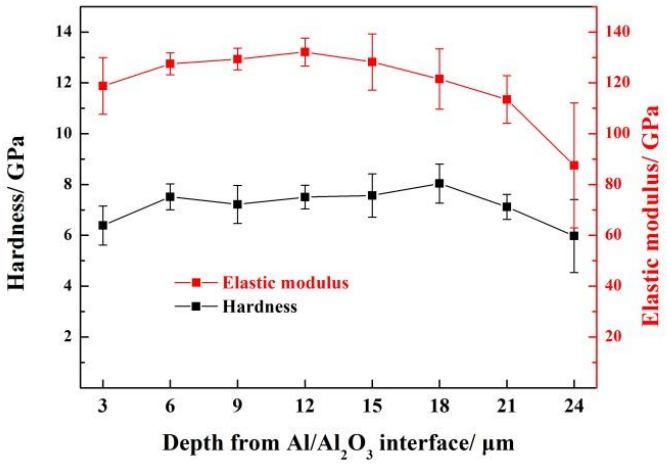

Fig. 3.16 The distribution of hardness and elastic modulus of AAO layer formed in 0.2 M HEDP for 1 h at 7 A/dm^2.

The nanoindentation tests were also performed on the center of the cross-section of AAO layers formed at 3–7 A/dm^2. The loading-unloading curves are represented in Fig. 3.17a. The indents have a good testing repeatability and show a substantial elastic recovery. Moreover, the AAO layers formed at 6 and 7 A/dm^2 keep higher stiffness. Fig.

3.17b shows the results of hardness and elastic modulus according to the loading-unloading curves. As the applied current density increases, the hardness of AAO regions increase insignificantly, while the elastic modulus increases greatly. It might be due to the difference in coating thicknes (Fig. 3.11b).

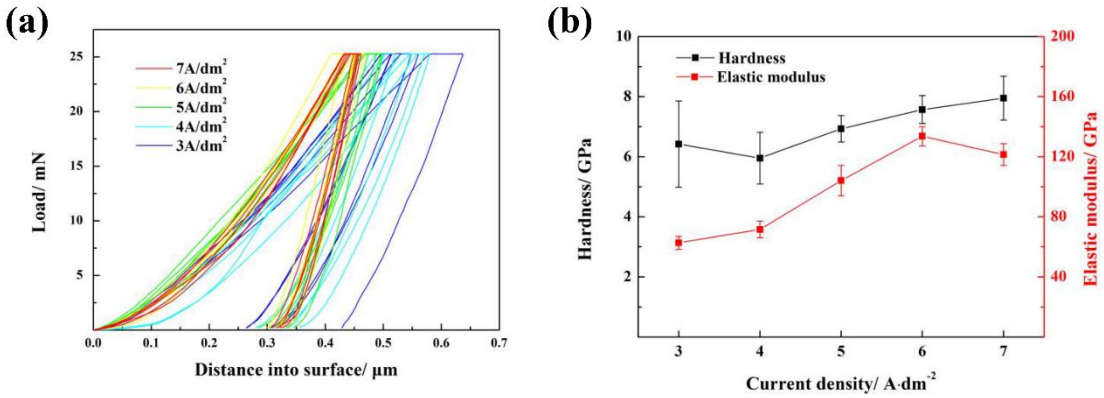

Fig. 3.17 Nanoindentation tests on AAO layers prepared at different current densities. (a) the loading-unloading curves; (b) the hardness and elastic modulus of AAO layers.

Moreover, the hardness/elastic modulus ratio (H/E) identifies the resilience of coating. Increasing in H/E ratio for coatings enhanced the elastic resilience, which might be responsible for their high mechanical and tribological performance [35]. The H/E ratio of MAO layer is 0.121-0.128 contrasting with 0.057-0.102 of AAO layer, which indicates the performance grads. Overall, the performance grads and high hardness value of MAO/AAO composite coating formed in HEDP are expected to expand the applicability of porous alumina in various severe conditions.

3.4 Conclusions

The DC anodizing on aluminum in HEDP at relatively high current densities was successfully conducted. Resulting in the obtained coatings having a MAO/AAO composite structure. The conclusions were drawn as follows:

1. The AAO films were prepared at 1–3 A/dm^2; The MAO/AAO composite coatings were prepared at 4–7 A/dm^2; The oxide coating would not be burnt down until the current

density up to 8 A/dm^2.

2. When the current density is higher than 4 A/dm^2, the whole oxidation process can be divided into two stages, namely, micro-arc stage and micro-arc extinguishing stage.

3. During the micro-arc stage, the oxide coating undergoes melting under the sparks, which changes the morphology and reduces the concentration of anion contaminants. Subsequent cooling crystallization resulted in the generation of γ-Al_2O_3 and α-Al_2O_3.

4. As the current density increases from 1 to 7 A/dm^2, the growth rate of oxide coating increases from 1 to 36 μm/h. Moreover, the relative contents of α-Al_2O_3 in MAO layer also increase.

5. The hardness of AAO layers of MAO/AAO composite coating is 6–8 GPa, and the hardness of MAO layer can reach 26.57 GPa.

References

[1] G.D. Bengough, J.M. Stuart, Improved process of protecting surfaces of aluminium or aluminium alloys, GB Patent 223994, 1923.

[2] G.D. Bengough, J.M. Stuart, A process of producing a coloured surface on aluminium or aluminium alloys, GB Patent 223995, 1923.

[3] C. Lee, K. Oh, D. Lee, Y. Kim, H. Yoon, D.-W. Park, M. Gab Kim, K. Lee, J. Choi, Self-sealing anodization approach to enhance micro-Vickers hardness and corrosion protection of a die cast Al alloy, Journal of Physics and Chemistry of Solids, 103 (2017) 87-94.

[4] Y. Wu, W. Zhao, W. Wang, L. Wang, Q. Xue, Novel anodic oxide film with self-sealing layer showing excellent corrosion resistance, Scientific Reports, 7 (2017) 1344.

[5] R. Ali, S. Pavan, V. Fridrici, P. Kapsa, Temperature effect on the kinetic alumina layer growth on 5086 aluminum substrate, Mechanika, 23 (2017) 923-930.

[6] T. Kikuchi, A. Takenaga, S. Natsui, R.O. Suzuki, Advanced hard anodic alumina coatings via etidronic acid anodizing, Surface and Coatings Technology, 326 (2017) 72-78.

[7] G. Alcalá, P. Skeldon, G.E. Thompson, A.B. Mann, H. Habazaki, K. Shimizu, Mechanical properties of amorphous anodic alumina and tantala films using nanoindentation, Nanotechnology, 13 (2002) 451-455.

[8] T. Kikuchi, O. Nishinaga, S. Natsui, R.O. Suzuki, Fabrication of self-ordered porous alumina via etidronic acid anodizing and structural color generation from submicrometer-scale dimple array, Electrochimica Acta, 156 (2015) 235-243.

[9] L. Wen, R. Xu, Y. Mi, Y. Lei, Multiple nanostructures based on anodized aluminium oxide templates, Nature Nanotechnology, 12 (2017) 244-250.

[10] W. Lee, S.-J. Park, Porous anodic aluminum oxide: Anodization and templated synthesis of functional nanostructures, Chemical Reviews, 114 (2014) 7487-7556.

[11] H. Wu, Y. Higaki, A. Takahara, Molecular self-assembly of one-dimensional polymer nanostructures in nanopores of anodic alumina oxide templates, Progress in Polymer Science, 77 (2018) 95-117.

[12] X.-w. Wei, C.-y. Chen, Influence of oxidation heat on hard anodic film of aluminum alloy, Transactions of Nonferrous Metals Society of China, 22 (2012) 2707-2712.

[13] G. Alcalá, S. Mato, P. Skeldon, G.E. Thompson, A.B. Mann, H. Habazaki, K. Shimizu, Mechanical properties of barrier-type anodic alumina films using nanoindentation, Surface and Coatings Technology, 173 (2003) 293-298.

[14] J. Luo, Young's modulus of electroplated Ni thin film for MEMS applications, Materials Letters, 58 (2004) 2306-2309.

[15] A. Takenaga, T. Kikuchi, S. Natsui, R.O. Suzuki, Exploration for the Self-ordering of Porous Alumina Fabricated via Anodizing in Etidronic Acid, Electrochimica Acta, 211 (2016) 515-523.

[16] K. Kawahara, T. Kikuchi, S. Natsui, R.O. Suzuki, Fabrication of ordered submicrometer-scale convex lens array via nanoimprint lithography using an anodized aluminum mold, Microelectronic Engineering, 185-186 (2018) 61-68.

[17] S. Ono, M. Saito, M. Ishiguro, H. Asoh, Controlling factor of self-ordering of anodic porous alumina, Journal of The Electrochemical Society, 151 (2004) B473.

[18] K. Nielsch, J. Choi, K. Schwirn, R.B. Wehrspohn, U. Gosele, Self-ordering Regimes of Porous Alumina: The 10% Porosity Rule, Nano Letters, 2 (2002) 677-680.

[19] M. Sepúlveda, J.G. Castaño, F. Echeverría, Influence of temperature and time on the fabrication of self-ordering porous alumina by anodizing in etidronic acid, Applied Surface Science, 454 (2018) 210-217.

[20] A.L. Yerokhin, X. Nie, A. Leyland, A. Matthews, S.J. Dowey, Plasma electrolysis for surface engineering, Surface and Coatings Technology, 122 (1999) 73–93.

[21] Z. Li, Y. Yuan, P. Sun, X. Jing, Ceramic coatings of LA141 alloy formed by plasma electrolytic oxidation for corrosion protection, ACS Applied Materials & Interfaces, 3 (2011) 3682-3690.

[22] X. Wu, P. Su, Z. Jiang, S. Meng, Influences of current density on tribological characteristics of ceramic coatings on ZK60 Mg alloy by plasma electrolytic oxidation, ACS Applied Materials & Interfaces, 2 (2010) 808-812.

[23] R.C. Zeng, L.Y. Cui, K. Jiang, R. Liu, B.D. Zhao, Y.F. Zheng, In vitro corrosion and cytocompatibility of a microarc oxidation coating and poly(L-lactic acid) composite coating on Mg-1Li-1Ca alloy for orthopedic implants, ACS Applied Materials & Interfaces, 8 (2016) 10014-10028.

[24] H. Huang, X. Wei, J. Yang, J. Wang, Influence of surface micro grooving pretreatment on MAO process of aluminum alloy, Applied Surface Science, 389 (2016) 1175-1181.

[25] J.A. Curran, H. Kalkancı, Y. Magurova, T.W. Clyne, Mullite-rich plasma electrolytic oxide coatings for thermal barrier applications, Surface and Coatings Technology, 201 (2007) 8683-8687.

[26] A. Polat, M. Makaraci, M. Usta, Influence of sodium silicate concentration on structural and tribological properties of microarc oxidation coatings on 2017A aluminum alloy substrate, Journal of Alloys and Compounds, 504 (2010) 519-526.

[27] Y.-l. Cheng, X.-Q. Wu, Z.-g. Xue, E. Matykina, P. Skeldon, G.E. Thompson, Microstructure, corrosion and wear performance of plasma electrolytic oxidation

coatings formed on Ti–6Al–4V alloy in silicate-hexametaphosphate electrolyte, Surface and Coatings Technology, 217 (2013) 129-139.

[28] X. Liu, L. Zhu, H. Liu, W. Li, Investigation of MAO coating growth mechanism on aluminum alloy by two-step oxidation method, Applied Surface Science, 293 (2014) 12-17.

[29] L. Yu, J. Cao, Y. Cheng, An improvement of the wear and corrosion resistances of AZ31 magnesium alloy by plasma electrolytic oxidation in a silicate–hexametaphosphate electrolyte with the suspension of SiC nanoparticles, Surface and Coatings Technology, 276 (2015) 266-278.

[30] Y.-l. Cheng, J.-h. Cao, M.-k. Mao, Z.-m. Peng, P. Skeldon, G.E. Thompson, High growth rate, wear resistant coatings on an Al–Cu–Li alloy by plasma electrolytic oxidation in concentrated aluminate electrolytes, Surface and Coatings Technology, 269 (2015) 74-82.

[31] Y.-l. Cheng, M.-k. Mao, J.-h. Cao, Z.-m. Peng, Plasma electrolytic oxidation of an Al-Cu-Li alloy in alkaline aluminate electrolytes: A competition between growth and dissolution for the initial ultra-thin films, Electrochimica Acta, 138 (2014) 417-429.

[32] Y. Cheng, T. Wang, S. Li, Y. Cheng, J. Cao, H. Xie, The effects of anion deposition and negative pulse on the behaviours of plasma electrolytic oxidation (PEO)—A systematic study of the PEO of a Zirlo alloy in aluminate electrolytes, Electrochimica Acta, 225 (2017) 47-68.

[33] Q. Van Overmeere, J. Proost, Stress-affected and stress-affecting instabilities during the growth of anodic oxide films, Electrochimica Acta, 56 (2011) 10507-10515.

[34] Y. Cheng, F. Wu, J. Dong, X. Wu, Z. Xue, E. Matykina, P. Skeldon, G.E. Thompson, Comparison of plasma electrolytic oxidation of zirconium alloy in silicate- and aluminate-based electrolytes and wear properties of the resulting coatings, Electrochimica Acta, 85 (2012) 25-32.

[35] Y.-l. Cheng, Z.-g. Xue, Q. Wang, X.-Q. Wu, E. Matykina, P. Skeldon, G.E. Thompson, New findings on properties of plasma electrolytic oxidation coatings from study of

an Al–Cu–Li alloy, Electrochimica Acta, 107 (2013) 358-378.

[36] E. Matykina, R. Arrabal, P. Skeldon, G.E. Thompson, P. Belenguer, AC PEO of aluminium with porous alumina precursor films, Surface and Coatings Technology, 205 (2010) 1668-1678.

[37] F. Li, L. Zhang, R.M. Metzger, On the Growth of Highly Ordered Pores in Anodized Aluminum Oxide, Chemistry of Materials, 10 (1998) 2470–2480.

[38] S. Lacour, V. Deluchat, J.-C. Bollinger, S. Bernard, Complexation of trivalent cations (Al(III), Cr(III), Fe(III)) with two phosphonic acids in the pH range of fresh waters, Talanta, 46 (1998) 999-1009.

[39] R.H.U. Khan, A. Yerokhin, X. Li, H. Dong, A. Matthews, Surface characterisation of DC plasma electrolytic oxidation treated 6082 aluminium alloy: Effect of current density and electrolyte concentration, Surface and Coatings Technology, 205 (2010) 1679-1688.

Chapter 4 Morphological evolution and burning behavior of MAO/AAO coating

4.1 Introduction

Anodizing is an electrolytic passivation process used to increase the thickness of the natural oxide layer on the surface of metals. The porous anodic aluminum oxide (AAO) formed on aluminum has been widely applied to increase surface corrosion resistance [1] or mechanical performance [2, 3], meet decorative requirements, prepare nano-template [4, 5], etc. Micro-arc oxidation (MAO) [6], also called anodic spark oxidation (ASO) [7] or plasma electrolyte oxidation (PEO) [8], is a combination of electrochemical and physical discharge processes, which has attracted more and more attention due to the excellent performance of MAO coating. The benefits of MAO coating include strong abrasion resistance, corrosion resistance, hardness, thermal shock resistance and biocompatibility, etc [7, 9-11].

The difference between MAO coating and anodic film are structure and crystalline state [12, 13]. The ceramic MAO coatings consist of an outer loose layer, inner compact layer and an extremely thin amorphous alumina layer (AAL) [14], while the amorphous anodic film is composed of an outer honeycomb layer and inner barrier layer [5]. These features are closely related to their different electrochemical regimes [5, 8].

For the case of anodizing, a lower current/ voltage at direct-current (DC) mode [15, 16] is generally chosen to avoid the burning of film [17, 18]. Meanwhile, the acid electrolytes (e.g. chromic acid [19], sulfuric acid [20, 21], oxalic acid [22] and phosphoric acid [23]) are used to prepare the AAO with different interpore distances according to the different electrochemical windows. The field-assisted dissolution [5, 24, 25] theory could explain the development of the major pores encountered in the AAO. Regarding to anodizing, the MAO process also requires immersion of the components in electrolyte, and uses electrical current to grow a thick coating on metal surface. However, most of MAO

coatings are generally prepared in alkaline electrolytes, e.g. silicate [6], phosphate [26] and aluminate [27], etc. The much higher electrical parameters are selected at alternating-current (AC) or high-frequency pulsed direct-current (PDC) modes [28-31] to arouse the surface sparks or plasma discharges. These sparks would result in high temperature conversion of the growing coating into crystalline phases, e.g. α- and γ-alumina [6]. Although many discharge models have been proposed, such as ion current mechanism, electron avalanche mechanism, thermal mechanism and mechanical mechanism [14, 32, 33], the complicated growth mechanism of MAO coating is still not unified. It is generally considered that migration of ion and deposition of components from electrolyte are the two driving forces for MAO coating growth [8, 9].

Recently, Shen et al. [34, 35] found that the coating/substrate interface layer of MAO coating consists of inter-connected tiny globular particles, which was interpreted by the re-passivation of newly exposed substrate caused by discharge. They considered that the inward growth of coating was attributed to plasma discharges. Afterward, Zhu et al. [14, 36] proposed that the main MAO voltage drop of applying the sample loaded on AAL layer (~1 V/nm), concluding that the MAO was not an abrupt ejection of a molten material but a gentle growth process. Actually, the similar "anodizing ratio" [5] was used to explain the growth kinetics of AAO film. They strongly imply the relationship between the growth mechanisms of MAO coating and AAO film. Moreover, the newly prepared coating with MAO/AAO double layers [37] via etidronic acid ($CH_3C(OH)[PO(OH)_2]_2$, HEDP) anodizing seems to be meaningful for interpreting the relationship.

This paper first investigated the burning of anodic film prepared in HEDP at 8 A/dm^2, which proved that the burning was caused by the stress-induce-cracking of initial film instead of sparks. Then, the DC oxidation was conducted just below burning current density, and results indicated that the resultant coating consisted of outer MAO layer and inner AAO layer. The morphological evolution of the coating was investigated in detail by SEM and the growth curve was recorded. Finally, the growth behavior of coating processed in HEDP at high current density was proposed and discussed.

4.2 Experimental procedure

4.2.1 Sample preparation

Pure aluminum (1N30, ≥99.3 wt% Al, Ra ≈ 0.026 μm), in the form of rolled foil (0.1mm), was cut and put into a holder with a round window of 1.8 cm^2. The configuration of the experimental setup is the same as described in a previous paper [37]. The electrolyte was 0.2 M HEDP (For 25 ºC the conductivity was 30.74 mS/cm and the pH=1.14), which was maintained at 273–283 K by circulating cooled water and strongly stirred by a mechanical stirring bar (350 rpm). During the oxidation treatment, the constant current (CC) mode was selected, and the electric signal was measured and recorded by data acquisition module. The plasma discharge during the oxidation process was monitored using a high speed camera (Fastcam SA1.1, Photron, Japan) with a shutter speed of 4 ms. After the oxidation treatment, the samples were ultrasonically washed with deionized water at room temperature, and then dried in a cooled air stream for characterization.

4.2.2 Characterization

The surface and cross-sectional morphologies were observed by the field emission scanning electron microscopies (FE-SEM) (S-4300 and SU-70, Hitachi, Japan). Meanwhile, the element compositions and distributions of coatings were measured by an energy dispersive spectrometer (EDS) coupled to the SEM (SU-70). For cross-sectional observation, the fresh broken section was obtained by breaking the sample. For testing, all samples were coated with platinum to increase the conductivity.

The phase compositions of coatings were examined by X-ray diffractometer (X'pert Pro MPD, Malvern Panalytical, Netherlands) with Cu-Kα radiation at a scan step (2θ) of 0.01° from 25° to 80°.

The roughness of oxide coating was tested by a surface measuring machine (Form Talysurf Intra, Taylor Hobson, U. K.) with a testing length of 8 mm. The thickness of the coatings was measured by an eddy current thickness gauge (MiniTest 735, Elektrophysik,

Germany). The thickness of the samples before and after oxidation was measured by a spherical face digimatic micrometer (395-271-30, Mitutoyo, USA). Each value was measured at least seven times. Moreover, the thickness of coating sub-layers was measured from the cross-sectional SEM images via image analysis software (Image J 1.42q).

4.3 Results and discussion

4.3.1 Maximum current density and burning behavior of anodic film

Fig. 4.1 shows the voltage-time response at different current densities. It is seen that the voltages rise rapidly in a short time and then slow down, which is due to the formation of the passive barrier layer. The stable oxidation process can be maintained when the current density is low than 7 A/dm^2. In contrast, the electrical instability occurs when the voltage reached 300 V at 8 A/dm^2.

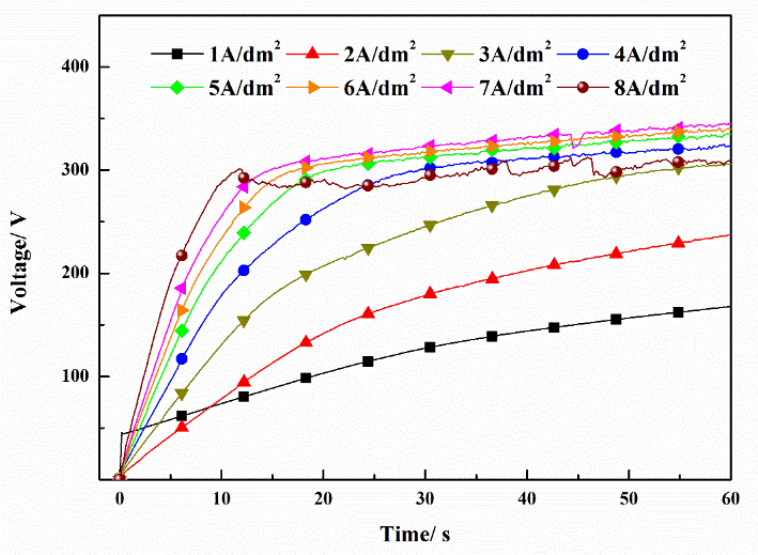

Fig. 4.1 Initial voltage response at different current densities.

The real-time imaging of oxide process (Fig. 4.2) indicates that the electrical instability is attributed to the burning of film. The weak sparks are uniformly distributed on the anode surface at first (Fig. 4.2A1), and then they concentrate on a local area, it eventually results in the strong burning of oxide film (Fig. 4.2A2). Afterward, the sparks randomly

spread on the anode, generating that the burnt area exhibits a dark brown hue contrasted with the light green of burnt-free area.

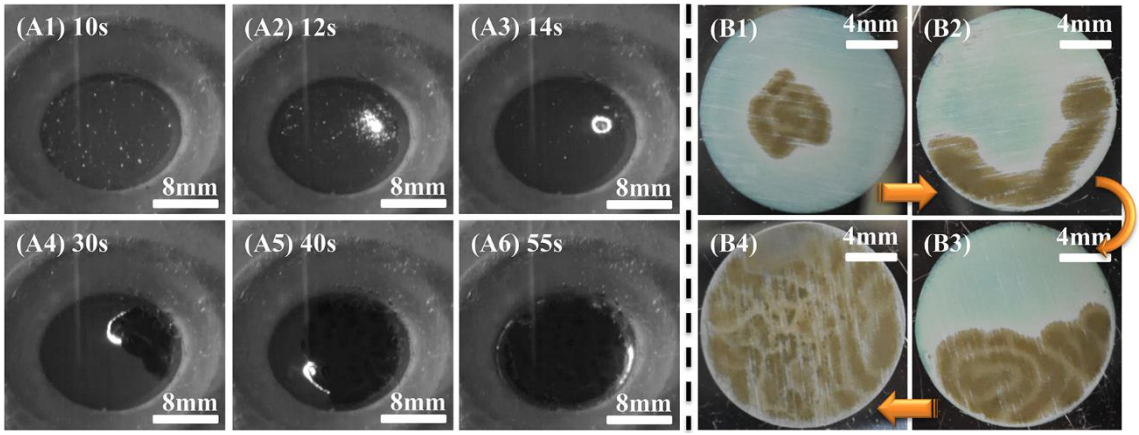

Fig. 4.2 Burning behavior of anodic film prepared at 8 A/dm^2 . (A1-A6) are real-time images of a single sample; (B1-B4) are burnt samples with different burning time.

4.3.2 Morphologies and element distributions of the burnt area

The surface morphologies of burnt and burnt-free areas are presented in Fig. 4.3. The burnt area with obvious bulging structures and even cracks can be observed (Fig. 4.3A). It is generally believed that oxidation of aluminum is a volume expansion process, and the volume expansion during anodizing can be expressed by Pilling-Bedworth ratio (PBR) [38], as follows:

$$\mathrm{PBR} = \frac{V_{ox}}{V_m} \qquad [4.1]$$

Where V_{ox} and V_m are the volume of grown oxide and consumed metal, respectively. It is proposed that the oxide film is easily crumbled due to the too much compressive stress when the PBR > 2 [5]. The higher magnification image of burnt area (Fig. 4.3B) shows that the porous-type oxide is formed again on the new-exposed aluminum inside the crack, and the surface cracks provide the local paths for electrolyte. Once the bulging structure appears, the current “run away” would occur. Then the bulging structure would start to spread until all the fresh anode surface is burnt (Fig. 4.2B4).

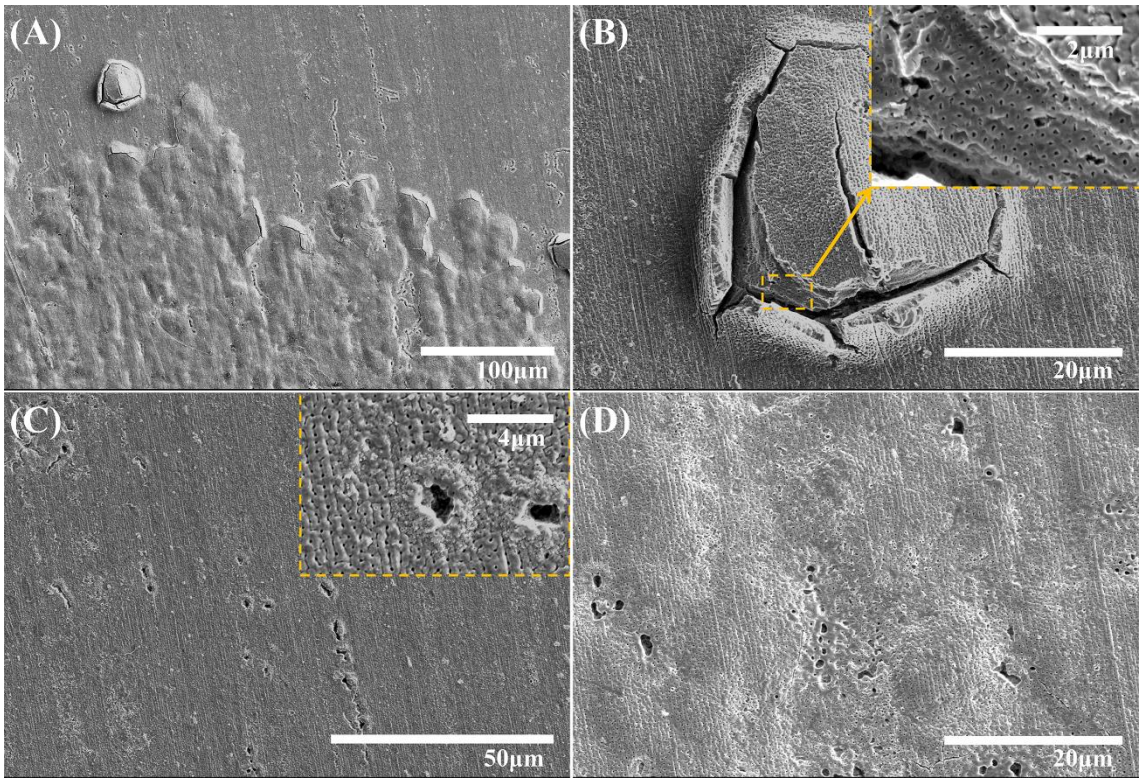

Fig. 4.3 Surface morphologies of the anodic film formed at 8 A/dm^2 . (A) and (B) are the boundary of the burnt area; (C) and (D) are the burnt-free and burnt areas, respectively

Excepting for the burning caused by high stress, other burning phenomenon was not observed, e.g. accelerated corrosion of anodic film caused by oxidation heat accumulation at high current density [39]. Although there are visible sparks on the anode surface (Fig. 4.2A1), it does not interrupt the oxidation balance and only some micro pits are bombed out on the anode surface (Fig. 3C and D).

The EDS results of burnt area (Fig. 4.4) show that the Al content decreases from 49.56 to 26.43 at% after the film is suffered from burning; however, the contents of other elements (O, P and C) increase. It can be explained by more incorporation of acid-anion as a result of the local high current density (sparking area). Furthermore, it was proposed that the amount of incorporated acid-anion would increase the volume expansion of film [40, 41].

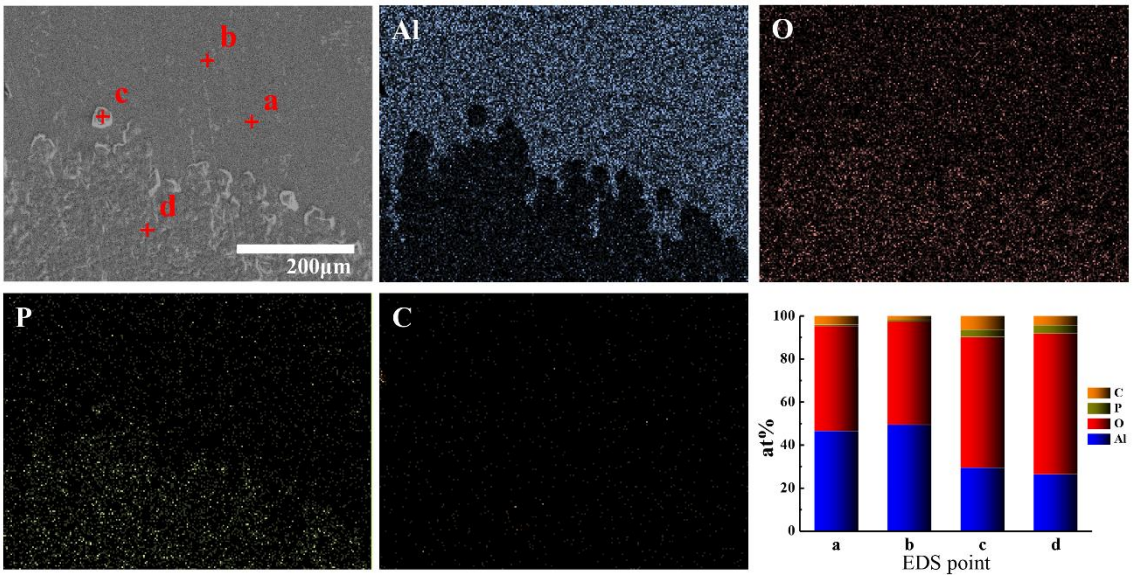

Fig. 4.4 EDS results of the burnt area.

4.3.3 Stable plasma discharge behavior

To investigate the film growth with stable sparks, the anodizing was conducted at the current density of 6 A/dm^2. Fig. 4.5A shows the V-t response curves of samples (1-5#) for different oxide time, indicative of good repeatability. Fig. 4.5B gives the whole changes in electrical signal-time response curves. It was seen that the oxidation process can be divided into four typical stages. The voltage first increases linearly to 306 V at a rate of 18 V/s (stage I, 0~17 s). Then, a sudden reduction in slope is seen when the voltage increases linearly to 411 V at a rate of 0.54 V/s (stage II, 17~213 s). In this stage, a slight electrical signal fluctuation begins to appear; simultaneously, some weak and soft sparks are visible on the electrode (Fig. 4.6A). For stage III (213 s~60 min), the voltage gradually increases to 474~510 V with a strong electrical signal fluctuation, while the rising rate of voltage further reduces to 0.026 V/s. As shown in Fig. 4.6B-D, the discharges become more and more intensive by accompanying with a bursting sound, indicating the appearance of micro-arcs [42]. These stable micro-arcs are generally considered as the typical feature of MAO, which creates a high temperature and pressure environment for the reaction of various reactive species [43]. In the later period of stage III, the intensity of micro-arcs gradually decreases (Fig. 4.7), the soft sparks become dominant again, and

then they eventually disappear. Finally, the electrical signals stop strongly fluctuating and the voltage gradually decreases to ~410 V (stage IV). As shown in Fig. 4.7, a micro-arc continues to appear somewhere for more than 0.6 s (Fig. 4.7) when compared to the short duration (0.25–3.5 ms [33]) of that in normal MAO, which indicates the relative weak area here and insufficient breakdown energy.

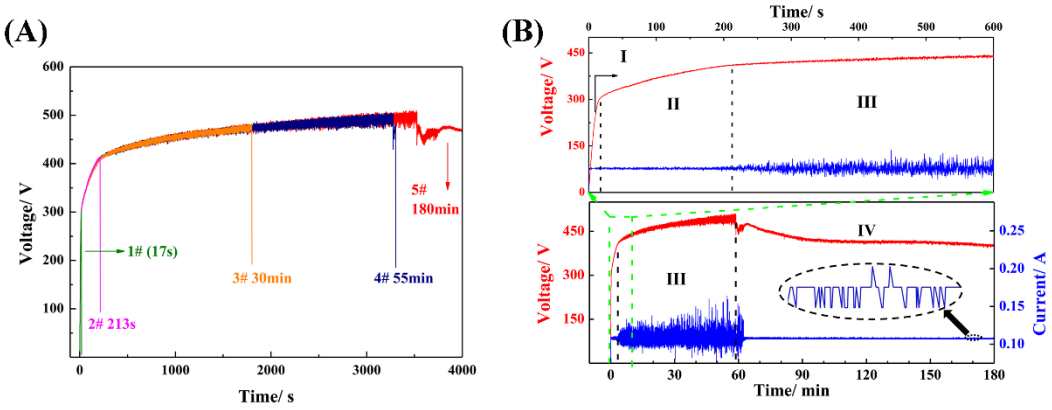

Fig. 4.5 Electrical signal-time response curves during the oxidation process in HEDP at 6 A/dm^2. (A) repeated experiments at different termination time; (B) the complete response curve of sample 5#.

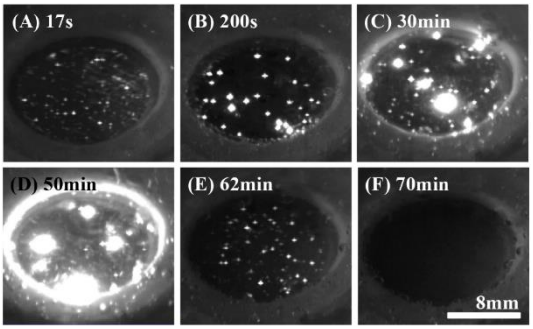

Fig. 4.6. Discharge behaviour on sample 5# immersed in HEDP at 6 A/dm^2

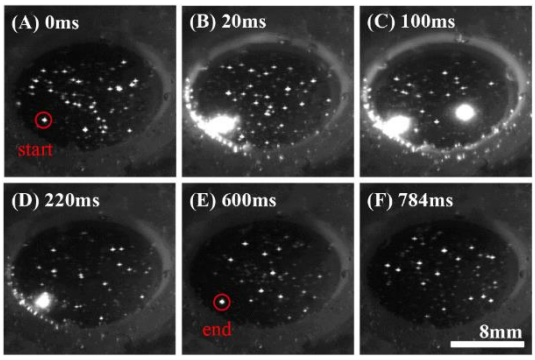

Fig. 4.7. Discharge behaviour on sample 5# at a moment during the end of stage III.

4.3.4 Surface roughness and compositions of coatings

The surface roughness and appearance of resultant coatings (1-5#) are presented in Fig. 4.8A and B. The untreated aluminum with mirror bright finish first turn light green and

then turn gray, which indicates the increase in coating thickness and the crystal transition. The surface roughness of coating keeps increasing under the influence of plasma discharge. After 55 min oxide treatment, the roughness reached the maximum, i.e. Ra=2.9 μm, and the later stage IV did not change the surface roughness.

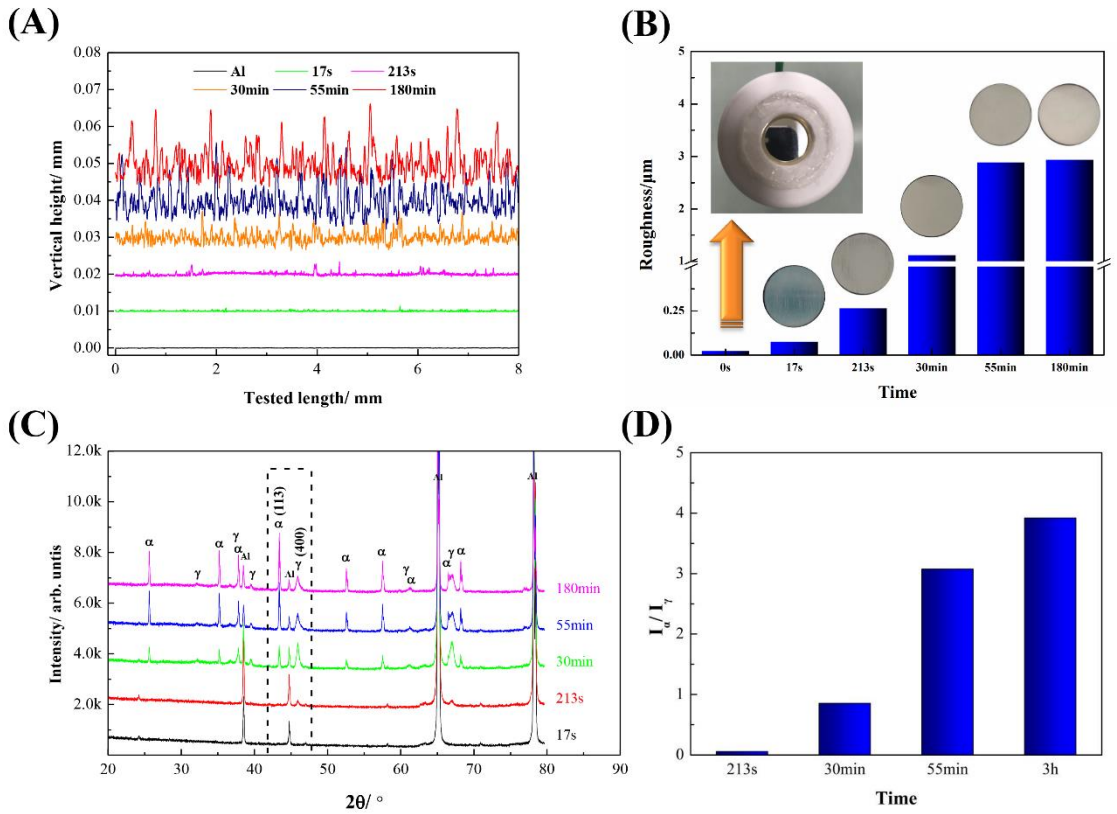

Fig. 4.8 (A) and (B) are surface roughnesses and color evolutions of oxide coatings; (C) and (D) are XRD results and the relative content of α-Al_2O_3 to γ-Al_2O_3.

The XRD patterns of oxide coatings prepared at different time are presented in Fig. 4.8C. The crystalline phases gradually appear due to the plasma-modification by sparks. The γ-Al_2O_3 first appears after 213 s treatment. The relative content of α-Al_2O_3 to γ-Al_2O_3 (I_α/I_γ, Fig. 4.8D) reached ~3 after the sparks extinguish, which indicates a high hardness value [6, 37]. Moreover, the I_α/I_γ of 3 h is a little bigger than that of 55 min, which should be attributed to different sparking time of samples 4# and 5# (Fig. 4.5).

4.3.5 Morphology evolution of coating formed at 6 A/dm^2

As given in Fig. 4.9, the surface and cross-sectional morphologies of the anodic film

formed for 17 s present two distinct features (Fig. 4.9B and C). Initially, the barrier layer with embryo pores rapidly form on aluminum (Fig. 4.9B). When the voltage reaches 300 V, many micro pits or even grooves (Fig. 4.9A and C) appear randomly on the surface of barrier layer. In agreement with Fig. 4.3C and D, the micro pits are attributed to the bombardment of soft sparks. Notably, the barrier layer would not be brokendown by sparks, instead, the grooves with a depth of ~1 μm are formed here (the insert figure in Fig. 4.9C).

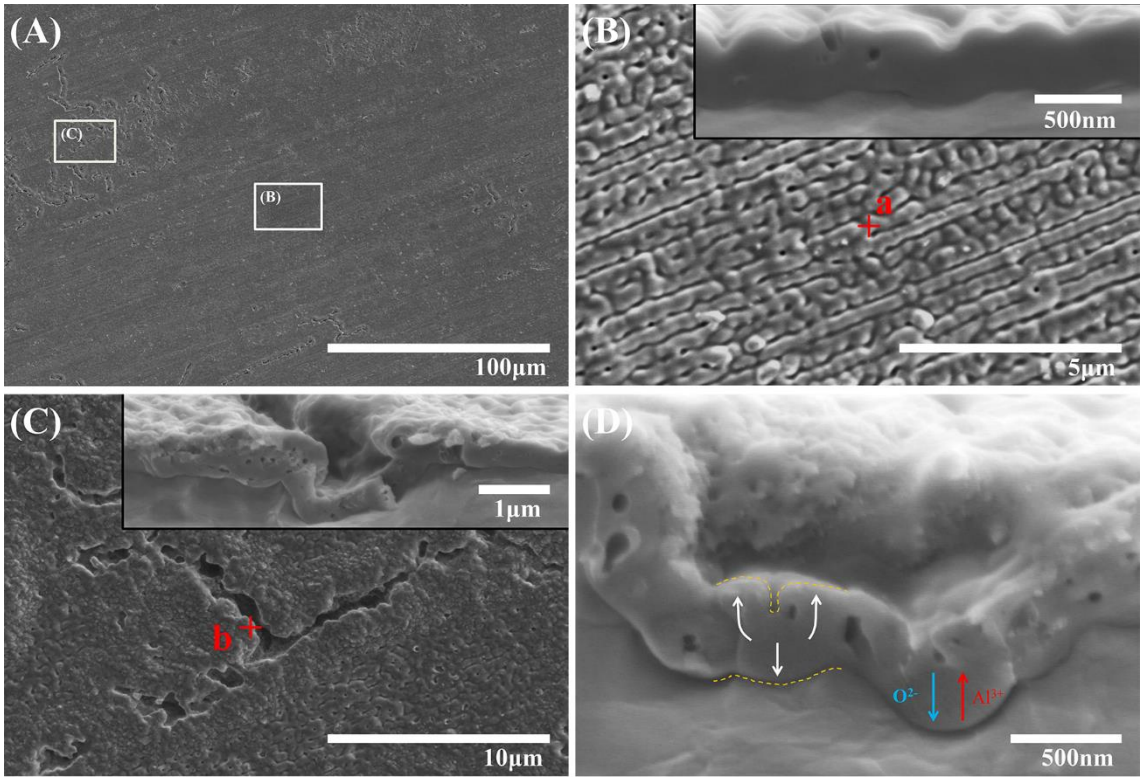

Fig. 4.9 Surface and cross-sectional morphologies of sample 1#. (B) and (C) are the higher magnification images of the box areas of (A); (D) is a cross-sectional morphology of micro pits; a and b are the EDS tested locations.

According to the existing plasma discharged models for MAO [33, 44], there are four types of discharge that can occur, i.e. the gas discharge near the anode surface (type A), the dielectric breakdown of coating (type B), the gas discharge deep in pores of coating (type C), and the internal discharges occurring in large pores near the interface between the inner and outer layers (type D). Undoubtedly, these soft sparks should be the type A

discharge at the barrier layer/electrolyte interface. This causes the thinning or even removal of barrier layer, generating the micro pits. Afterward, the current would focus on the micro pits due to the impedance reduction. The passive barrier layer would rapidly form at the bottom of micro pits again (Fig. 4.9D), simultaneously accompanying with more micro pores because of the induction of defects and stress (Fig. 4.9D). In addition, the micro pores would further motivate the discharges (type C). Thus, the continuously moving sparks cause the micro grooves (Fig. 4.9C). EDS results (Table 4.1) show that more O, P and C can be found around the plasma-modified (PM) area, indicating a generation of carbon-phosphorus compound caused by plasma heating.

Table 4.1 EDS analyses on the surface of sample 1#. (the points in Fig. 4.9)

Point	Element composition (at%)			
	O	Al	P	C
a	47.96	49.45	0.77	1.83
b	60.73	31.63	1.99	5.66

As the oxidation progress, the coating (which should not be called as film in the later stages) continues to thicken and the PM area gradually cover the whole aluminum surface with a short duration (Fig. 4.10), resulting in increases in voltage (Fig. 4.5) and intensity of sparks (Fig. 4.6B). Three features can be observed on coating formed for 213 s treatment, i.e. the bud of volcano-like structure, the nodular PM area, and the residual anodic film. The generation of volcano-like structure implies the melting of coating materials caused by dielectric breakdown. In addition, the evolution of embryo pores into honeycomb (residual anodic film, Fig. 4.10C) indicates that the field-assisted dissolution theory promotes the growth of oxide coating during stage II.

EDS analyses have been made on these features as listed in Table 4.2. The concentrations of P and C of volcano-like structure (study point a in Fig. 4.10B) were lower than that of PM area (study area b in Fig. 4.10B). E. Matykina, et al [43] have proved that the melting process of anodic alumina would reduce the concentration of anion contaminants. The pyrolysis of compounds containing P and C can be used to interpret the results.

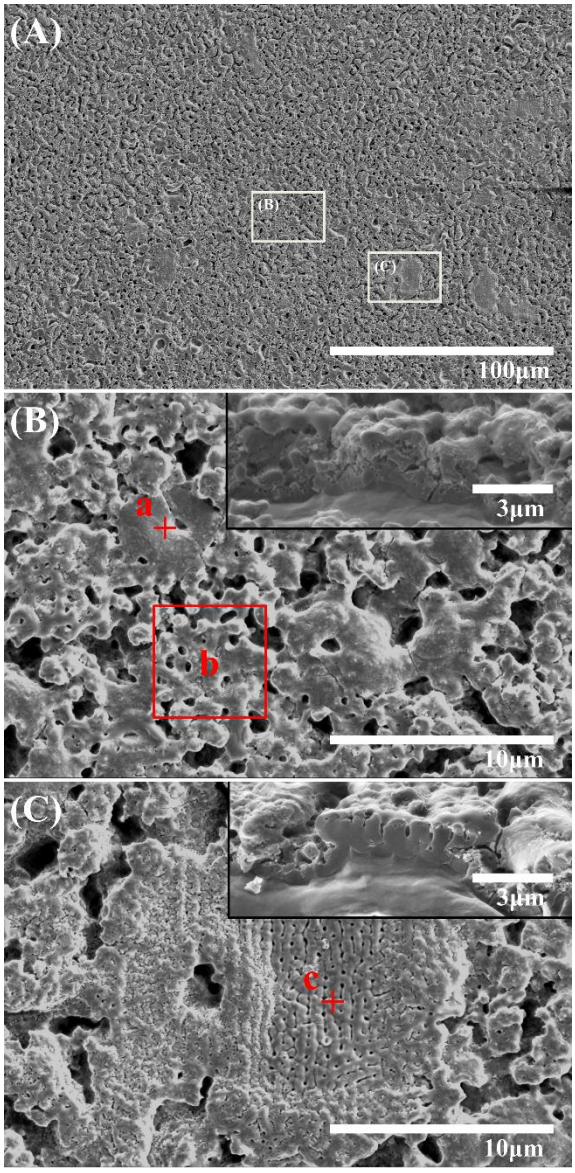

Fig. 4.10 Surface and cross-sectional morphologies of sample 2#. (B) and (C) are the higher magnification images of the box areas of (A); a, b and c are the EDS tested locations.

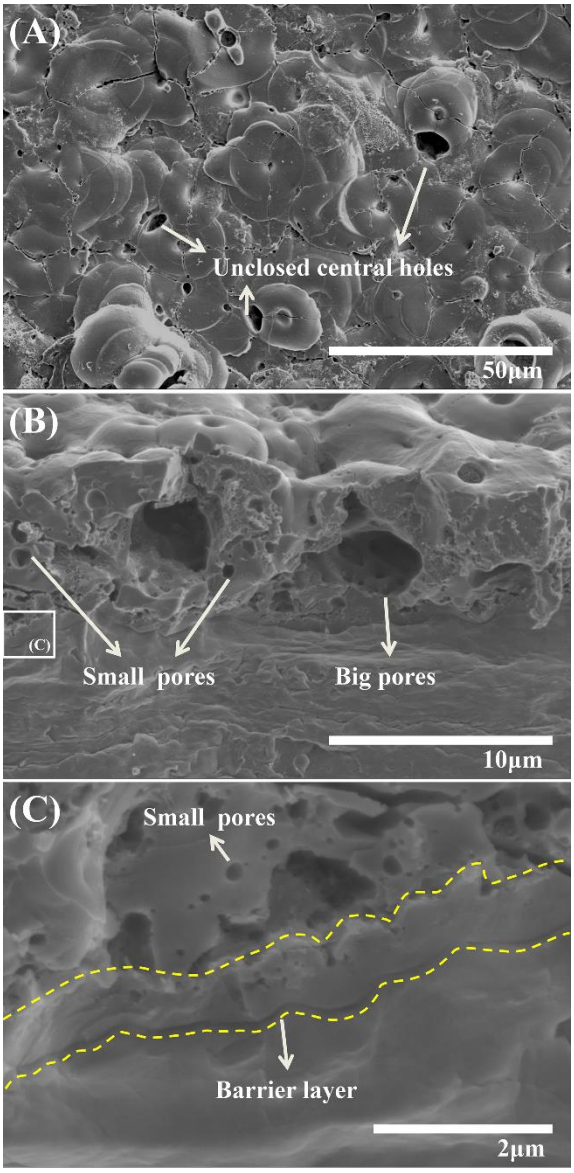

Fig. 4.11 Surface and cross-sectional morphologies of sample 3#. (A) surface image; (B) cross-sectional image; (C) is the higher magnification image of the box areas of (B)

Table 4.2 EDS analyses on the surface of sample 2#. (the locations in Fig. 4.10)

Location	Element composition (at%)			
	O	Al	P	C
a	56.89	41.35	0.99	0.78
b	62.92	32.74	2.31	2.03
c	50.01	47.50	0.66	1.82

The coating formed for 30 min oxide treatment is presented in Fig. 4.11. Its surface is only featured by volcano-like structure, i.e., the MAO coating is generated, and no anodic area can be found. Moreover, some unclosed holes are observed on the coating surface. The cross-sectional images prove that there are big pores under the volcano-like structure (Fig. 4.11B). The big pores are caused by gas evolution associated with the strong discharges [27]. Besides, many small pores are observed on the cross-sectional morphology and the barrier layer seems to still be honeycomb structure (Fig. 4.11C), indicating the processes of gas evolution and ion migration at the barrier layer. The honeycombs at the bottom of big pores also prove this speculation (Fig. 4.11B). Moreover, Cheng et al. [44] have proposed that there should be secondary internal discharges in the big pores, which would cause heating and softening of the outer layer that allows the outer layer to be pushed outward due to stress generated by gas evolution from the formation of the inner layer.

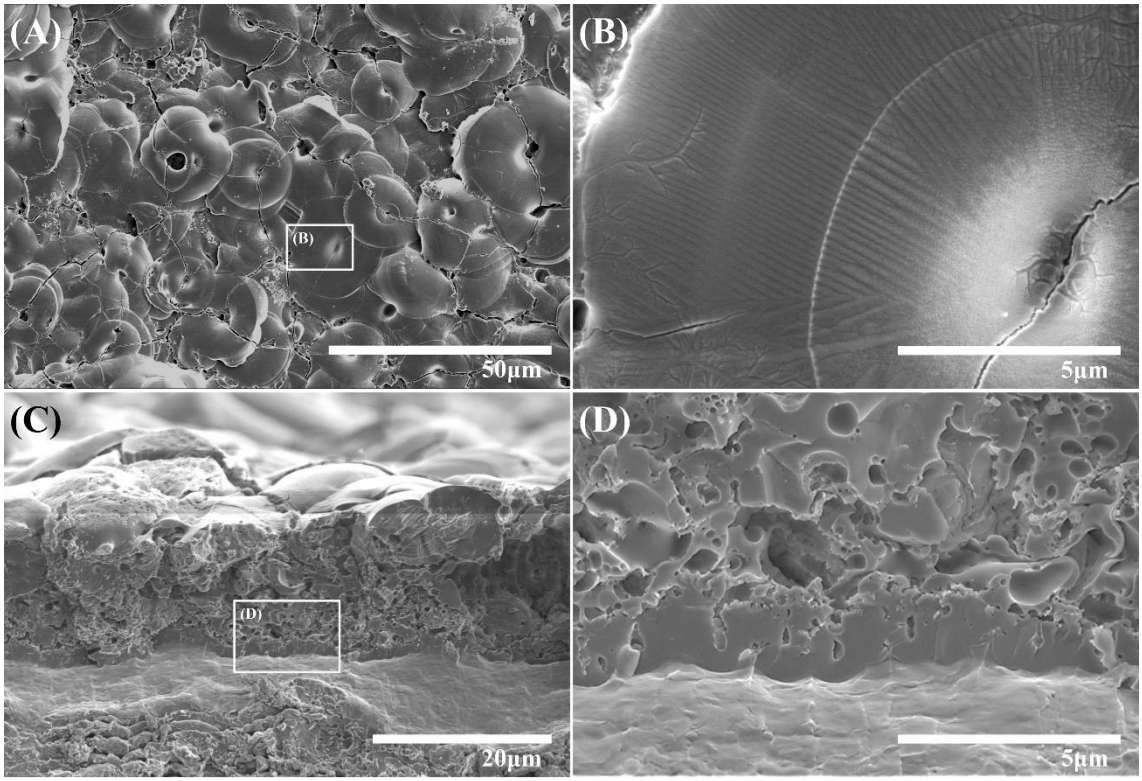

Fig. 4.12 Surface and cross-sectional morphologies of sample 4#. (A) surface image; (C) cross-sectional image; (B) and (D) are the higher magnification images of the box areas of (A) and (C), respectively.

Fig. 4.12 shows the morphologies of the coating when the sparks have just been extinguished. Clearly, the more dense and thick MAO coating is formed (Fig. 4.12A and C). The dendritic crystal caused by solidification of molten coating material can be observed in Fig. 4.12B, which implies a strong crystallization transformation and possible isotherm from the oval circle. When the sparks are extinguished and high-pressure state of plasma in the coating is released, the electrolyte would easily reach the barrier layer via cracks, pores or discharge channels, hence reducing the coating impedance (Fig. 4.5). The growing barrier layer would no longer be bombarded by sparks, and therefore, it grows up a little in a short time (Fig. 4.12D).

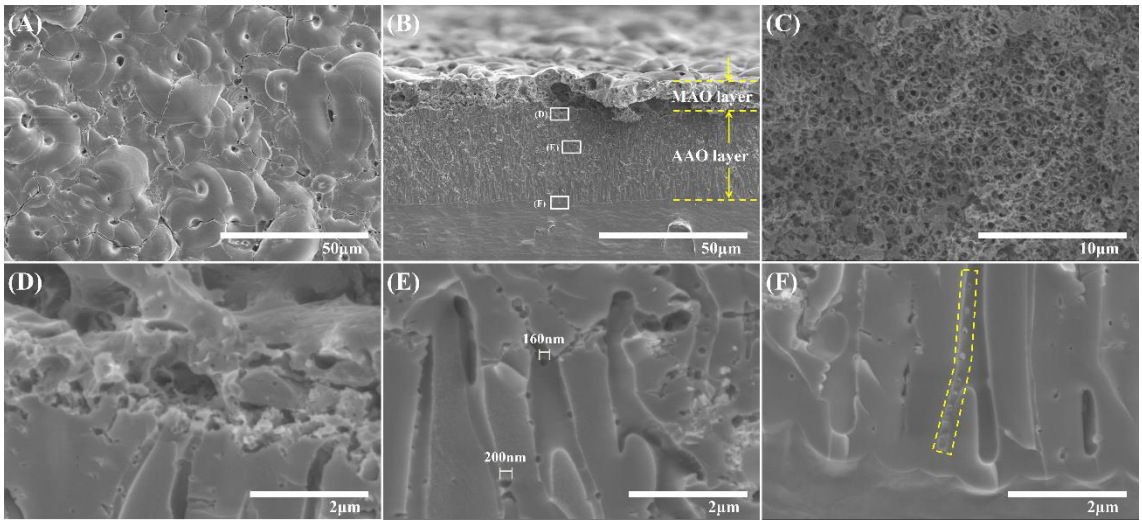

Fig. 4.13 Surface and cross-sectional morphologies of sample 5#. (A) surface image; (B) cross-sectional image; (C) the surface image after removed the outer layer; (D)-(F) are the higher magnification images of the box areas of (B), respectively.

Fig. 4.13 presents the morphologies of coating after 3 h oxide treatment. It clearly observes the coating with outer MAO layer and inner AAO layer (Fig. 4.13B). The inner AAO layer undoubtedly grows up in stage IV (Fig. 4.5B). Moreover, some pits (160~200 nm) can be observed on the hole wall of AAO layer (Fig. 4.13E) and the bubbling behavior with smaller diameter can be observed in extruded honeycomb near the barrier layer (Fig. 4.13F). These pits may be caused by the discharge of the bubbles adsorbed on the wall, which was proved by the slight current fluctuation at the end of stage IV (Fig.

4.5B). These discharges do not have enough energy to pass through the AAO layer. The increase in the pit size can be attributed to the acidic dissolution. Similarly, the MAO layer would also suffer from corrosion of the electrolyte. After the sparks are extinguished, as MAO layer is continuously corroded by electrolyte, its blocking ability to the electrolyte is reduced, resulting in a continuous voltage drop (60~90 min of Fig. 4.5B). In addition, the morphological instability caused by reorganization of embryo pores should also be considered.

4.3.6 Coating growth kinetics

Fig. 4.14 shows the morphologies of coating near the O-ring prepared on sample 5#. Clearly, the area of coating not affected by sparks can be observed. This phenomenon is caused by the penetration of HEDP into the gap between the O-ring and substrate (Fig. 4.14C). This indicates that the anodizing regime always powers the growth of coating from stages I to IV. Actually, the electrolyte can still reach the barrier layer during the discharge process [34, 44], which provides conditions for anodizing here. Moreover, the different coating areas (spark and non-spark areas, Fig. 4.14B) are on the same horizontal line, indicating that the growth of coating is hardly promoted by sparks. It should be noted that nothing can be sintered on the anode from pure HEDP solution by sparks except for a small amount of aluminum-containing chelate.

The dependence of coating thickness on time is presented in Fig. 4.15A. It reveals a linear trend of outward growth rate of ~0.16 μm/min. By contrast, the inward growth rate (approximately ~0.10 μm/min) seems to share a type of “fast followed by slow” under the influence of sparks. However, the inward growth rate during the stage III (30~55min, Fig. 4.15A), where strong plasma discharge appears (Fig. 4.6C and D), has dropped and is the same as stage IV. It proves again that the plasma discharges have little contribution to coating thickening. Thus, the same gentle growth process of ion migration can be used to describe the stages of I~IV. The relative higher growth rate of the coating during stage I~III should be attributed to the pits as a result of plasma discharge on the initial thin

coating (Figs. 4.9D and 4.10B).

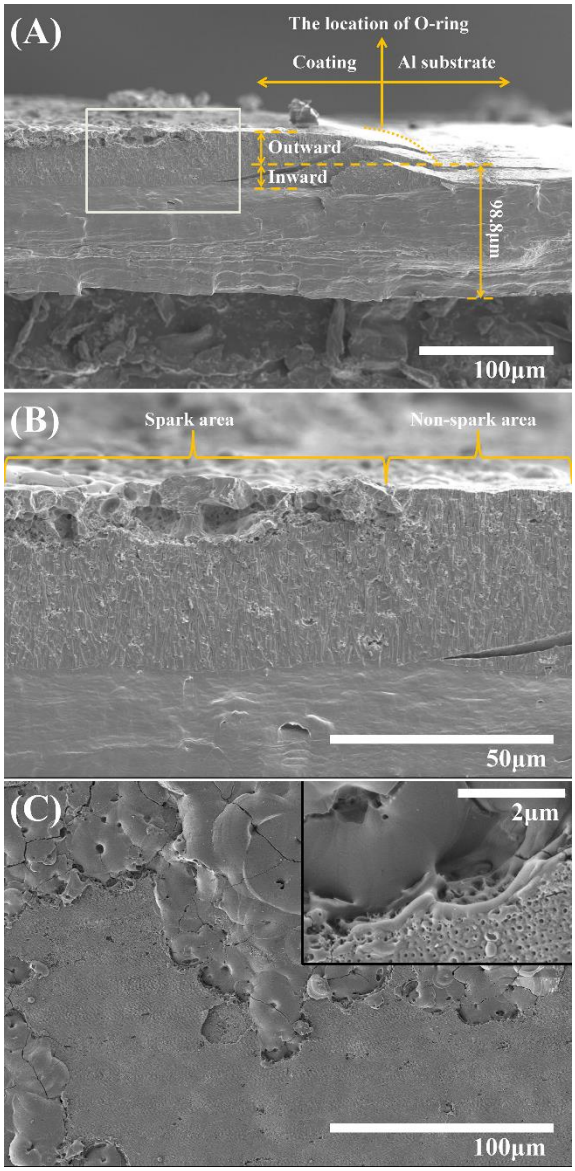

Fig. 4.14 (A) and (C) are the cross-sectional and surface morphologies of sample 5# near the O-ring, respectively; (B) The higher magnification image of the box area of (A).

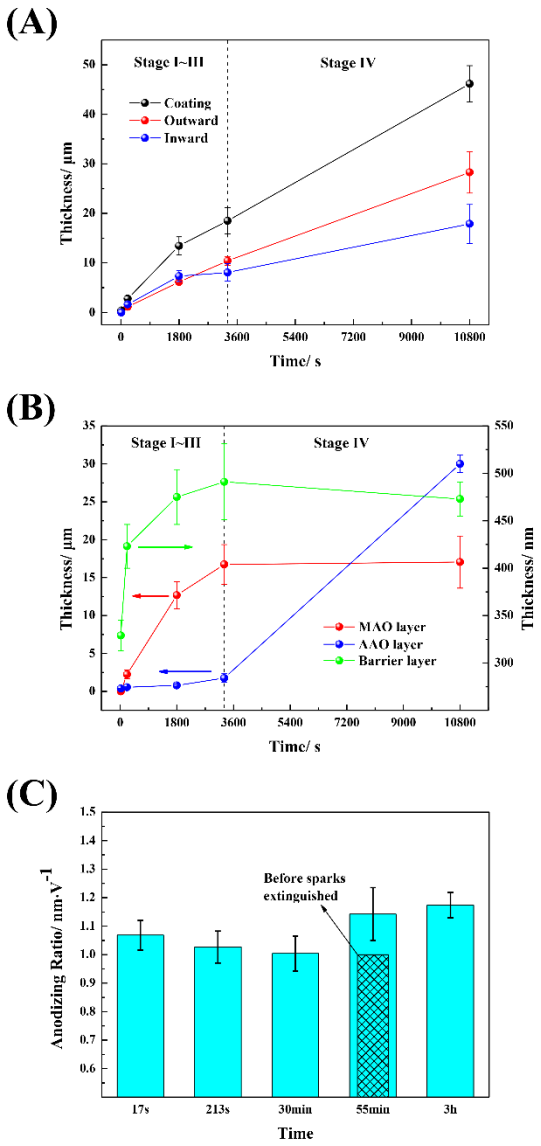

Fig. 4.15 (A) The outward, inward growth curves of coating; (B) The changes in thickness of sub-layers; (C) The calculated anodizing ratio of coating.

Fig. 4.15B shows the changes in thickness of sub-layers of coating. The MAO and AAO layers grow up in the different stages, respectively. The thickness of barrier layer (t_b) gradually increases with oxidation time, which eventually reaches ~475 nm. Generally,

it is believed that the main voltage drop is loaded on the barrier layer of anodic film, ignoring the small impedances of porous layer and electrolyte. The "anodizing ratio ($AR=t_b/U$)" is used to describe the dependence between the thickness of barrier layer (t_b) and working voltage (U), which determines the ionic current ($\boldsymbol{J}_{ion}$) according to the exponential law [5, 45, 46]:

$$\boldsymbol{J}_{ion} = \boldsymbol{A}\exp(\boldsymbol{B}\Delta U/t_b) \quad [4.2]$$

where $\boldsymbol{A}$ and $\boldsymbol{B}$ are material-dependent constants at a given temperature. Recently, Zhu et al. [14] proved that the AR is still applicable to MAO coating. Moreover, the existence of the electronic current ($\boldsymbol{J}_e$) has been testified by researches [47, 48], which is used to explain the evolution of oxygen bubbles on the anode ($2O^{2-} \rightarrow O_2 + 4e$ or $4OH^- \rightarrow O_2 + 2H_2O + 4e$). The $\boldsymbol{J}_e$ increases exponentially with the increase of t_b and conforms to the following expansion:

$$\boldsymbol{J}_e = \boldsymbol{j_o}\exp(\boldsymbol{\alpha} t_b) \quad [4.3]$$

where $\boldsymbol{j}_o$ and $\boldsymbol{\alpha}$ are the primary electronic current and impact ionization coefficient of the avalanche, respectively. The total current is composed of ionic current and electronic current, i.e. $\boldsymbol{J} = \boldsymbol{J}_{ion} + \boldsymbol{J}_e$.

Fig. 4.15C shows the dependence of AR vs time with a range of 1.0~1.2 nm/V, which is consistent with the AR for various electrolytes [16, 49-51]. Hence, the $\boldsymbol{J}_{ion}$ is basically kept constant, which implies the stable growth of coating in all stages. For the case of CC mode, the increase of t_b (Fig. 4.15B) results in the increase of $\boldsymbol{J}_e$, the decrease of $\boldsymbol{J}_{ion}$ and then the increase of AR (17 s and 3h of Fig. 4.15C). Nevertheless, the $\boldsymbol{J}_{ion}$ is much larger than the $\boldsymbol{J}_e$, and therefore the growth rate of coating is almost unaffected [23]. Moreover, the AR slightly decreases first (213s and 30 min of Fig. 4.15C) because the generated MAO layer is covered on barrier layer. After sparks are extinguished, the impedance of MAO layer is completely removed with the immersion of electrolyte, thus increasing the calculated AR. On the other hand, the reaction involved in anodic oxidation of aluminum is exothermic and the rise in temperature can be several tens of degrees centigrade at high current densities [52]. The increase of the coating thickness is bound to result in the

decrease of heat conduction. Then, the local higher temperature would cause a thinner barrier layer (Fig. 4.15C) and slight voltage drop (120~180 min, Fig. 4.5B) due to acidic dissolution [50].

4.3.7 Proposed growth mechanism

According to the electrical signal-time responses and structural characterization presented above, the growth process of coating formed in HEDP at high current density can be divided into four stages, as schemed in Fig. 4.16.

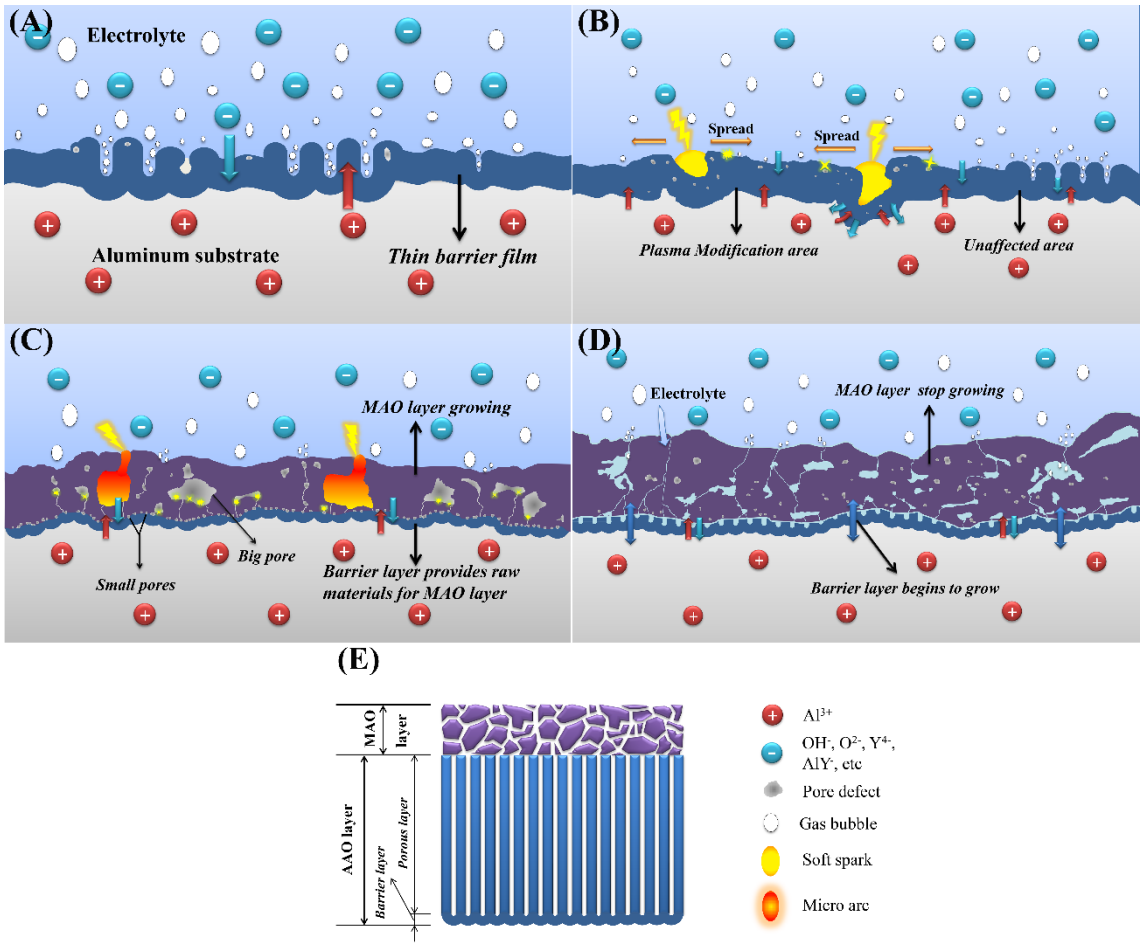

Fig. 4.16 The schematic diagram of the growth mechanism of coating prepared in HEDP at high current density

Passivation stage (Fig. 4.16A): Initially, the anodic barrier film fast grows in a short time, and then the embryo pores generate with gas evolution. The outward immigrant Al^{3+} from the substrate reacts with the inward immigrant O^{2-}, OH^- and acid-anion (e.g. Y^{4-} and

AlY^{4-}) at the solid-liquid interface. An increase of current density leads to more incorporation of acid-anion in the film until the oxide cracking (Fig. 4.3) caused by volume expansion appears. The way to gradually increase the current may help to avoid the burning, which needs further studies.

Soft sparking stage (Fig. 4.16B): As the growth of the anodic film, the voltage quickly increases to 300 V. Then, the electric field applied on the gas fills in the channel and pore-defects of film sufficiently excites the spark discharges. However, the aluminum separated by spark from substrate would be dissolved by HEDP, but not deposited on anode through the form of oxide (Figs. 4.9 and 4.10). Moreover, the temperature of soft sparks insufficiently melts the generated alumina, but the craters and many micro pores would form around the PM area (Fig. 4.9D). These pore-defects would further promote the spread of sparks and even cover the entire surface.

Micro arcing stage (Fig. 4.16C): The soft sparks would transform to high energy sparks, i.e. micro arcs, with the voltage increases up to 400V (Fig. 4.6). Micro arcs would cause the crystallization of oxides, and thus the outer MAO layer begins to form. Moreover, ion exchange still occurs on the barrier layer in this stage. The porous MAO layer can allow the immersion of electrolyte, and hence the electrolyte would be excluded the sparking at the moment accompanying with strong electric signal fluctuation (Fig. 4.5). The generated gas and the defects caused by extrusion of growing barrier layer to MAO layer would arouse gas discharges and dielectric breakdown. The micro arcs only heat and melt the coating material, and the bottom barrier layer provides the raw materials for growth of MAO layer. The small pores (Figs. 4.11C and 4.12D) observed near the barrier layer are the evidence of gas evolution. Contrasting with the widely used electrolytes containing cationic/anionic components that incorporate other elements into the coating or suspensions that provide cataphoretic transport of macroparticles [8], no other material can be deposited on the MAO layer by sparks in pure HEDP solution. For the given current density, the strong discharges would gradually disappear after the thickness of MAO layer reaches a certain value due to insufficient energy for breakdown.

Anodizing stage (Fig. 4.16D): After the high-pressure state of plasma in the coating is released, the electrolyte enters into the gap of the coating, in turn, giving rise to the formation of AAO layer. As the AAO layer is continuously thickened, a MAO/AAO composite coating is finally formed (Fig. 4.16E). Notably, the AAO layer proves the possibility of preparing anodic film in HEDP solution at 400V or higher, while the highest voltage so far is 280 V [16, 50, 51], which also needs further studies.

4.4 Conclusions

We present the systematic study on the growth behavior of coating formed in HEDP at the overlapping electrochemical windows of anodizing and MAO. The conclusions are as follows:

1. The soft parks would be aroused when the voltage reaches 300 V, which generates the pits and micro pores on the barrier layer. The micro pores would further promote the appearance of micro-arcs. The burning of barrier layer at 8 A/dm^2 is caused by oxide cracking.

2. The MAO regime forms MAO layer first, and then the sparks would automatically extinguish and electrolyte would immerse in the coating. Afterwards, the inner AAO layer begins to grow under the anodizing regime. Finally, the MAO/AAO composite coating is obtained.

3. The growth kinetics for the whole stages is a linear type, which comes from the ion migration at the barrier layer. The discharges have few contributions to coating thickening. The barrier layer would be partially converted into MAO layer after being bombarded by discharges.

References

[1] Y. Ma, X. Zhou, Y. Liao, X. Chen, C. Zhang, H. Wu, Z. Wang, W. Huang, Effect of anodizing parameters on film morphology and corrosion resistance of AA2099 aluminum-lithium alloy, J. Electrochem. Soc., 163 (2016) C369-C376.

[2] T. Kikuchi, A. Takenaga, S. Natsui, R.O. Suzuki, Advanced hard anodic alumina coatings via etidronic acid anodizing, Surf. Coat. Tech., 326 (2017) 72-78.

[3] G. Alcalá, S. Mato, P. Skeldon, G.E. Thompson, A.B. Mann, H. Habazaki, K. Shimizu, Mechanical properties of barrier-type anodic alumina films using nanoindentation, Surf. Coat. Tech., 173 (2003) 293-298.

[4] H. Wu, Y. Higaki, A. Takahara, Molecular self-assembly of one-dimensional polymer nanostructures in nanopores of anodic alumina oxide templates, Prog. Polym. Sci., 77 (2018) 95-117.

[5] W. Lee, S.-J. Park, Porous anodic aluminum oxide: Anodizing and templated synthesis of functional nanostructures, Chem. Rev., 114 (2014) 7487-7556.

[6] H. Huang, X. Wei, J. Yang, J. Wang, Influence of surface micro grooving pretreatment on MAO process of aluminum alloy, Appl. Surf. Sci., 389 (2016) 1175-1181.

[7] M. Fazel, H.R. Salimijazi, M. Shamanian, Improvement of corrosion and tribocorrosion behavior of pure titanium by subzero anodic spark oxidation, ACS Appl. Mater. Inter., 10 (2018) 15281-15287.

[8] A.L. Yerokhin, X. Nie, A. Leyland, A. Matthews, S.J. Dowey, Plasma electrolysis for surface engineering, Surf. Coat. Tech., 122 (1999) 73-93.

[9] Y.-l. Cheng, J.-h. Cao, M.-k. Mao, Z.-m. Peng, P. Skeldon, G.E. Thompson, High growth rate, wear resistant coatings on an Al–Cu–Li alloy by plasma electrolytic oxidation in concentrated aluminate electrolytes, Surf. Coat. Tech., 269 (2015) 74-82.

[10] Y.-l. Cheng, X.-Q. Wu, Z.-g. Xue, E. Matykina, P. Skeldon, G.E. Thompson, Microstructure, corrosion and wear performance of plasma electrolytic oxidation coatings formed on Ti–6Al–4V alloy in silicate-hexametaphosphate electrolyte, Surf. Coat. Tech., 217 (2013) 129-139.

[11] J.A. Curran, H. Kalkancı, Y. Magurova, T.W. Clyne, Mullite-rich plasma electrolytic oxide coatings for thermal barrier applications, Surf. Coat. Tech., 201 (2007) 8683-8687.

[12] L.R. Krishna, A.S. Purnima, G. Sundararajan, A comparative study of tribological behavior of microarc oxidation and hard-anodized coatings, Wear, 261 (2006) 1095-1101.

[13] J.M. Wheeler, J.A. Curran, S. Shrestha, Microstructure and multi-scale mechanical behavior of hard anodized and plasma electrolytic oxidation (PEO) coatings on aluminum alloy 5052, Surf. Coat. Tech., 207 (2012) 480-488.

[14] L. Zhu, Z. Guo, Y. Zhang, Z. Li, M. Sui, A mechanism for the growth of a plasma electrolytic oxide coating on Al, Electrochim. Acta, 208 (2016) 296-303.

[15] W. Lee, J.-C. Kim, U. Gösele, Spontaneous current oscillations during hard anodizing of aluminum under potentiostatic conditions, Adv. Funct. Mater., 20 (2010) 21-27.

[16] A. Takenaga, T. Kikuchi, S. Natsui, R.O. Suzuki, Exploration for the self-ordering of porous alumina fabricated via anodizing in etidronic acid, Electrochim. Acta, 211 (2016) 515-523.

[17] B. Gastón-García, E. García-Lecina, J.A. Díez, M. Belenguer, C. Müller, Local burning phenomena in sulfuric acid anodizing: Analysis of porous anodic alumina layers on AA1050, Electrochem. Solid State Lett., 13 (2010) C33-C35.

[18] C. Lämmel, M. Schneider, C. Heubner, W. Beckert, A. Michaelis, Investigations of burning phenomena during the hard anodising of aluminium by local in-operando temperature measurements, Electrochim. Acta, 249 (2017) 271-277.

[19] D. Elabar, T. Hashimoto, J. Qi, P. Skeldon, G.E. Thompson, Effect of low levels of sulphate on the current density and film morphology during anodizing of aluminium in chromic acid, Electrochim. Acta, 196 (2016) 206-222.

[20] R. Elaish, M. Curioni, K. Gowers, A. Kasuga, H. Habazaki, T. Hashimoto, P. Skeldon, Influence of fluorozirconic acid on sulfuric acid anodizing of aluminum, J. Electrochem. Soc., 164 (2017) C831-C839.

[21] M. Pashchanka, J.J. Schneider, Self-ordering regimes of porous anodic alumina layers formed in highly diluted sulfuric acid electrolytes, J. Phys. Chem. C, 120 (2016)

14590-14596.

[22] Y. Li, Y. Qin, S. Jin, X. Hu, Z. Ling, Q. Liu, J. Liao, C. Chen, Y. Shen, L. Jin, A new self-ordering regime for fast production of long-range ordered porous anodic aluminum oxide films, Electrochim. Acta, 178 (2015) 11-17.

[23] M. Yu, W. Zhang, S. Zhang, S. Zhao, F. Ai, X. Zhu, Morphology evolution of porous anodic alumina in mixed H_3PO_4/NH_4F electrolytes, Surf. Coat. Tech., 334 (2018) 500-508.

[24] S. Zhao, L. Wu, C. Li, C. Li, M. Yu, H. Cui, X. Zhu, Fabrication and growth model for conical alumina nanopores – Evidence against field-assisted dissolution theory, Electrochem. Commun., 93 (2018) 25-30.

[25] N. Sato, A theory for breakdown of anodic oxide films on metals, Electrochim. Acta, 16 (1971) 1683-1692.

[26] H.R. Wang, F. Liu, Y.P. Zhang, D.Z. Yu, F.P. Wang, Preparation and properties of titanium oxide film on NiTi alloy by micro-arc oxidation, Appl. Surf. Sci., 257 (2011) 5576-5580.

[27] Y. Cheng, J. Cao, M. Mao, H. Xie, P. Skeldon, Key factors determining the development of two morphologies of plasma electrolytic coatings on an Al–Cu–Li alloy in aluminate electrolytes, Surf. Coat. Tech., 291 (2016) 239-249.

[28] V. Dehnavi, B.L. Luan, D.W. Shoesmith, X.Y. Liu, S. Rohani, Effect of duty cycle and applied current frequency on plasma electrolytic oxidation (PEO) coating growth behavior, Surf. Coat. Tech., 226 (2013) 100-107.

[29] J. Martin, A. Melhem, I. Shchedrina, T. Duchanoy, A. Nominé, G. Henrion, T. Czerwiec, T. Belmonte, Effects of electrical parameters on plasma electrolytic oxidation of aluminium, Surf. Coat. Tech., 221 (2013) 70-76.

[30] R.H.U. Khan, A. Yerokhin, X. Li, H. Dong, A. Matthews, Surface characterisation of DC plasma electrolytic oxidation treated 6082 aluminium alloy: Effect of current density and electrolyte concentration, Surf. Coat. Tech., 205 (2010) 1679-1688.

[31] M.S. Yilmaz, O. Sahin, Applying high voltage cathodic pulse with various pulse

durations on aluminium via micro-arc oxidation (MAO), Surf. Coat. Tech., 347 (2018) 278-285.

[32] T. Mi, B. Jiang, Z. Liu, L. Fan, Plasma formation mechanism of microarc oxidation, Electrochim. Acta, 123 (2014) 369-377.

[33] A.L. Yerokhin, L.O. Snizhko, N.L. Gurevina, A. Leyland, A. Pilkington, A. Matthews, Discharge characterization in plasma electrolytic oxidation of aluminium, J. Phys. D: Appl. Phys., 36 (2003) 2110-2120.

[34] C. Liu, D. He, Q. Yan, Z. Huang, P. Liu, D. Li, G. Jiang, H. Ma, P. Nash, D. Shen, An investigation of the coating/substrate interface of plasma electrolytic oxidation coated aluminum, Surf. Coat. Tech., 280 (2015) 86-91.

[35] Y. Zhang, Y. Wu, D. Chen, R. Wang, D. Li, C. Guo, G. Jiang, D. Shen, S. Yu, P. Nash, Micro-structures and growth mechanisms of plasma electrolytic oxidation coatings on aluminium at different current densities, Surf. Coat. Tech., 321 (2017) 236-246.

[36] L. Zhu, X. Ke, J. Li, Y. Zhang, Z. Chen, Z.H. Zhang, Y. Lu, M. Sui, Nature of the growth of plasma electrolyte oxidation coating on Aluminum, arXiv preprint arXiv:1712.02459 (2017).

[37] H. Huang, J. Qiu, M. Sun, W. Liu, X. Wei, E. Sakai, K. Ito, A hard coating with MAO/AAO double layers prepared on aluminum in etidronic acid by DC oxidation, Surf. Coat. Tech., 360 (2019) 307-317.

[38] C. Xu, W. Gao, Pilling-Bedworth ratio for oxidation of alloys, Mater. Res. Innov., 3 (2000) 231-235.

[39] X.-w. Wei, C.-y. Chen, Influence of oxidation heat on hard anodic film of aluminum alloy, T. Nonferr. Metal. Soc., 22 (2012) 2707-2712.

[40] I. Vrublevsky, V. Parkoun, V. Sokol, J. Schreckenbach, G. Marx, The study of the volume expansion of aluminum during porous oxide formation at galvanostatic regime, Appl. Surf. Sci., 222 (2004) 215-225.

[41] F. Zhou, A.K. Mohamed Al-Zenati, A. Baron-Wiecheć, M. Curioni, S.J. Garcia-Vergara, H. Habazaki, P. Skeldon, G.E. Thompson, Volume Expansion Factor and

Growth Efficiency of Anodic Alumina Formed in Sulphuric Acid, J. Electrochem. Soc., 158 (2011) C202-C214.

[42] Y. Cheng, T. Wang, S. Li, Y. Cheng, J. Cao, H. Xie, The effects of anion deposition and negative pulse on the behaviours of plasma electrolytic oxidation (PEO)—A systematic study of the PEO of a Zirlo alloy in aluminate electrolytes, Electrochim. Acta, 225 (2017) 47-68.

[43] W. Tu, Y. Cheng, X. Wang, T. Zhan, J. Han, Y. Cheng, Plasma electrolytic oxidation of AZ31 magnesium alloy in aluminate-tungstate electrolytes and the coating formation mechanism, J. Alloys Compd., 725 (2017) 199-216.

[44] Y.-l. Cheng, Z.-g. Xue, Q. Wang, X.-Q. Wu, E. Matykina, P. Skeldon, G.E. Thompson, New findings on properties of plasma electrolytic oxidation coatings from study of an Al–Cu–Li alloy, Electrochim. Acta, 107 (2013) 358-378.

[45] B. Chong, D. Yu, R. Jin, Y. Wang, D. Li, Y. Song, M. Gao, X. Zhu, Theoretical derivation of anodizing current and comparison between fitted curves and measured curves under different conditions, Nanotechnology, 26 (2015) 145603.

[46] X.F. Zhu, Y. Song, L. Liu, C.Y. Wang, J. Zheng, H.B. Jia, X.L. Wang, Electronic currents and the formation of nanopores in porous anodic alumina, Nanotechnology, 20 (2009) 475303.

[47] A. Mazzarolo, M. Curioni, A. Vicenzo, P. Skeldon, G.E. Thompson, Anodic growth of titanium oxide: Electrochemical behaviour and morphological evolution, Electrochim. Acta, 75 (2012) 288-295.

[48] J.M. Albella, I. Montero, J.M. Martinez-Duart, A theory of avalanche breakdown during anodic oxidation, Electrochim. Acta, 32 (1987) 255-258.

[49] S.Z. Chu, K. Wada, S. Inoue, M. Isogai, Y. Katsuta, A. Yasumori, Large-scale fabrication of ordered nanoporous alumina films with arbitrary pore intervals by critical-potential anodizing, J. Electrochem. Soc., 153 (2006).

[50] M. Sepúlveda, J.G. Castaño, F. Echeverría, Influence of temperature and time on the fabrication of self-ordering porous alumina by anodizing in etidronic acid, Appl. Surf.

Sci., 454 (2018) 210-217.

[51] T. Kikuchi, O. Nishinaga, S. Natsui, R.O. Suzuki, Fabrication of self-ordered porous alumina via etidronic acid anodizing and structural color generation from submicrometer-scale dimple array, Electrochim. Acta, 156 (2015) 235-243.

[52] L.E. Fratila-Apachitei, I. De Graeve, I. Apachitei, H. Terryn, J. Duszczyk, Electrode temperature evolution during anodic oxidation of AlSi(Cu) alloys studied in the wall-jet reactor, Surf. Coat. Tech., 200 (2006) 5343-5353.

Chapter 5 Ultra-fast fabrication of porous alumina film with excellent wear and corrosion resistance via HEDP hard anodizing

5.1 Introduction

Anodizing is the most commonly used surface strengthening technology applied to aluminum through the fabrication of a so-called porous anodic alumina (PAA) film [1-3]. Although the ordered PAA is widely used as the template for assembling nanomaterials due to its unique honeycomb nanopore structure [4-6], the anodizing process was first implemented in the 1920s for the purpose of protection [7], which does not necessarily require a highly ordered PAA. Many excellent engineering properties can be attached to aluminum via anodizing, such as wear resistance [8, 9], corrosion resistance [10, 11], and thermal and electrical insulations [12, 13].

Generally, PAA film consists of an outer porous layer and inner barrier layer, which dominate the mechanical properties and corrosion resistance, respectively. For the mechanical properties, the PAA porosity, which depends on both its pore diameter and inter pore distance, is the critical index. On the other hand, it is widely believed that the thicker the barrier layer, the higher the corrosion resistance of PAA. Subsequent sealing processes on PAA via water vapor or metal salt solutions are frequently carried out to further improve its corrosion resistance [14]. Nevertheless, these basic performance strongly depend on the type of electrolytes in which the PAA films are fabricated, such as chromic [15], sulfuric [16], oxalic [17], phosphoric [12], citric [18], selenic [19], and maleic [20] acids. Among these electrolytes, sulfuric acid anodizing is currently the primary commercial method for the surface reinforcement of aluminum alloy, due to factors of solution stability, formation efficiency, and film performance. However, the

sulfuric-acid-anodized film (Sul-film) still struggles to meet the industrial demands for performance and environmental protection, even though sulfuric acid hard anodizing [21, 22] has been developed.

More recently, the environmentally friendly etidronic acid (HEDP) anodizing has been proposed by Kikuchi et al. [23, 24] to fabricate ordered PAA in the submicron level with special structural coloration. They found that the anodized film prepared in etidronic acid (Eti-film) can retain a higher hardness (~600 HV) than can the hard Sul-film (300–550 HV) due to the low porosity (as low as 4%) [25]. Moreover, it was reported that the thick barrier layer of Eti-film promises an excellent alkaline corrosion resistance due to a high anodizing voltage (200–300 V) [14]. However, rapidly fabricating the Eti-film with a certain thickness is still a challenge.

Regarding the anodizing efficiency of Eti-film, Sepúlveda, et al. [26] noted that the growth rate of Eti-film can reach ~20 μm/h during potentiostatic anodizing at a high temperature (270V, 40ºC). However, galvanostatic anodizing is actually more suitable for industrial production than is potentiostatic anodizing. Subsequently, Iwai et al. [27] investigated the time required for the recovery of the anodizing voltage and the burning current densities via galvanostatic anodizing in HEDP solutions with different temperatures; however, they did not mention the growth rate of Eti-film. It is well known that the growth rate of PAA strongly depends on the applied current density [28, 29], while an excessive current causes the burning of PAA due to the accelerated acidic dissolution of the film induced by the reaction heat (also called Joule heat) [30, 31]. Whereupon, Huang et al. [32, 33] combined the single-sided and low-temperature (0–10 ºC) techniques to timely remove the reaction heat of HEDP anodizing at high current density (~8 A/dm^2), while a micro-arc oxidation (MAO) regime was aroused and a coating with MAO/PAA double layers was ultimately prepared. Notably, the PAA layer galvanostatically prepared at 4–7 A/dm^2 implied the possibility of HEDP hard anodizing [32,33].

In this study, we demonstrated the fast-fabrication strategy of Eti-film on 6063T5

aluminum alloy. The growth behaviors and microstructures of the Eti-film were first investigated just under the burning current densities in the temperature range of 15–45°C, and the optimal temperature for the fast-fabrication strategy of Eti-films was determined to be 35°C. Then, the possibility of super-high-current anodizing (up to 15 A/dm^2) in an HEDP solution was proven via a gradient-increase-current approach; ultimately resulting in a high growth rate (2.1 μm/min), excellent hardness (up to 11 GPa) and branched-nanoholes structure of Eti-film. Moreover, the anodizing voltage broke the limit of ~300 V reported in the literature [24] and reached ~460V, causing a much thicker barrier layer (~510 nm). By comparison, the wear and corrosion performance of the hard-anodized Eti-film was much better than that of the hard-anodized Sul-film.

5.2 Experimental procedure

5.2.1 Sample preparation

6063T5 aluminum alloy (UACJ, JP) was cut into rectangular pieces (40 mm×10 mm×2 mm) and ground with abrasive papers (320–800#). Then, the pieces were electrochemically polished in a 60 wt% $HClO_4$ /C_2H_5OH mixture (v: v = 1: 4) at 25 V for 2.5 min under -5–5ºC. Finally, all samples were sealed with an exposed area of 3.8 cm^2. The compositions of the 6063T5 aluminum alloy are listed in Table 5.1.

Table 5.1 Composition of 6063T5 aluminum alloy in wt%

Si	Fe	Cu	Mn	Mg	Cr	Zn	Ti	Others	Al
0.40	0.15	0.00	0.02	0.48	0.00	0.00	0.01	< 0.05	Balance

The details of the electrolytic cell have been described elsewhere [32]. The anodizing was conducted in 0.2 M etidronic acid ($CH_3C(OH)[PO(OH)_2]_2$, HEDP, TCI, JP) solution with temperatures of 15, 25, 35 and 45 ± 0.5ºC at 0.5–15 A/dm^2 for 1h or until the appearance of the critical electrical breakdown of the film. A power supply (PWR1201H, Kikusui Electronics, JP) was used for anodizing and the electric signals were measured during the anodizing process.

The hard-anodized Sul-film was also prepared on 6063T5 aluminum alloy in 30 wt%

sulfuric acid solution at -5 ± 0.5ºC, 3 A/dm^2 current density, and 75% duty cycle (to avoid burning) to compare with the Eti-film. The thicknesses of both the Sul-film and Eti-film used for performance comparison were adjusted to ~40 μm.

5.2.2 Characterization

The broken sections of anodized films were fabricated to observe the barrier layer; the polished cross-sections of the anodized films after mounting in epoxy resin were prepared for thickness and hardness measurements. The surface and cross-sectional morphologies of the anodized films were investigated by scanning electron microscopy (SEM, S-4300 and SU-70, Hitachi, JP). Before the SEM examination, all samples were coated with platinum to increase their conductivity. The pore diameter, porosity, and thickness of the anodized films were measured from the SEM images using software (Image J 1.42q).

The elemental compositions and distributions of the Eti-films were evaluated via energy dispersive spectrometry (EDS, Oxford Instruments) coupled to the SEM (SU-70) and X-ray photoelectron spectroscopy (XPS, ESCA5400, ULVAC-PHI, JP). The samples used for the XPS measurements were etched with argon ions for 5 min in advance, and the XPS spectra were corrected by reference to the Ar2p3/2 (242 eV) and Ar2p1/2 (244 eV) peaks.

The crystal state of the Eti-film was determined by using a high-resolution X-ray diffractometer (XRD, SmartLab9K-INP, Rigaku, JP) and selected-area electron diffraction (SAED) analysis via a transmission electron microscope (TEM, HT7830, Hitachi, JP) at 120 kV. The sample used for TEM was fabricated with a the focused ion beam (FIB, FB2000A, Hitachi, JP).

The hardness H_{IT} and elastic modulus E_{IT} of the anodized films were measured on their cross-sections at a load of 0.025 N for 10 s by a nanoindentation tester (DUH-211, Shimadzu, JP) equipped with a Berkovitch diamond indenter. The hardness was also evaluated via the Vickers method at a load of 0.1 N (HM-200, Mitutoyo, JP). Each value was measured at least three times, and the average was taken. The wear resistance of the

film was evaluated by the reciprocating motion approach of an UMT TriboLab (BRUKER, USA) for 30 min. A GCr15 steel ball (Φ 9.5 mm, HRC 62) and the anodized aluminum block were set as the friction pairs. The load was 10 N and the frequency was 5 Hz. The wear scars were examined with a profilometer (Form Talysurf Intra, Taylor Hobson, UK) and SEM-EDS.

An electrochemical workstation (CS2350H, Corrtest, CHN) was used to analyze the corrosion resistance of the films with electrochemical impedance spectroscopy (EIS) and potentiodynamic polarization tests in a 3.5 wt% NaCl solution at room temperature (20~25ºC). A saturated calomel electrode (SCE), a platinum plate, and the anodized aluminum were set as the reference, counter, and working electrodes, respectively. Before the test, the samples were sealed with the evaluated areas of 1 cm^2, then immersed in NaCl solution for 1 h to reach a steady open-circuit potential (OCP). Afterwards, an EIS measurement was performed by applying the signal amplitude of 10 mV on an OCP over a frequency from 10^{-2} to 10^5 Hz, 1 point per decade. Potentiodynamic polarization was carried out by applying a ± 250 mV polarization based on the OCP at a scanning rate of 1 mV/s. Zview and Cview software were used to simulate the EIS and polarization data, respectively.

5.3 Results and discussion

5.3.1 Effect of electrolyte temperature on the Eti-film

First, we investigated the HEDP anodizing behavior of 6063T5 aluminum alloy at different temperatures (15, 25, 35, and 45°C), as shown in Fig. 5.1. Large differences in the voltage-time curves were observed (Fig. 5.1A). During the anodizing process at 15°C, the voltage quickly increased to ~400 V in 1200 s. Both a soft spark on the aluminum anode and the voltage fluctuation were observed at the same time, which imply the establishment of the MAO regime [32, 33]. Because of the low conductivity and high viscosity of the HEDP solution at a relatively low temperature [33], the electrical

breakdown value of the bubbles generated in the nanopores can be easily reached; thus, a porous MAO coating was ultimately formed (Fig. 5.2A).

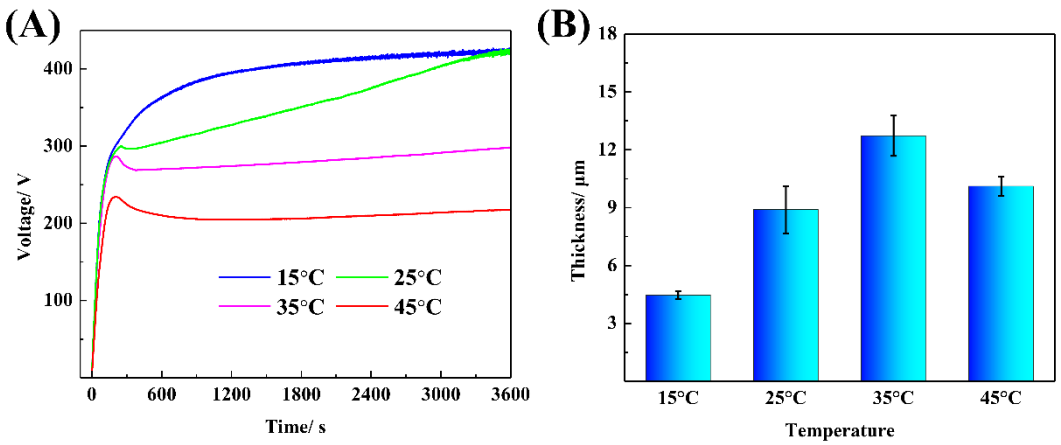

Fig. 5.1 (A) Voltage-time curves of anodizing at 1 A/dm^2 for 1 h with different HEDP temperatures; (B) thicknesses of the resultant Eti-films.

During the anodizing processs at 25–45°C, typical anodizing behaviors were observed, i.e., the voltages increased gradually after passing through an overshoot in a short time (Fig. 5.1A). These overshoots signify the reorganization processes of the initial embryonic pores [2]. Notably, the overshoot is generally followed by a plateau voltage [27]. The increase rate in the voltage at 25°C reached ~2.5 V/min and was much higher than that at 35 and 45°C (Fig. 5.1A). Nevertheless, the resultant thickness of the Eti-film obtained at 25°C was not the thickest (~9 μm, Fig. 5.1B). The low porosity of the Eti-film (Fig. 5.2B1) caused by the low corrosion of the HEDP solution with a low temperature can be used to explain this phenomenon. By contrast, the increase in electrolyte temperature resulted in the increase in porosity of the Eti-films (Figs. 5.2C1 and D1); the corresponding voltages were therefore relatively low and stable. Moreover, serious corrosion marks were clearly observed on the Eti-film prepared at 45°C (Fig. 5.2D1).

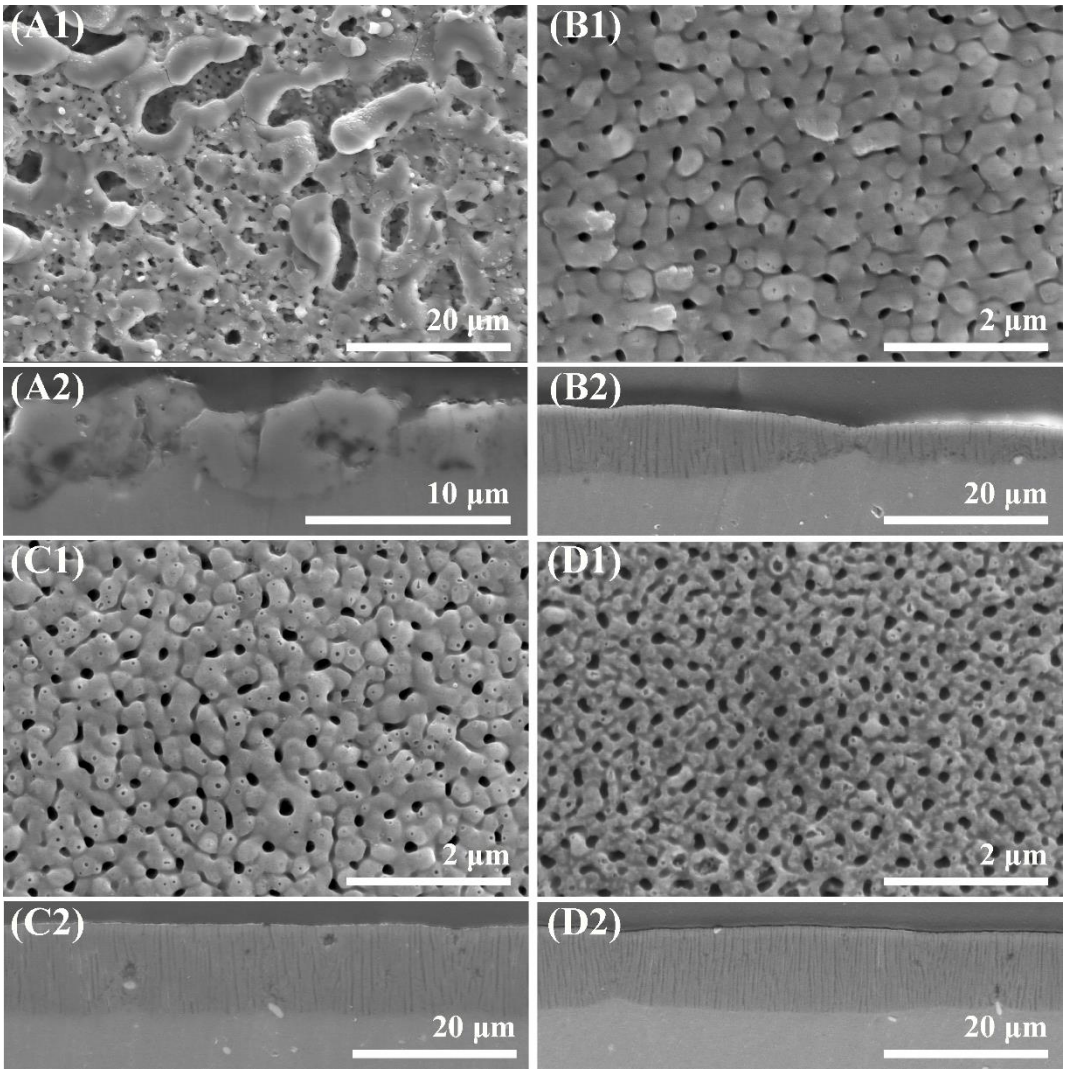

Fig. 5.2 Surface (A1, B1, C1 and D1) and cross-sectional (A2, B2, C2, and D2) morphologies of Eti-films fabricated in HEDP solution at 1 A/dm^2: (A) 15 °C; (B) 25 °C; (C) 35 °C; (D) 45 °C.

5.3.2 Electrochemical behaviors of anodizing just under the burning current

Anodizing processes powered by different current densities were then carried out (Fig. 5.3). It was seen that increasing the current caused more severe signal fluctuations during anodizing at 15°C. During the anodizing processs at 25 and 35°C, as the current density increases, the time required for the voltage overshoot decreases, and the voltage increases faster. Burnings of the Eti-films were observed at 3, 4, and 2 A/dm^2 for the 25, 35, and 45°C processes, respectively. Notably, the voltage curves suggest that the voltage “run

away" process caused by the burning was not completely out of control (Figs. 5.3B, C, and D). Moreover, when the voltage exceeded ~450 V, the rapid fluctuations of electrical signals and bursting sounds indicated the high-voltage breakdown of the Eti-film (25°C, Fig. 5.3B). Fig. 5.4D shows the appearances of burnt-free, burnt and breakdown samples. It can be seen that the burnt and breakdown areas exhibited a darker color than the burnt-free Eti-film.

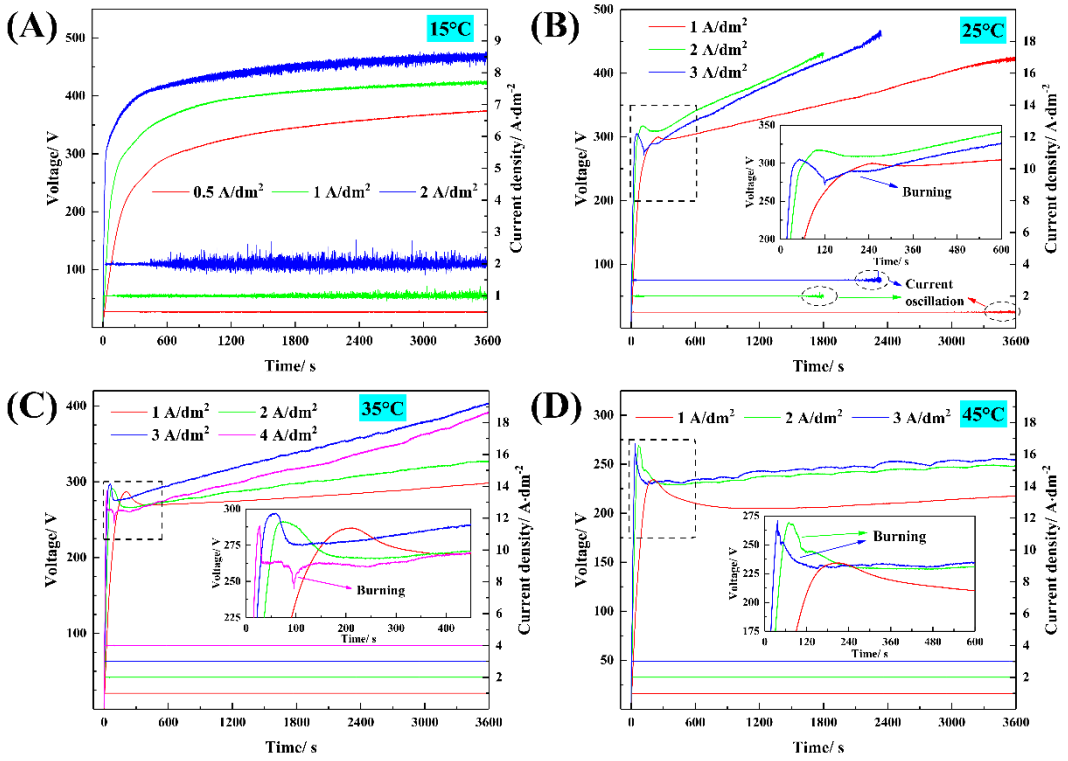

Fig. 5.3 Voltage-time curves of anodizing just under the burning current: (A) 15 °C; (B) 25 °C; (C) 35 °C; (D) 45 °C.

In general, for anodizing in conventional electrolytes (i.e., sulfuric, oxalic and phosphoric acids), the burning process refers to the localized accelerated dissolution of the anodic film, which is caused by the accumulated reaction heat [2, 30]; it manifests as a sharp decrease in the voltage in the galvanostatic mode. For the HEDP anodizing, the extremely high anodizing voltage undoubtedly causes a great amount heat, which is enough to arouse the candoluminescence (2 A/dm^2 at 35°C, Figs. 5.4A and B). Nevertheless, the reaction heat does not seem to be the main reason for the burning of the

Eti-film.

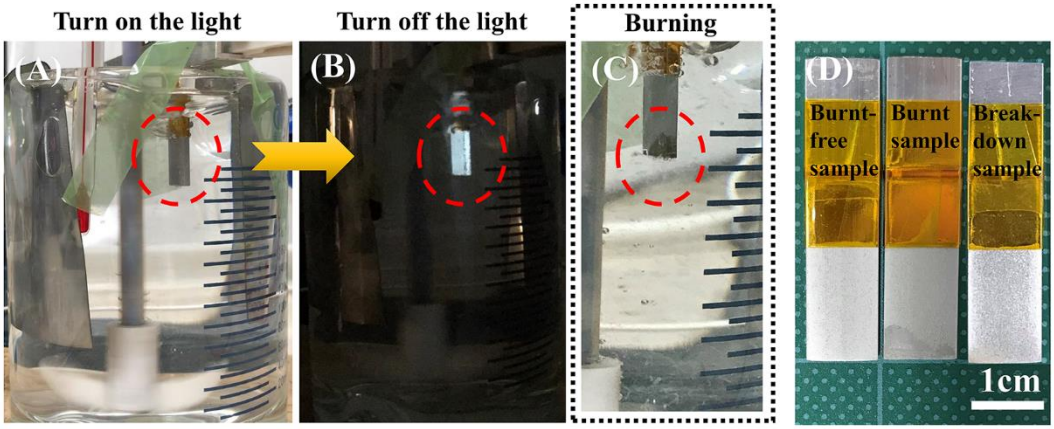

Fig. 5.4 Images of anodizing process and the resultant Eti-films. (A and B) Anodizing at 2 A/dm^2, 35°C; (C) Burning of Eti-film at 4 A/dm^2, 35°C; (D) The resultant Eti-films.

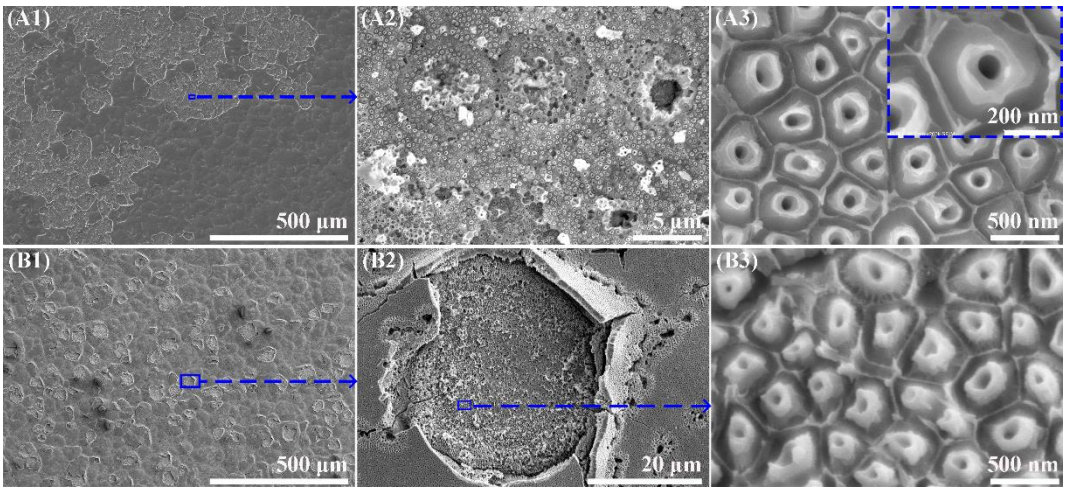

Fig. 5.5 (A1–A3) Burnt areas of Eti-film prepared at 35 °C (4 A/dm^2 for 1 h); (B1–B3) Electrical breakdown areas of Eti-film prepared at 25 °C (2 A/dm^2 for 30 min).

Fig. 5.5 reveals the surface morphologies of the burnt and breakdown areas of the Eti-films. Clearly, the burnt area shows a continuous film loss, contrasting with a dispersive film loss in the electrical breakdown area. Notably, only the outer porous layers of the Eti-films were stripped, whereas the barrier layers of the Eti-films still remain on the surface of the aluminum (Figs. 5.5A3 and B3).

It is generally known that most of the anodizing voltage appears across the barrier layer; thus, the circuit voltage would not significantly decrease as the burning or breakdown happens (Fig. 5.3). Actually, bulging and cracking were observed instead of dissolution

on the burnt area of the Eti-film surface [27, 33], which can be attributed to the volume expansion during alumina formation [34, 35]. Therefore, the large internal stress in the Eti-film with a low porosity should be the reason for the blockage of the high-growth process in the early stage of anodizing. On the other hand, it is difficult to completely avoid the high-voltage breakdown of Eti-film during the late stage of anodizing. Overall, increasing the temperature can increase the electrolyte's corrosion of the Eti-film, which not only releases part of the internal stress of the Eti-film but also results in larger nano pores and a thinner barrier layer. Therefore, the possibility of an electrical breakdown of the generated bubbles in the porous layer would be reduced during the late stage of anodizing (Fig. 5.3).

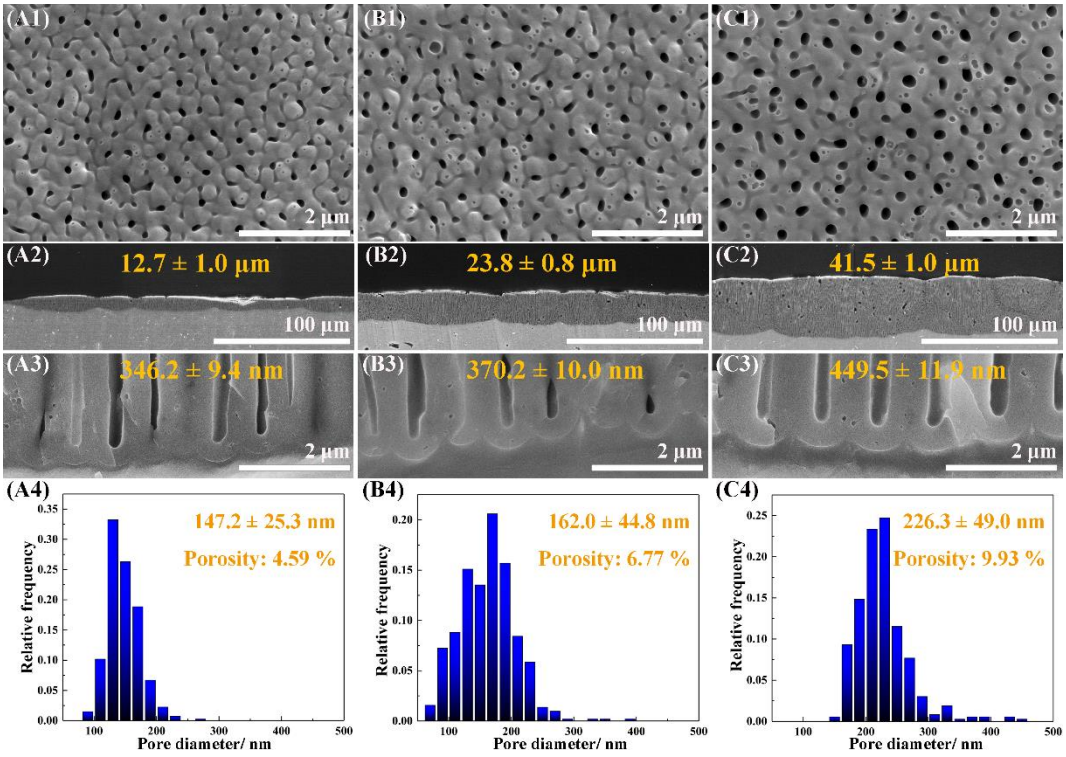

Fig. 5.6 Eti-films prepared at 1 A/dm^2 (A1–A4), 2 A/dm^2 (B1–B4), and 3 A/dm^2 (C1–C4) in 35 °C HEDP solution for 1 h. (A1, B1, and C1) Surface morphologies; (A2, B2, and C2) Cross-sectional morphologies; (A3, B3, and C3) Barrier layers; (A4, B4, and C4) Distributions of pore diameter of Eti-films.

Fig. 5.6 presents the morphologies of the Eti-films prepared at 35ºC. The pore diameter, porosity, and film thickness as well as the barrier layer thickness clearly increase with the

current density. Nevertheless, the porosity of the Eti-film prepared at 3 A/dm^2 is still as low as 9.9%. The growth rate of the Eti-film prepared at 3 A/dm^2 is ~0.69 μm/min, and the thickness of barrier layer is as high as ~450 nm (Figs. 5.6C2 and C3). Thus, this Eti-film is expected to retain excellent wear and corrosion resistances. Moreover, the large pores (~200 nm in diameter) in the Eti-film can allow a much larger filler to enter than in the Sul-film (~20 nm in diameter, Fig. 2.3); thus, its application is expected to be expanded.

5.3.3 HEDP hard anodizing

To suppress the burning of the Eti-film during anodizing with a high current density, the HEDP anodizing was first conducted at a relatively low current density (2 A/dm^2) for 300 s and was subsequently increased to the target values (5, 10, and 15 A/dm^2) at a rate of 1.3 A/dm^2·min (Fig. 5.7A). It was seen that 300 s is enough time to form the initial embryos of the Eti-films (reflected as the voltage overshoot), and the initial Eti-films are sufficient to resist the subsequent current increase processes. During the current increase processe, the voltages rise slowly over a small range. After reaching the target current densities, the voltages start to rise at different rates. Considering the high electrical breakdown of the Eti-film, the anodizing was stopped when the voltage reached ~460 V. Fig. 5.7B shows the images of obtained the Eti-films; it can be seen that the color of the Eti-film changes from off-white to brown as the current density increases.

Fig. 5.8 shows the morphologies of the Eti-films fabricated by the hard anodizing in Fig. 5.7. Reticular grain boundaries with a certain depth were observed on the surface of the Eti-films (Figs. 5.8A1, B1 and C1) and can be attributed to the poor corrosion resistance of the grain boundaries of 6063T5 substrate [36]. Moreover, many micron-level holes were observed on the surface and cross-section of the Eti-film. The alloying elements of 6063 aluminum alloy are primarily Mg, Si, and Fe in the forms of Mg_2Si and AlSiFe [37]; the electrode potentials of these second phases are more negative than that of the aluminum matrix. During anodizing, the Mg_2Si and AlSiFe phases dissolve into

the HEDP solution; thus, holes appear on the Eti-film. The same phenomenon was observed on hard-anodized Sul-film (Fig. 2.3A).

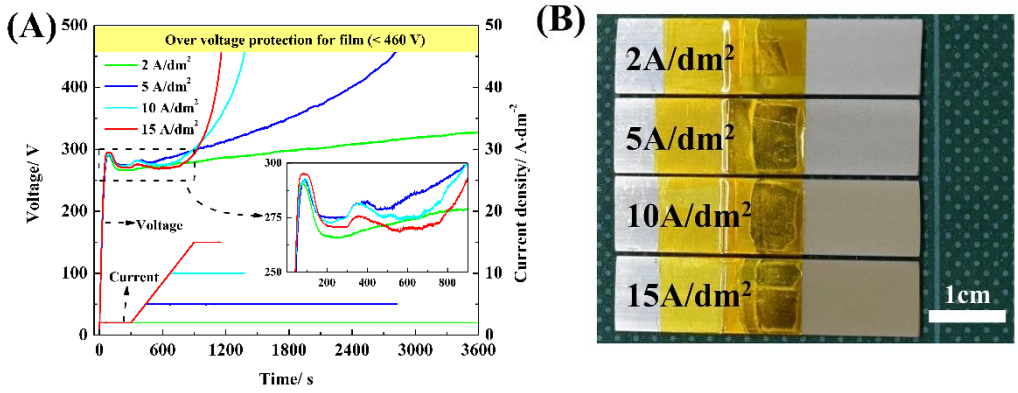

Fig. 5.7 Anodizing via gradient-increase-current approach: (A) Electrical signal curves; (B) Images of the obtained Eti-films.

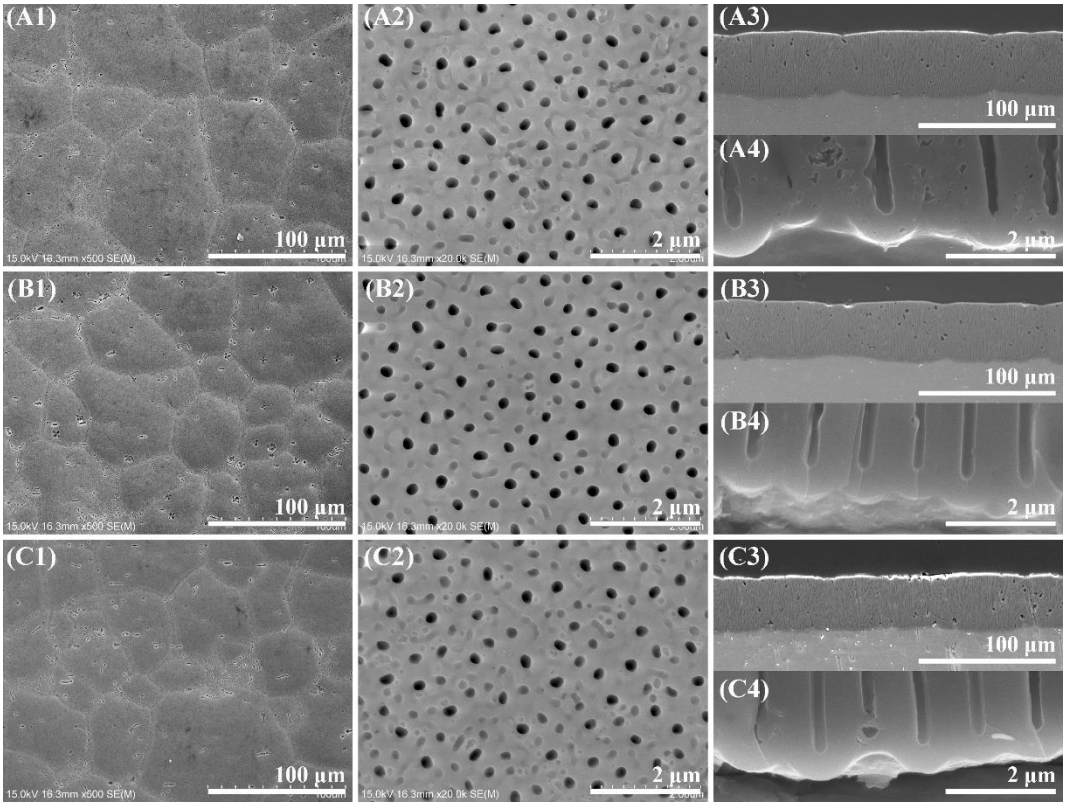

Fig. 5.8 Morphologies of Eti-films prepared via HEDP hard anodizing. (A1–A4) 5 A/dm^2; (B1–B4) 10 A/dm^2; (C1–C4) 15 A/dm^2; (A1, B1, and C1) Surface morphologies with a low magnification; (A2, B2, and C2) Surface morphologies with a high magnification; (A3, B3, and C3) Cross-sectional morphologies; (A4, B4, and C4) Barrier layers.

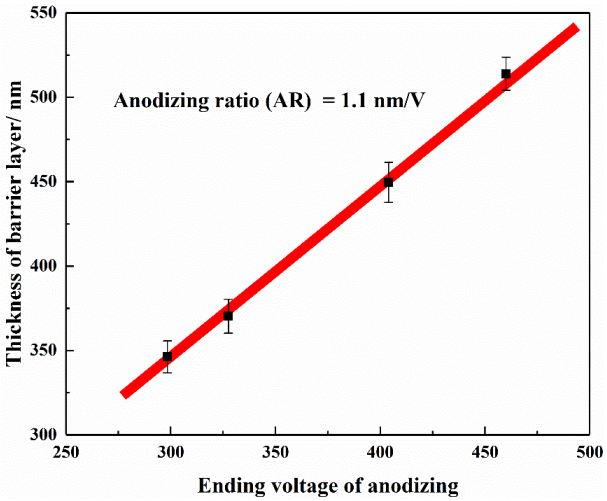

Fig. 5.9 Anodizing ratio of Eti-film prepared at 35°C.

Notably, the porosities and pore diameters of the hard-anodized Eti-films prepared at 5, 10, and 15 A/dm^2 are nearly the same (Table 5.2), ~9% and ~220 nm, respectively. These surface pore structures were greatly influenced by the initial anodizing process, i.e., 2 A/dm^2 for 300 s. For the Eti-film prepared at 2 A/dm^2 (Fig. 5.6B), a porosity of 6.67% and pore diameter of ~160 nm were observed. Because of the higher current density, more reaction heat is generated, and the corrosion of the Eti-film is accelerated, resulting in the increased porosity. However, the porosities of the Eti-films are still lower than 10% due to the short time the Eti-films are exposured to HEDP. Moreover, the same barrier layer thicknesses (~510 nm, Table 5.2) can be attributed to the unified ending voltage of anodizing (460 V). In this work, Fig. 5.9 shows that the anodizing ratio of the Eti-film prepared in HEDP at 35°C is ~1.1 nm/V and is consistent with that in other acidic solutions [2, 38], which indicates the same growth kinetics as thoes of the hard-anodized Eti-film.

Interestingly, the thicknesses of the Eti-films prepared at 5, 10, and 15 A/dm^2 are almost the same (~40 μm, Table 5.2), which might be a coincidence caused by the different anodizing times (Fig. 5.7A). For the gradient anodizing at 15 A/dm^2, the average growth rate of the Eti-film reaches ~2.1 μm/min. Moreover, it was pointed out that an increase in temperature would lead to a higher efficiency of film formation [38]. Our results showed

that the formation efficiency of the Eti-film increased from 0.33 to 0.42 μm·cm^2/C with the increase of current density (Table 5.2, the charge was calculated by integrating the area of the curve of the current density vs time).

Table 5.2 Structural parameters, growth rates, and formation ratios of Eti-films prepared with hard anodizing until the voltage reached 460 V

Current density (A/dm^2)	Porosity (%)	Pore diameter (nm)	Film thickness (μm)	Barrier layer thickness (nm)	Average growth rate (μm/min)	Formation efficiency (μm·cm^2/C)
5	9.13	222.1 ± 28.7	42.5 ± 1.7	509.9 ± 10.9	0.9	0.33
10	9.36	217.3 ± 26.7	41.2 ± 1.7	513.8 ± 9.8	1.8	0.41
15	9.42	227.7 ± 32.9	41.6 ± 1.1	516.8 ± 13.0	2.1	0.42

5.3.4 Elemental composition and crystalline state of the hard anodized Eti-film

XPS spectra (Fig. 5.10) indicated that the main elements in the Eti-films are Al, O, C, and P. For the Al2p photoelectron region, the peaks at 74.9 eV and 74.1 eV are assigned as Al_2O_3 and AlOOH (or $Al(OH)_3$) [39], respectively. Notably, an increase in the area ratio of Al_2O_3/AlOOH (or $Al(OH)_3$) with the current density can be observed. It could be explained as the dehydration phenomenon of the film during anodizing at high temperatures (Fig. 5.4B). For the C1s photoelectron region, the peaks at 284.8 eV and 286.1 eV correspond to the bonds of C-C/C-H and C-O [18, 40], respectively. The C-O bond (Fig. 5.10B) can be attributed to the carbide deposition caused by the pyrolysis of HEDP, thus causing the color change in the Eti-films (Fig. 5.7B). It was also proven by the higher C content of Eti-15 (20.2 at%) than that of Eti-2 (7.5 at%). The EDS results (Fig. 5.11) indicated that the carbide deposition occurs only on the surface of the Eti-film, i.e., the interface between the high-temperature Eti-film and the low-temperature electrolyte during hard anodizing in HEDP.

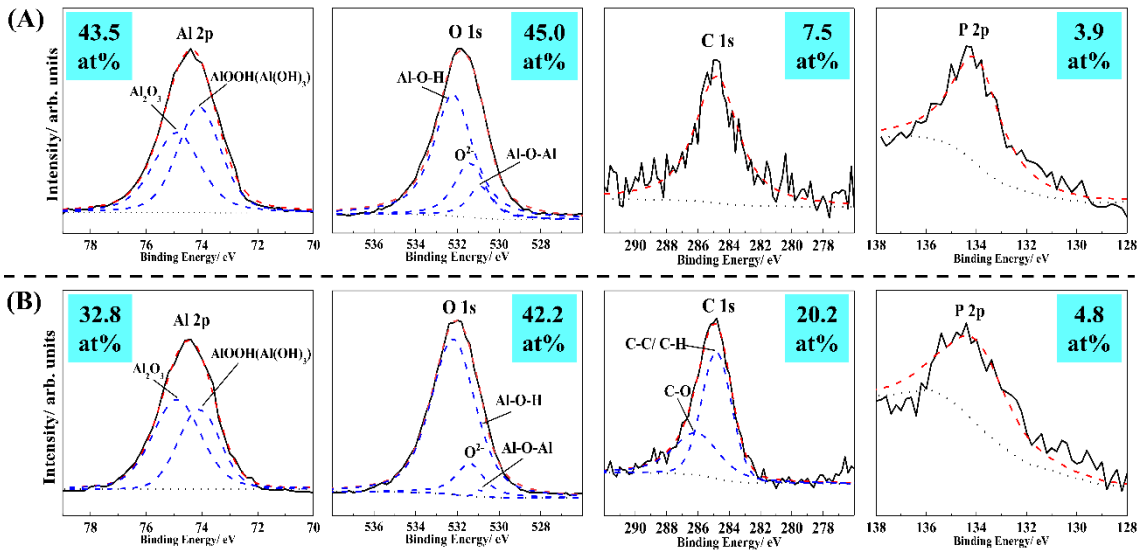

Fig. 5.10 XPS results of Eti-films prepared at (A) 2 A/dm^2, marked as Eti-2, and (B) 15 A/dm^2, marked as Eti-15.

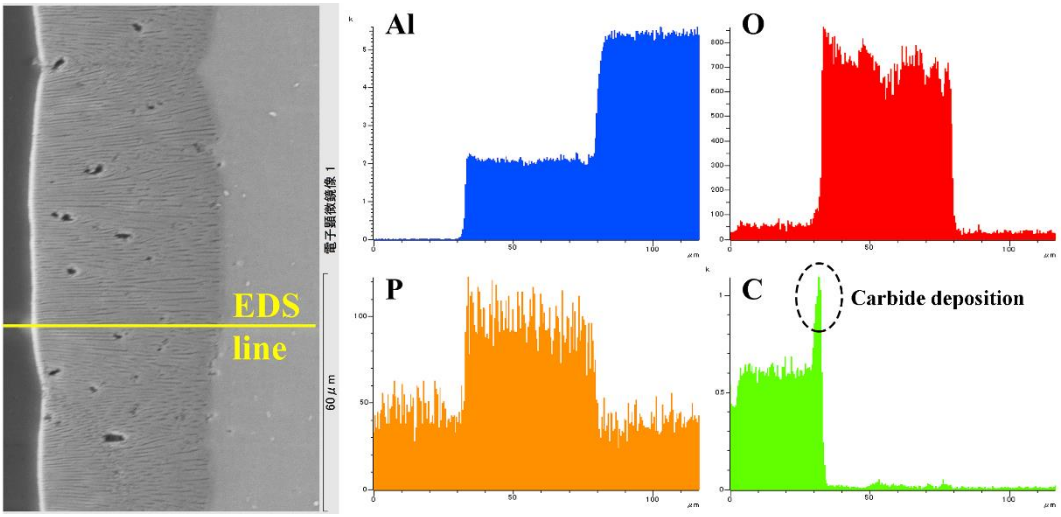

Fig. 5.11 EDS line analysis on Eti-film prepared at 15 A/dm^2.

Fig. 5.12 presents the XRD and SAED patterns of Eti-15. It is known that PAA film is amorphous, while Li et al. recently reported that crystallized PAA film can be fabricated under ultra-high anodizing voltage [41]. In this work, only the broad pattern (from 20–30°) of amorphous aluminum oxide and the diffraction peaks of aluminum substrate were observed (Fig. 5.12A), although the energy input used to prepare our PAA film is higher than that used in Li's work. Moreover, we still did not find crystal islands in the Eti-15 with the SAED analysis (Fig. 5.12B).

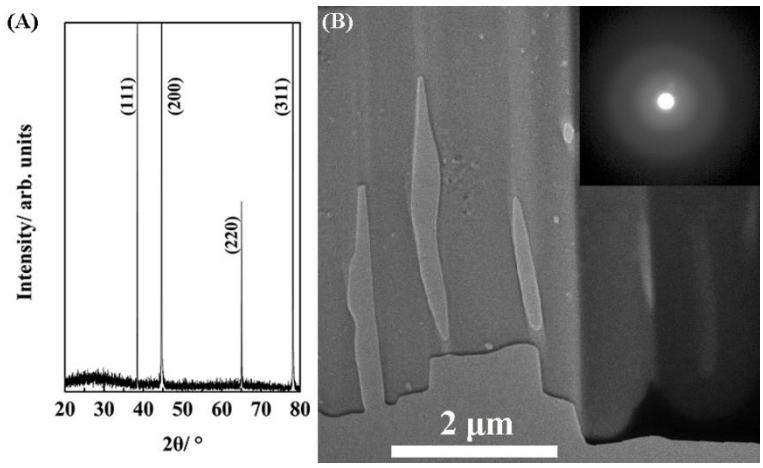

Fig. 5.12. Crystallization state of Eti-film prepared at 15 A/dm^2 (Eti-15). (A) XRD pattern; (B) TEM brightfield image with SAED pattern near the barrier layer.

5.3.5 Mechanical performance of the hard anodized Eti-film

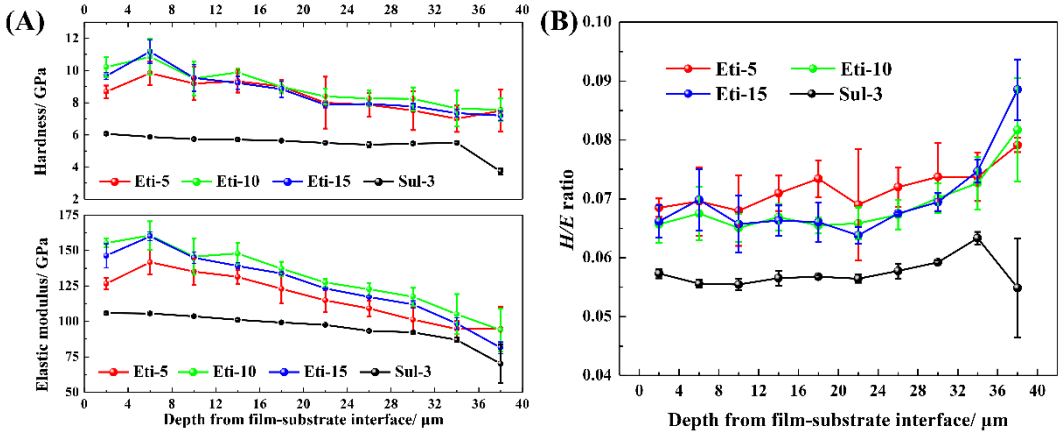

Fig. 5.13 Nanoindentation analysis of Eti-films and Sul-film at the load of 0.025 N: (A) Hardness and Elastic modulus; (B) H/E ratio.

Fig. 5.13 presents comparisons of the hardness and elastic modulus between the Eti-films and Sul-3. In addition, a comparison of the Vickers hardness was also conducted (Fig. 5.14). The results show that the hardness of Sul-3 for reference reached ~6 GPa (> 500 $HV_{0.01}$, Fig. 5.14), which is close to the highest value (~550 HV) of hard Sul-film reported in the literature [42-45]. Notably, the hardness of the Eti-films significantly exceeded this limit and reached 7–11 GPa (600–1000 $HV_{0.01}$, Fig. 5.14), which is harder than the porous layer of most MAO ceramic coatings [46, 47]. Moreover, the hardness increases gradually from the surface to the interior. The elastic modulus shows the same

trend as the hardness. However, the *H/E* ratio (Fig. 5.13B) shows the opposite trend, i.e., it decreases gradually from the surface to the interior. The highest *H/E* ratio of the Eti-films reached ~0.09, while that of Sul-3 was only ~0.06. It is generally believed that the high *H/E* ratio is often a reliable indicator of good wear resistance in a film [48].

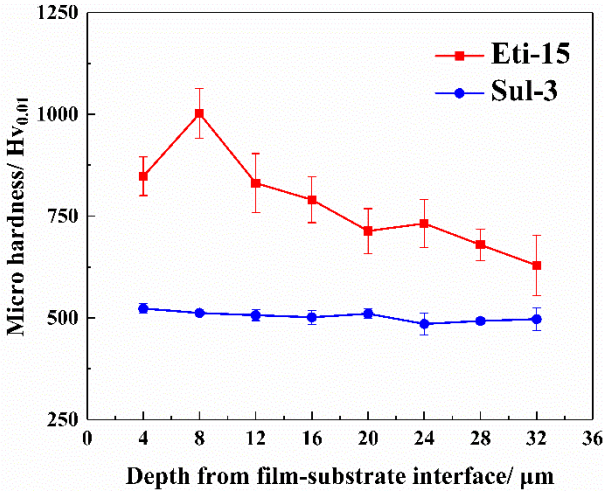

Fig. 5.14 Vickers hardness test results of Eti-15 and Sul-3 films

Such a high hardness value for the Eti-film can be mainly attributed to the dehydration phenomenon of Eti-films during anodizing at high temperatures (Fig. 5.10 and 5.4B). Kikuchi et al. [25] proved that subsequent thermal treatment of Eti-film causes dehydration and corresponding hardening. On the other hand, Table 5.2 lists the surface porosities of the Eti-films (~9%), which are much higher than that of the Sul-3 film (~6.6%, Fig. 2.3). In fact, the true porosities inside the Eti-films should be lower than their surface porosities. It should be noted that the sharp rise in anodizing voltage (Fig. 5.7A) caused the merger of the film cells at the film/substrate interface (Fig. 5.15A and B). Consequently, the Eti-film with branched nanoholes [49] was prepared (Fig. 5.15C). The decreasing porosity along the film thickness would also cause this kind of hardness distribution (Fig. 5.13A). Considering the above two factors, the result that the highest hardnesses of the Eti-films appear approximately 6 μm from the film/substrate interface is understandable.

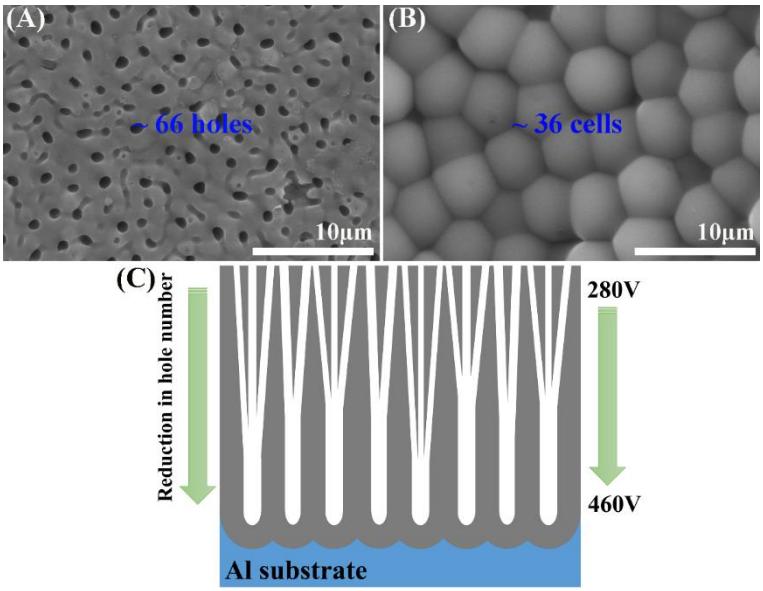

Fig. 5.15 (A) The surface morphology of Eti-15; (B) The bottom morphology of Eti-15; (C) The schematic diagram of film structure.

The comparison of wear resistance between the Eti-15 and Sul-3 films is illustrated in Fig. 5.16. After the run-in period, the friction coefficients of the Eti-15 and Sul-3 films were stable at ~0.7 and ~0.8, respectively, in contrast to the gradually increasing vertical displacement (Fig. 5.16A). The much higher vertical displacement of Eti-15 compared to that of Sul-3 can be attributed to the severe wear of the GCr15 steel ball (insert image in Fig. 5.16A) and was also proven by the cross-sectional profiles of the wear scars of the anodic films (Fig. 5.16B). Due to the high-speed growth of the Eti-15 film, it shows a rougher surface than that of the Sul-3 film. After sliding for 30 min, a groove with a width of ~1 mm and depth of ~5 μm was scratched on the Sul-3 film, while there was no significant change in the Eti-15 film except for the reduction in surface roughness around the sliding area. Fig. 5.17 shows the surface morphologies of the two wear scars, and the wear scar on the Sul-3 film was more obvious than that on the Eti-15 film. Moreover, it was found that many abrasive particles falling from the GCr15 steel balls remained on the surface of the Eti-15 film (Fig. 5.17A2). The EDS analysis of these abrasive particles indicated that their primary element is Fe. By comparison, few Fe was found on the wear scar of the Sul-3 film.

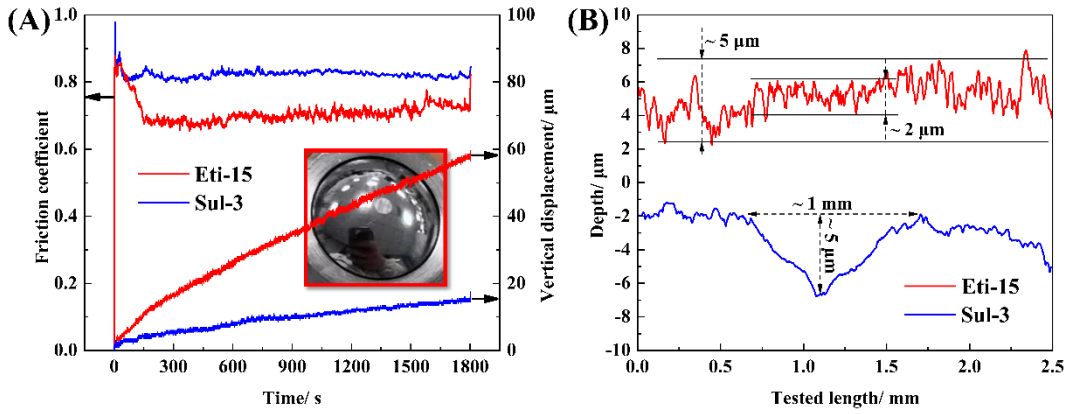

Fig. 5.16 (A) Friction coefficients and vertical displacements as functions of sliding time, the insert image shows the appearance of the GCr15 steel ball after testing Eti-15; (B) Cross-sectional profiles of wear scars.

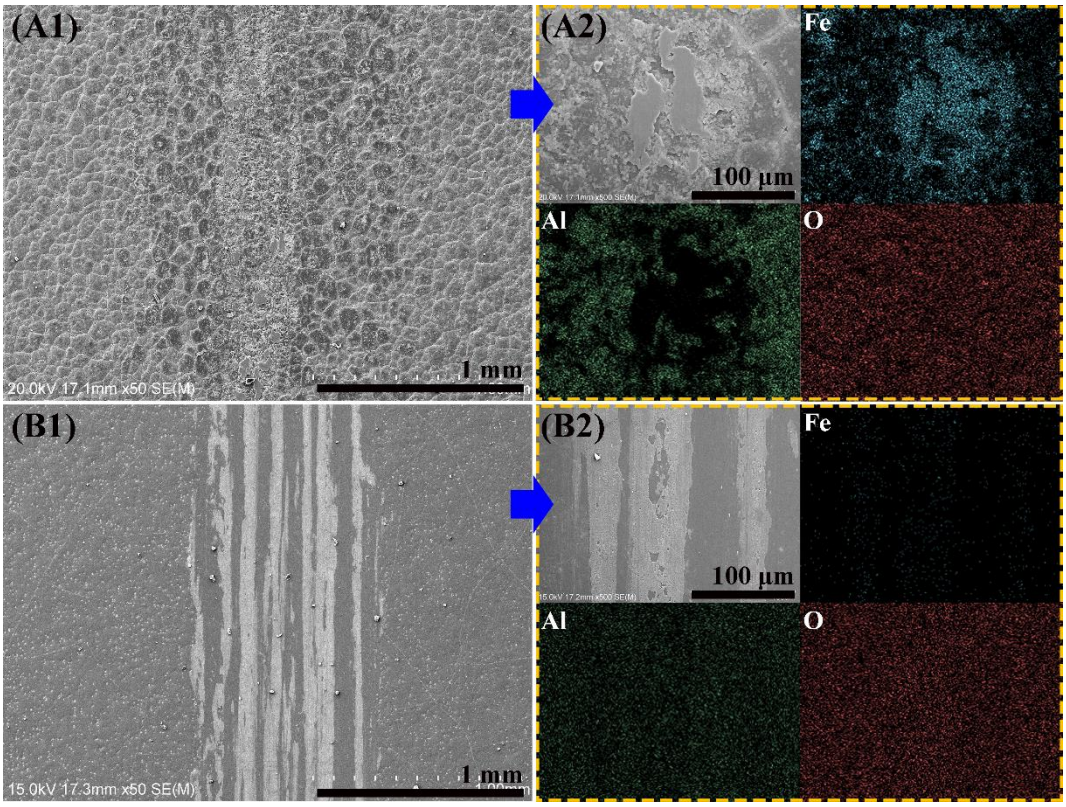

Fig. 5.17. Surface morphologies of the wear scars on (A1) Eti-15 and (B1) Sul-3 films; (A2) and (B2) are the corresponding EDS mapping results.

Overall, the wear resistance of the Eti-15 film is excellent as shown by the hardness test results (Fig. 5.13 and 5.14) and is significantly better than some MAO coatings tested under the same conditions [50-52]. Although MAO coatings are known for their high

hardness and wear resistance as compared with hard-anodized films, their loose outer layers and high energy consumption are the critical drawbacks that lead to limited applications.

5.3.6 Corrosion resistances of the hard anodized Eti-film

Fig. 5.18 depicts the polarization curves of the samples after the steady OCP values in 3.5 wt% NaCl were reached. The corrosion potential (E_{corr}) and corrosion current (i_{corr}) were obtained through Tafel fitting, and the polarization resistance (R_p) was calculated by R_p fitting, as listed in Table 5.3. It can be seen that both the E_{corr} and i_{corr} values decreased after the 6063T5 aluminum alloy was anodized. The anions that enter the anodic film from the solution cause a higher active stage; therefore, the E_{corr} of the anodic film is lower than that of the aluminum substrate, while the low i_{corr} can be attributed to the thin and dense barrier layer which provides the high R_p (Table 5.3). Because the thickness of the barrier layer of the Eti-15 film (~510 nm, Fig. 5.8 and Table 5.2) is nearly 10 times than that of the Sul-3 film, the Eti-15 film exhibited the lowest i_{corr} (10^{-10} A/cm^2), which was an order of magnitude lower than that of Sul-3 film and three orders of magnitude lower than that of the 6063T5 aluminum alloy.

EIS is widely used to evaluate the corrosion mechanism of anodic film [10]. Fig. 5.19 shows the EIS results of the Eti-15 and Sul-3 films immersed in 3.5 wt% NaCl for 14 d. It can be seen in the Nyquist plots (Fig. 5.19A and D) that the semicircle of the Eti-15 film was significantly larger than that of the Sul-3 film. Moreover, the radius of the Nyquist plots (the high frequency region) of both the Eti-15 and Sul-3 films first decrease and then increase with immersion time. In the low-frequency region of the Nyquist plots after the Eti-15 was immersed in NaCl solution for 2–5 d (Fig. 5.19A), the occurrence of a Warburg impedance might indicate an increase in the diffusion resistance of the ions in the porous layer. In the phase angles in the Bode plots of the Eti-15 and Sul-3 films (Figs. 5.19B and E, respectively), the phase angle of the Eti-15 film approached near -90° over a wide range indicating its high resistance and low capacitance, which are significantly

different from thoes of the Sul-3 film. On the other hand, the impedance Bode plots indicated the high impedance in |Z| of the Eti-15 film (Fig. 5.19C) at low frequency, which was at least an order of magnitude higher than that of the Sul-3 film (Fig. 5.19E).

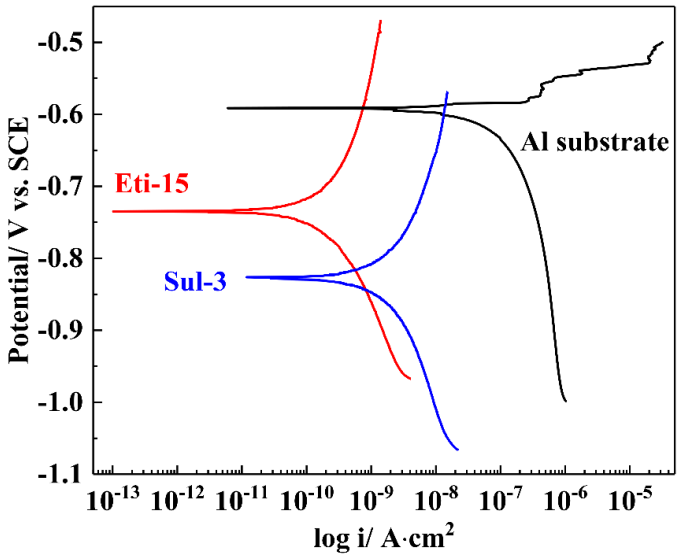

Fig. 5.18 Polarization curves of Eti-15 and Sul-3 films and 6063T5 aluminum alloy substrate exposed in 3.5 wt% NaCl.

Table 5.3 Electrochemical parameters of the polarization curves

	Eti-15	Sul-3	6063T5 aluminum alloy
E_{corr} (V_{SCE})	-0.735	-0.824	-0.591
i_{corr} (A/cm^2)	3.72×10^{-10}	3.80×10^{-9}	3.33×10^{-7}
R_p ($\Omega\cdot cm^2$)	1.71×10^{8}	1.98×10^{7}	8.34×10^{4}

Generally, two constant phase elements (CPE) are used to consider the nonideal capacitive values of anodic film [53]. To facilitate a comparison of all fitted data, the Warburg impedance is not considered in the fitting process. Thus, the equivalent circuit model (Fig. 5.19F) can be used to simulate the EIS results: $R_s(CPE_pR_p)(CPE_bR_b)$, where R_s is the solution resistance; CPE_p and CPE_b are the constant phase elements of the porous and barrier layers, respectively; and R_p and R_b are the charge transfer resistances of the porous and barrier layers, respectively. The impedance of CPE is determined as follows [54]:

$$Z_{CPE} = \frac{1}{Q(j\omega)^n} \quad [5.1]$$

where ω corresponds to the angular frequency (rad/s). When n = 0, the CPE is considered as a resistor, and when n = 1, the CPE can be simplified to a capacitor. Table 5.4 lists the fitting data. Furthermore, the capacitance of the CPE (C_b for CPE_b and C_p for CPE_p), takes the form:

$$C = Q^{1/n} R^{(1-n)/n} \qquad [5.2]$$

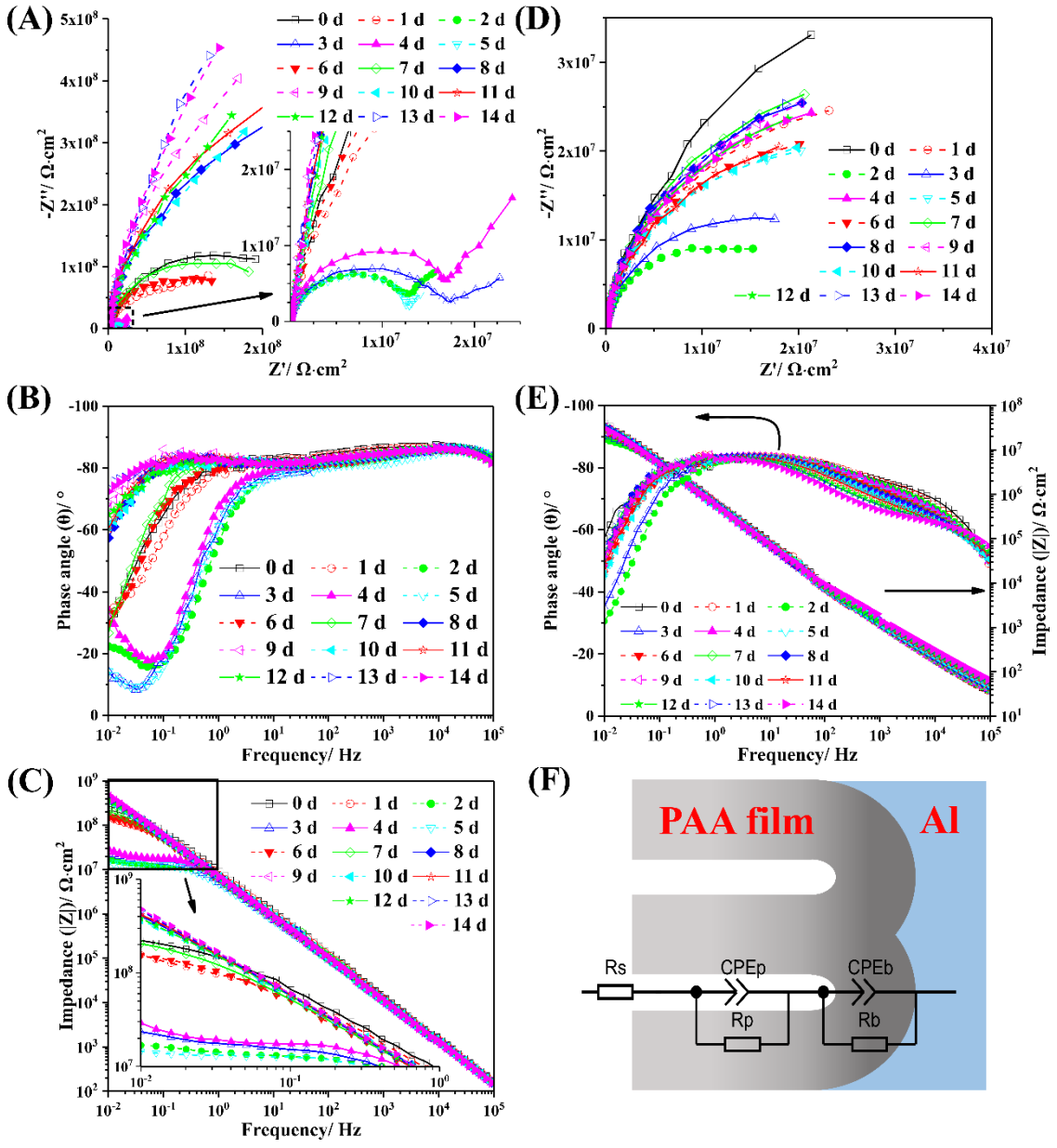

Fig. 5.19 EIS diagrams of Eti-15 (A, B and C) and Sul-3 (D and E) films exposed in 3.5 wt% NaCl for different time. (A and D) Nyquist plots; (B, C and E) Bode plots; (F) Equivalent circuits.

Table 5.4 Equivalent circuit parameters obtained from the impedance data fitting at different immersion times 3.5 wt.% NaCl. The *Rs* of Eti-film was artificially set as 10 $\Omega \cdot cm^2$ before fitting after referring to *Rs* of Sul-film.

Sample	Time (d)	R_s ($\Omega \cdot cm^2$)	CPE_p-Q (s-sec^n/cm^2)	CPE_p-n	R_p ($\Omega \cdot cm^2$)	CPE_b-Q (s-sec^n/cm^2)	CPE_b-n	R_b ($\Omega \cdot cm^2$)
	0	10	2.77E-08	0.95433	9.47E+06	1.10E-08	0.95448	2.52E+08
	1	10	9.14E-09	0.94223	6.65E+07	4.12E-08	0.94996	1.70E+08
	2	10	7.53E-09	0.93937	1.27E+07	2.69E-07	8.97E-01	2.38E+07
	3	10	6.73E-09	0.92404	1.56E+07	3.99E-07	0.93003	7.99E+06
	4	10	7.49E-09	0.93328	1.80E+07	2.95E-07	9.30E-01	6.69E+07
	5	10	6.44E-09	0.91662	1.32E+07	1.62E-06	9.30E-01	3.18E+07
	6	10	7.94E-09	0.92612	1.18E+08	5.78E-08	0.93056	1.61E+08
Eti-15	7	10	8.48E-08	0.97867	2.07E+05	8.84E-09	0.93788	2.34E+08
	8	10	1.01E-08	0.93472	5.03E+08	2.64E-08	0.91942	9.28E+08
	9	10	1.39E-08	0.92952	3.93E+08	1.60E-08	0.93123	1.62E+09
	10	10	1.19E-07	0.99746	9.16E+05	8.41E-09	0.93592	9.77E+08
	11	10	6.74E-08	0.9491	197310	9.22E-09	0.94257	1.07E+09
	12	10	4.14E-08	0.93106	1.00E+07	9.51E-09	0.9375	1.16E+09
	13	10	6.57E-08	0.94978	275360	9.54E-09	0.94386	1.94E+09
	14	10	6.72E-08	0.95051	319660	9.70E-09	0.94651	1.88E+09
	0	14.684	8.50E-06	0.67571	384.29	2.71E-07	0.92453	8.24E+07
	1	15.239	8.45E-06	0.67053	304.71	2.71E-07	0.93329	5.19E+07
	2	13.108	1.13E-05	0.63581	370.3	2.88E-07	9.27E-01	2.03E+07
	3	13.27	1.20E-05	0.62373	522.13	2.91E-07	0.93034	2.68E+07
	4	13.435	1.03E-05	0.63184	524.69	2.90E-07	0.93384	5.35E+07
	5	13.687	1.03E-05	0.62901	493.07	2.96E-07	0.92881	4.34E+07
	6	13.298	9.24E-06	0.62735	737.73	3.02E-07	0.93029	4.52E+07
Sul-3	7	12.634	9.00E-06	0.62195	882.18	2.91E-07	0.93257	6.11E+07
	8	12.456	8.58E-06	0.62121	998.33	3.00E-07	0.9321	5.86E+07
	9	12.66	7.58E-06	0.62689	890.55	3.00E-07	0.92976	5.86E+07
	10	13.1	7.44E-06	0.63	829.51	3.10E-07	0.93172	4.33E+07
	11	11.437	6.93E-06	0.62661	1043.4	3.22E-07	0.92967	4.46E+07
	12	11.821	4.86E-06	0.64352	924.22	3.13E-07	0.92543	5.55E+07
	13	9.2959	5.94E-06	0.61777	1752.6	3.13E-07	0.92609	6.15E+07
	14	10.012	5.11E-06	0.62547	3420.4	3.16E-07	0.92168	5.53E+07

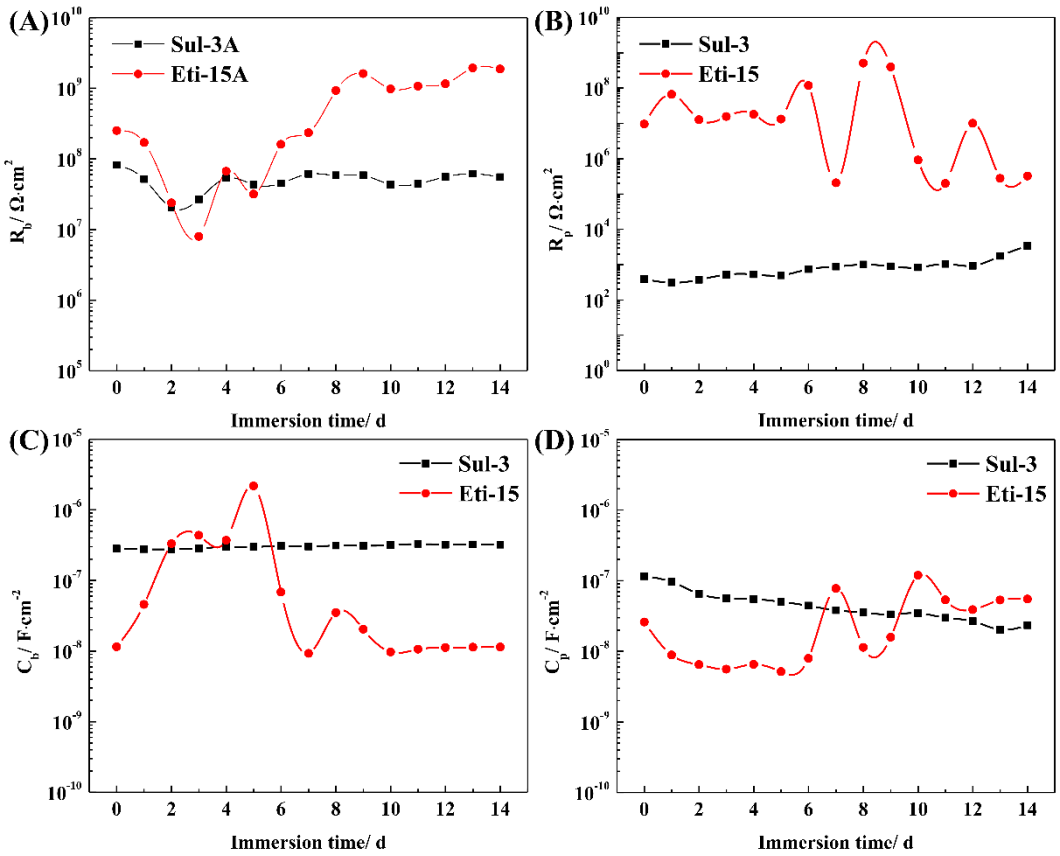

Fig. 5.20 Changes in R_b (A), R_p (B), C_b (C), and C_p (D) of anodic films with the immersion time in 3.5 wt% NaCl solution.

Fig. 5.20 presents the simulated values of the elements, i.e., R_b, R_p, C_b and C_p. In the early stage of immersion (2–5 days), a reduction in R_b and increase in C_b of the Eti-15 film were observed, meaning the erosion of the barrier layer from Cl^-. However, all simulated values of the Sul-3 film are relatively stable. Actually, the defects introduced in the Eti-15 film during the high-speed growth would also accelerate the erosion from Cl^-. With a prolonged immersion time, the R_b and C_b of the Eti-15 film start to stabilize, indicating the saturation of the Cl^- penetration. Moreover, the self-sealing phenomenon of Eti-film should also be considered. Fig. 5.10B proved that the less hydrated alumina in the Eti-15 film are due to high temperature anodizing. It should be pointed out that the anhydrous alumina react with absorbed water, and then the volume expansion of the anodic film caused the self-sealing phenomenon [53]. Moreover, the branched nanoholes structure (Fig. 5.15) also impedes the penetration of electrolytes into the Eti-

film, thus causing the high R_p value. In general, such a thick barrier layer in the Eti-15 film dominated the excellent corrosion resistance, which is much higher than that of Sul-3 film.

5.4 Conclusions

Based on the experimental investigations and analysis regarding HEDP anodizing of 6063T5 aluminum alloy, the following conclusions may be drawn:

1. Low-temperature anodizing (≤ 15°C) tends to arouse the MAO regime and coatings; high-temperature anodizing (≥ 45°C) causes the HEDP electrolyte to excessively corrode the Eti-film. The appropriate temperature for the fabrication of Eti-film is ~35°C according to the film microstructures and electrochemical curves.

2. Burning of the Eti-film is caused by stress accumulation instead of chemical dissolution caused by the reaction heat; the gradient-increase-current approach can efficiently inhibit the burning of the Eti-film, thus realizing the HEDP hard-anodizing process; the growth rate of the hard-anodized Eti-film can reach ~2.1 μm/min.

3. The hard-anodized Eti-films were prepared with the pore diameter, surface porosity, and barrier layer thickness of ~220 nm, ~9%, and ~510 nm, respectively; anodizing at a high current density generates a large amount of reaction heat and eventually leads to the dehydration of the Eti-film; the rapid rise of the anodizing voltage in a short time causes the branched nanopore structure of the Eti-film.

4. Ample evidence shows that the hardness of the hard-anodized Eti-film can reach up to ~11 GPa (~1000 $HV_{0.01}$), which greatly exceeds that of the widely used hard-anodized Sul-film; a lower friction coefficient (~0.7) and slighter wear are found on hard-anodized Eti-film than on Sul-film; the corrosion resistance of the hard-anodized Eti-film is 10 times higher than that of Sul-film due to its thick barrier layer and the branched nanopore structure.

References

[1] H. Masuda, K. Fukuda, Ordered Metal Nanohole Arrays Made by a Two-Step Replication of Honeycomb Structures of Anodic Alumina, Science, 268 (1995) 1466-1468.

[2] W. Lee, S.-J. Park, Porous Anodic Aluminum Oxide: Anodizing and Templated Synthesis of Functional Nanostructures, Chemical Reviews, 114 (2014) 7487-7556.

[3] I.V. Roslyakov, E.O. Gordeeva, K.S. Napolskii, Role of Electrode Reaction Kinetics in Self-Ordering of Porous Anodic Alumina, Electrochimica Acta, 241 (2017) 362-369.

[4] K. Kawahara, T. Kikuchi, S. Natsui, R.O. Suzuki, Fabrication of ordered submicrometer-scale convex lens array via nanoimprint lithography using an anodized aluminum mold, Microelectronic Engineering, 185-186 (2018) 61-68.

[5] L.B. Huang, W. Xu, J. Hao, Energy Device Applications of Synthesized 1D Polymer Nanomaterials, Small, 13 (2017) 1701820.

[6] Q. Xu, G. Meng, F. Han, Porous AAO template-assisted rational synthesis of large-scale 1D hybrid and hierarchically branched nanoarchitectures, Progress in Materials Science, 95 (2018) 243-285.

[7] G.D. Bengough, J.M. Stuart, Improved process of protecting surfaces of aluminium or aluminium alloys, GB Patent 223994, 1923.

[8] R.K. Choudhary, P. Mishra, V. Kain, K. Singh, S. Kumar, J.K. Chakravartty, Scratch behavior of aluminum anodized in oxalic acid: Effect of anodizing potential, Surface and Coatings Technology, 283 (2015) 135-147.

[9] Y. Wu, W. Zhao, W. Wang, Y. Zhang, Q. Xue, Novel structured anodic oxide films containing surface layers and porous sublayers showing excellent wear resistance performance, RSC Advances, 6 (2016) 94074-94084.

[10] Y. Huang, H. Shih, H. Huang, J. Daugherty, S. Wu, S. Ramanathan, C. Chang, F. Mansfeld, Evaluation of the corrosion resistance of anodized aluminum 6061 using

electrochemical impedance spectroscopy (EIS), Corrosion Science, 50 (2008) 3569-3575.

[11] S.-J. Lee, S.-J. Kim, Essential anti-corrosive behavior of anodized Al alloy by applied current density, Applied Surface Science, 481 (2019) 637-641.

[12] S. Lee, D. Kim, Y. Kim, U. Jung, W. Chung, Effect of aluminum anodizing in phosphoric acid electrolyte on adhesion strength and thermal performance, Metals and Materials International, 22 (2016) 20-25.

[13] M. González-Castaño, C. Cancellieri, X. Maeder, E. Hack, P. Schmutz, Enhancing the insulating and dielectric properties of barrier anodic Al_2O_3 on high purity aluminum, Applied Surface Science, 505 (2019) 144522.

[14] Y. Suzuki, K. Kawahara, T. Kikuchi, R.O. Suzuki, S. Natsui, Corrosion-Resistant Porous Alumina Formed via Anodizing Aluminum in Etidronic Acid and Its Pore-Sealing Behavior in Boiling Water, Journal of The Electrochemical Society, 166 (2019) C261-C269.

[15] D. Elabar, G.R. La Monica, M. Santamaria, F. Di Quarto, P. Skeldon, G.E. Thompson, Anodizing of aluminium and AA 2024-T3 alloy in chromic acid: Effects of sulphate on film growth, Surface and Coatings Technology, 309 (2017) 480-489.

[16] M. Pashchanka, J.J. Schneider, Self-Ordering Regimes of Porous Anodic Alumina Layers Formed in Highly Diluted Sulfuric Acid Electrolytes, The Journal of Physical Chemistry C, 120 (2016) 14590-14596.

[17] Y. Li, Y. Qin, S. Jin, X. Hu, Z. Ling, Q. Liu, J. Liao, C. Chen, Y. Shen, L. Jin, A new self-ordering regime for fast production of long-range ordered porous anodic aluminum oxide films, Electrochimica Acta, 178 (2015) 11-17.

[18] Y. Ma, Y. Wen, J. Li, J. Lu, Y. Li, Y. Yang, C. Feng, C. Hao, Z. Zhang, J. Hu, R. Sun, Pore Nucleation Mechanism of Self-Ordered Alumina with Large Period in Stable Anodizing in Citric Acid, Journal of The Electrochemical Society, 165 (2018) E311-E317.

[19] Y. Nazarkina, K. Kamnev, A. Dronov, A. Dudin, A. Pavlov, S. Gavrilov, Features of

Porous Anodic Alumina Growth in Galvanostatic Regime in Selenic Acid Based Electrolyte, Electrochimica Acta, 231 (2017) 327-335.

[20] B. Sun, J. Li, X. Jin, C. Zhou, Q. Hao, X. Gao, Self-ordered hard anodizing in malonic acid and its application in tailoring alumina taper-nanopores with continuously tunable periods in the range of 290–490nm, Electrochimica Acta, 112 (2013) 327-332.

[21] A.l.o.o.p. R.Gabe, Hard anodizing—What do we mean by hard?, Metal finishing, 100 (2002) 52-58.

[22] W. Lee, R. Ji, U. Gosele, K. Nielsch, Fast fabrication of long-range ordered porous alumina membranes by hard anodizing, Nature Materials, 5 (2006) 741-747.

[23] T. Kikuchi, O. Nishinaga, S. Natsui, R.O. Suzuki, Fabrication of Self-Ordered Porous Alumina via Etidronic Acid Anodizing and Structural Color Generation from Submicrometer-Scale Dimple Array, Electrochimica Acta, 156 (2015) 235-243.

[24] A. Takenaga, T. Kikuchi, S. Natsui, R.O. Suzuki, Exploration for the Self-ordering of Porous Alumina Fabricated via Anodizing in Etidronic Acid, Electrochimica Acta, 211 (2016) 515-523.

[25] T. Kikuchi, A. Takenaga, S. Natsui, R.O. Suzuki, Advanced hard anodic alumina coatings via etidronic acid anodizing, Surface and Coatings Technology, 326 (2017) 72-78.

[26] M. Sepúlveda, J.G. Castaño, F. Echeverría, Influence of temperature and time on the fabrication of self-ordering porous alumina by anodizing in etidronic acid, Applied Surface Science, 454 (2018) 210-217.

[27] M. Iwai, T. Kikuchi, R.O. Suzuki, S. Natsui, Electrochemical and morphological characterization of porous alumina formed by galvanostatic anodizing in etidronic acid, Electrochimica Acta, 320 (2019) 134606.

[28] X.F. Zhu, Y. Song, L. Liu, C.Y. Wang, J. Zheng, H.B. Jia, X.L. Wang, Electronic currents and the formation of nanopores in porous anodic alumina, Nanotechnology, 20 (2009) 475303.

[29] B. Chong, D. Yu, R. Jin, Y. Wang, D. Li, Y. Song, M. Gao, X. Zhu, Theoretical derivation of anodizing current and comparison between fitted curves and measured curves under different conditions, Nanotechnology, 26 (2015) 145603.

[30] C. Lämmel, M. Schneider, C. Heubner, W. Beckert, A. Michaelis, Investigations of burning phenomena during the hard anodising of aluminium by local in-operando temperature measurements, Electrochimica Acta, 249 (2017) 271-277.

[31] B. Gastón-García, E. García-Lecina, J.A. Díez, M. Belenguer, C. Müller, Local Burning Phenomena in Sulfuric Acid Anodizing: Analysis of Porous Anodic Alumina Layers on AA1050, Electrochemical and Solid-State Letters, 13 (2010) C33-C35.

[32] H. Huang, J. Qiu, M. Sun, W. Liu, X. Wei, E. Sakai, K. Ito, A hard coating with MAO/AAO double layers prepared on aluminum in etidronic acid by DC oxidation, Surface and Coatings Technology, 360 (2019) 307-317.

[33] H. Huang, J. Qiu, M. Sun, W. Liu, X. Wei, Morphological evolution and burning behavior of oxide coating fabricated on aluminum immersed in etidronic acid at high current density, Surface and Coatings Technology, 374 (2019) 83-94.

[34] K. Nielsch, J. Choi, K. Schwirn, R.B. Wehrspohn, U. Gosele, Self-ordering Regimes of Porous Alumina: The 10% Porosity Rule, Nano Letters, 2 (2002) 677-680.

[35] C. Xu, W. Gao, Pilling-Bedworth ratio for oxidation of alloys, Materials Research Innovations, 3 (2000) 231-235.

[36] Y. Ma, X. Zhou, G.E. Thompson, J.O. Nilsson, M. Gustavsson, A. Crispin, Anodizing of AA6063 aluminium alloy profiles: Generation of dark appearance, Surface and Interface Analysis, 45 (2013) 1479-1484.

[37] L. Hu, D. Chen, F. Shi, S. Chen, Effect of AlSiFe on the anodizing process of 6063 aluminum, Surface and Interface Analysis, 48 (2016) 1299-1304.

[38] G.D. Sulka, W.J. Stępniowski, Structural features of self-organized nanopore arrays formed by anodizing of aluminum in oxalic acid at relatively high temperatures, Electrochimica Acta, 54 (2009) 3683-3691.

[39] Y. Yang, J. Cheng, S. Liu, H. Wang, P. Dong, Effect of $NaAlO_2$ sealing on corrosion

resistance of 2024 aluminum alloy anodized film, Materials and Corrosion, 70 (2019) 120-127.

[40] F. Gao, P.M.A. Sherwood, Photoelectron spectroscopic studies of the formation of hydroxyapatite films on titanium pretreated with etidronic acid, Surface and Interface Analysis, 45 (2013) 742-750.

[41] S. Li, Y. Li, S. Jin, J. Wu, Z. Li, X. Hu, Z. Ling, Fabrication of Crystallized Porous Anodic Aluminum Oxide under Ultra-High Anodizing Voltage, Journal of The Electrochemical Society, 165 (2018) E623-E627.

[42] L. Vojkuvka, A. Santos, J. Pallarès, J. Ferré-Borrull, L.F. Marsal, J.P. Celis, On the mechanical properties of nanoporous anodized alumina by nanoindentation and sliding tests, Surface and Coatings Technology, 206 (2012) 2115-2124.

[43] M. Bononi, R. Giovanardi, A. Bozza, Pulsed current hard anodizing of heat treated aluminum alloys: Frequency and current amplitude influence, Surface and Coatings Technology, 307 (2016) 861-870.

[44] A. Bozza, R. Giovanardi, T. Manfredini, P. Mattioli, Pulsed current effect on hard anodizing process of 7075-T6 aluminium alloy, Surface and Coatings Technology, 270 (2015) 139-144.

[45] L.R. Krishna, A.S. Purnima, G. Sundararajan, A comparative study of tribological behavior of microarc oxidation and hard-anodized coatings, Wear, 261 (2006) 1095-1101.

[46] H. Huang, X. Wei, J. Yang, J. Wang, Influence of surface micro grooving pretreatment on MAO process of aluminum alloy, Applied Surface Science, 389 (2016) 1175-1181.

[47] X. Wei, H. Huang, M. Sun, W. Liu, J. Qiu, Effects of honeycomb pretreatment on MAO coating fabricated on aluminum, Surface and Coatings Technology, 363 (2019) 265-272.

[48] A. Leyland, A. Matthews, On the significance of the H/E ratio in wear control: a nanocomposite coating approach to optimised tribological behaviour, Wear 246

(2000) 1-11.

[49] G. Meng, Y.J. Jung, A. Cao, R. Vajtai, P.M. Ajayan, Controlled fabrication of hierarchically branched nanopores, nanotubes, and nanowires, Proceedings of the National Academy of Sciences of the United States of America, 102 (2005) 7074-7078.

[50] Y.-l. Cheng, Z.-g. Xue, Q. Wang, X.-Q. Wu, E. Matykina, P. Skeldon, G.E. Thompson, New findings on properties of plasma electrolytic oxidation coatings from study of an Al–Cu–Li alloy, Electrochimica Acta, 107 (2013) 358-378.

[51] Y. Cheng, F. Wu, J. Dong, X. Wu, Z. Xue, E. Matykina, P. Skeldon, G.E. Thompson, Comparison of plasma electrolytic oxidation of zirconium alloy in silicate- and aluminate-based electrolytes and wear properties of the resulting coatings, Electrochimica Acta, 85 (2012) 25-32.

[52] Y. Cheng, J. Cao, Z. Peng, Q. Wang, E. Matykina, P. Skeldon, G.E. Thompson, Wear-resistant coatings formed on Zircaloy-2 by plasma electrolytic oxidation in sodium aluminate electrolytes, Electrochimica Acta, 116 (2014) 453-466.

[53] L. Bouchama, N. Azzouz, N. Boukmouche, J.P. Chopart, A.L. Daltin, Y. Bouznit, Enhancing aluminum corrosion resistance by two-step anodizing process, Surface and Coatings Technology, 235 (2013) 676-684.

[54] S.P. Harrington, T.M. Devine, Relation Between the Semiconducting Properties of a Passive Film and Reduction Reaction Rates, Journal of The Electrochemical Society, 156 (2009) C154-C159.

Chapter 6 Conclusions

6.1 General conclusions and remarks

HEDP is an environmentally friendly chelating agent and is recently proposed as an anodizing electrolyte. Comparing with other organic acid of anodizing, HEDP anodizing is more stable and the risk of burning phenomenon is lower. Moreover, high anodizing voltage and low corrosivity of HEDP give the resultant anodized film a thick barrier layer and low porosity, which is expected to provide anti-wear and anti-corrosion protection for aluminum alloys. However, the low growth rate of HEDP anodized film cannot meet industrial production requirements. In order to rapidly fabricate HEDP anodized film, the HEDP anodizing was conducted at under high current density and the growth and performance of the resultant film were systematically investigated in this thesis. The main conclusions are as follows.

In chapter 3, when anodizing in HEDP solution at a relatively low temperature, the anodized film would not be burnt down until the current density increased up to 8 A/dm^2, and a steady sparking was observed when the current density was higher than 4 A/dm^2. The obtained oxide coating had both the outer volcanic resolidified pool structure and inner honeycomb structure, i.e., a MAO/AAO composite coating. The estimated growth rate of oxide coating increased from 1 to 36 μm/h with the increase of current densities from 1 to 7 A/dm^2. The hardness of inner AAO layer was about 6–8 GPa, which was in contrast with the highest hardness (26.57 GPa) of the outer MAO layer.

In chapter 4, the growth mechanisms of MAO/AAO coating found were systematically investigated. The soft spark would appear when voltage reached 300 V, then change to the micro arcs at 400 V, and finally manufacture the outer MAO layer. Hereafter, the automatic extinguishing of micro arcs gives rise to the formation of inner AAO layer. Moreover, it is evidenced that plasma discharge has few contributions to coating thickening. The growth kinetics for the whole stages is a linear type, which comes from

the ion migration at the barrier layer. The barrier layer would be partially converted into MAO layer after being bombarded by discharges.

In chapter 5, the HEDP anodizing was conducted on 6063T5 aluminum alloy at different temperatures and current densities and the HEDP hard anodizing was successfully developed. Low-temperature anodizing (≤ 15°C) tends to arouse the MAO regime and coatings; high-temperature anodizing (≥ 45°C) causes the HEDP electrolyte to excessively corrode the film. The appropriate temperature for the fabrication of HEDP anodized film is ~35°C. The HEDP hard anodizing without burning was successfully conducted via a gradient-increase-current approach, resulting in a high growth rate (~ 2.1 μm/min), low porosity (< 10%), thick barrier layer (~ 510 nm) and branched nanoholes structure of the hard anodized film. The hardness of the HEDP hard-anodized film can reach up to ~11 GPa (~1000 $HV_{0.01}$), which greatly exceeds that of the widely used sulfuric acid hard-anodized film, and the corrosion resistance of the HEDP hard-anodized film is 10 times higher than that of sulfuric acid hard-anodized film.

6.2 Future work

In general, this thesis is a preliminary exploration of micro-arc oxidation and hard anodizing in HEDP solution. The newly found MAO/AAO composite structure might guide the further research on the growth mechanism of the micro-arc oxidation coating, which has not been determined so far. Moreover, functional coatings with gradient performance can be designed based on MAO/AAO composite structure, such as preparing an outer biocompatible MAO layer and filling the porous AAO layer with functional materials. For the HEDP hard anodizing, it is necessary to further optimize the anodizing conditions and clarify the influence of different alloying elements (especially copper and silicon) on it to realize the practical application.

List of Research Achievement

Ⅰ．審査付投稿論文

(1) **Hongjian Huang**, Jianhui Qiu*, Manxi Sun, Wendi Liu, Xiaowei Wei, Eiichi Sakai, Kazushi Ito, A hard coating with MAO/AAO double layers prepared on aluminum in etidronic acid by DC oxidation, *Surface & Coatings Technology*, 360 (2019) 307-317;

(2) **Hongjian Huang**, Jianhui Qiu*, Manxi Sun, Wendi Liu, Xiaowei Wei, Morphological evolution and burning behavior of oxide coating fabricated on aluminum immersed in etidronic acid at high current density, *Surface & Coatings Technology*, 374 (2019) 83-94;

(3) **Hongjian Huang**, Jianhui Qiu*, Xiaowei Wei, Eiichi Sakai, Genjie Jiang, Hong Wu,Takao Komiyama, Ultra-fast fabrication of porous alumina film with excellent wear and corrosion resistance via hard anodizing in etidronic acid, *Surface & Coatings Technology*, 393 (2020) 125767;

(4) **Hongjian Huang**, Xiaowei Wei*, Haiyan He, Yuhao Wu, Jianhui Qiu, Characterization and growth kinetics of plasma nitrided layer fabricated on Incoloy 901 superalloy, *Surface & Coatings Technology*, 396 (2020) 125960;

(5) Xiaowei Wei, **Hongjian Huang***, Manxi Sun, Wendi Liu, Jianhui Qiu, Effects of honeycomb pretreatment on MAO coating fabricated on aluminum, *Surface & Coatings Technology*, 363 (2019) 265-272;

(6) Jian Wang*, Shuai Huang, **Hongjian Huang****, Mingyang He, Peihua Wangyang, Lin Gu, Effect of micro-groove on microstructure and performance of MAO ceramic coating fabricated on the surface of aluminum alloy, *Journal of Alloys and Compounds*, 777 (2019) 94-101;

(7) Manxi Sun, **Hongjian Huang***, Xiaowei Wei, Jianhui Qiu, Aggregation of MAO coating and crack formation in the microgrooves on the aluminum surface, *International Journal of Electrochemical Science*, 15 (2020) 839-844;

(8) Shuping Jin, Jianhui Qiu*, Manxi Sun, **Hongjian Huang**, and Eiichi Sakai, Strain-sensitive performance of a tough and ink-writable polyacrylic acid ionic gel crosslinked by carboxymethyl cellulose, *Macromolecular Rapid Communications*, 2019, 40, 1900329;

(9) Jian Wang*, Shuai Huang, Mingyang He, Peihua Wangyang, Yangfan Lu, **Hongjian Huang**, Lei Xu, Microstructural characteristic, outward-inward growth behavior and formation mechanism of MAO ceramic coating on the surface of ADC12 Al alloy with micro-groove, *Ceramics International*, 44 (2018) 7656-7662.

注：博士論文テーマ関連：3 編（(1）～（3)），その他：6 編（(4）～（9)）

Ⅱ. 国際会議論文・発表

(1) **Hongjian Huang**, Jianhui Qiu, Xiaowei Wei, Eiichi Sakai, Preparation and characterization of MAO coating on aluminum with micro grooves, The 1st International Symposium on Advanced Materials Science and Engineering (AMSE-1), Akita, Japan, August 20-25, 2024.

Ⅲ. 国内会議論文・発表

(1) **Hongjian Huang**, Jianhui Qiu, Xiaowei Wei, Eiichi Sakai, Kazushi Ito, Rapid preparation of hard anodic oxidation coatings on 6063 aluminum alloy via etidronic acid, 化学系学協会東北大会,平成 30 年, 2P076.

注：博士論文テーマ関連：1 件

Acknowledgements

I would like to express my sincere gratitude to my major supervisor Prof. Jianhui Qiu for his constant encouragement and guidance. I deeply appreciate his consistent and illuminating instruction.

I would like to appreciate Prof. Qingqing Ni from Department of Mechanical Engineering & Robotics, Shinshu University, Prof. Noboru Nakayama from Department of Mechanical Systems Engineering, Faculty of Engineering, Shinshu University, and Prof. Teruo Bitoh and Prof. Nobuhiro Kanazawa from Department of Mechanical Engineering, Faculty of Systems Science and Technology, Akita Prefectural University, for being my committee members and their time in reviewing my thesis.

I deeply appreciate Prof. Xiaowei Wei from Xihua University for his kind support and comments on my thesis.

I sincere appreciate the experimental support from Assoc. Prof. Kazushi Ito, Dr. Eiichi Sakai, Dr. Tatsuya Fujii, Dr. Takao Komiyama and Mr. Hiroto Abe in Akita Prefectural University.

I wish to express my thanks to the members of Prof. Jianhui Qiu's Composites Laboratory, Dr. Jiao Chen, Dr. Longxiang Zhu, Dr. Wendi Liu, Dr. Guohong Zhang, Ms. Nie Nobe, Mr. Haodao Mo, Ms. Manxi Sun, Mr. Pengpeng Wang, Mr. Qifan Liu and Ms. Chunyin Lu for their advice and kindly help in completing my PhD program.

At last, my thanks would go to my beloved family for their loving considerations and great confidence in me all through these years.

Hongjian Huang

2021.03, Yurihonjo, Japan